

Wright State University

CORE Scholar

[Browse all Theses and Dissertations](#)

[Theses and Dissertations](#)

2011

Highly Active Porous Catalysts Fabricated by Attachment of Palladium Nanoparticles on Hierarchical Carbon Structures

Hema Vijwani
Wright State University

Follow this and additional works at: https://corescholar.libraries.wright.edu/etd_all



Part of the [Engineering Science and Materials Commons](#)

Repository Citation

Vijwani, Hema, "Highly Active Porous Catalysts Fabricated by Attachment of Palladium Nanoparticles on Hierarchical Carbon Structures" (2011). *Browse all Theses and Dissertations*. 468.
https://corescholar.libraries.wright.edu/etd_all/468

This Thesis is brought to you for free and open access by the Theses and Dissertations at CORE Scholar. It has been accepted for inclusion in Browse all Theses and Dissertations by an authorized administrator of CORE Scholar. For more information, please contact library-corescholar@wright.edu.

**HIGHLY ACTIVE POROUS CATALYSTS FABRICATED BY
ATTACHMENT OF PALLADIUM NANOPARTICLES ON
HIERARCHICAL CARBON STRUCTURES**

A thesis submitted in partial fulfillment
of the requirements for the degree of
Master of Science in Engineering

By

HEMA VIJWANI
B.E., Gandhi Institute of Technology and Management (GITAM), 2006

2011
Wright State University

WRIGHT STATE UNIVERSITY
SCHOOL OF GRADUATE STUDIES

June 24, 2011

I HEREBY RECOMMEND THAT THE THESIS PREPARED UNDER MY
SUPERVISION BY Hema Vijwani ENTITLED Highly Active Porous Catalysts
Fabricated By Attachment of Palladium Nanoparticles on Hierarchical Carbon Structures
BE ACCEPTED IN PARTIAL FULFILLMENT OF THE REQUIREMENTS FOR THE
DEGREE OF Master of Science in Engineering.

Sharmila M. Mukhopadhyay, Ph.D.,
Thesis Director

George Huang, Ph.D., PE,
Chair, Department of Mechanical and
Materials Science Engineering

Committee on
Final Examination

Sharmila M. Mukhopadhyay, Ph.D.

Abinash Agrawal, Ph.D.

Raghavan Srinivasan, Ph.D.

Andrew Hsu, Ph.D.,
Dean, School of Graduate Studies

ABSTRACT

Vijwani, Hema. M.S.Egr., Department of Mechanical and Materials Science Engineering, Wright State University, 2011, Highly Active Porous Catalysts Fabricated By Attachment of Palladium Nanoparticles on Hierarchical Carbon Structures

The effectiveness of metal-based catalysts can be significantly enhanced by increasing the available surface area relative to the volume through the creation of hierarchical nanostructures. The catalyst demonstrated here is palladium, which is a widely recognized heterogeneous catalyst suitable for a variety of industrial applications such as water purification, hydrogen storage, and electrochemical devices. In this study, a novel multi-scale supporting material developed in this group, has been used as support. It consists of micro-porous graphitic carbon with strongly attached carbon nanotubes. This can increase the surface area by orders of magnitude without increasing the size or weight while still maintaining structural integrity. This allows miniaturization of palladium catalysts structures that are lighter, smaller and more compact than conventional ones. Fabrication issues of these structures have been successfully addressed. Detailed micro-structural as well as spectroscopic analysis of the nanoparticles have been performed. Variations of palladium nanoparticles distribution with processing conditions, and the possible ways of controlling this distribution will be presented. Surface spectroscopic analysis indicates that these are zero-valent metallic palladium and do not degrade with time.

The catalytic activity of palladium nanoparticles has been tested via bench-scale experiments for reductive dechlorination of carbon tetrachloride. It is seen that palladium functionalized carbon nanotubes is highly effective in the degradation of carbon

tetrachloride and similar organic pollutants found commonly in drinking water sources. It was also demonstrated that palladium functionalized carbon nanotubes can be used repeatedly as the valence state of palladium does not change, and thus can be cost-effective.

Future scope of these results and their connection to future device applications will be discussed.

TABLE OF CONTENTS

DEDICATION	viii
ACKNOWLEDGEMENT	ix
LIST OF FIGURES	x
LIST OF TABLES	xiii
1. INTRODUCTION AND BACKGROUND.....	1
1.1. Catalysis.....	1
1.2. Palladium as Heterogeneous Catalyst	2
1.3. Metal Nanoparticles	2
1.4. Supports	4
1.4.1. Carbon Nanostructures – Family of Fullerenes	5
1.5. Carbon Supports Used in this Study	7
1.5.1. Microcellular Carbon Foam.....	7
1.5.2. Hierarchical Structures - Carbon Nanotubes Grafted on Carbon Foam.....	11
1.5.3. Flat Graphite Support – Model Study	12
2. SCOPE OF THE THESIS	14
3. LITERATURE REVIEW: Nanoparticles Synthesis Techniques	16
3.1. Lithographic Technique	17
3.2. Laser Ablation or Pulse Laser Deposition	18
3.3. Liquid-Phase Synthesis Techniques (LPS)	20
3.4. Sol-Gel Technique	23
3.5. Overview of Synthesis Techniques.....	24
4. CHARACTERIZATION TECHNIQUES	27
4.1. Field Emission Scanning Electron Microscopy	27
4.1.1. Secondary Electron Mode (SE/SB Mode)	30
4.1.2. Backscatter Electron Mode (BE/BS mode).....	30
4.1.3. Scanning-Transmission Electron Microscopy (STEM Mode).....	31
4.1.4. Energy Dispersive X-Ray Spectroscopy (EDAX)	32
4.2. Scandium© SEM Imaging Software for Statistical Analysis	32
4.3. X-Ray Photoelectron Spectroscopy (XPS)	33
5. EXPERIMENTAL	37

5.1.	Materials and Chemicals.....	37
5.2.	Microcellular Carbon Foam -Support Preparations	37
5.3.	Surface-Pretreatment Techniques for the Activation of the Foam.....	38
5.3.1.	Plasma-Enhanced Silicon Oxide (SiO _x) Surface Pretreatment	38
5.3.2.	Liquid-Phase Surface Pretreatment with Nitric Acid.....	38
5.4.	Carbon Nanotubes Grafted on Carbon Foam - Support Preparations.....	39
5.4.1.	Silica Coating by Plasma Deposition.....	39
5.4.2.	Grafting CNT by Catalytic Chemical Vapor Deposition (CCVD)	40
5.5.	Liquid-Phase Synthesis (LPS) of Supported Palladium Nano-particles	40
5.5.1.	Precursor Equilibrium-Adsorption – Stage I	42
5.5.2.	Thermal Reduction – Stage II	42
6.	RESULTS AND DISCUSSIONS: Processing and Characterization	45
6.1.	Initial Optimization of Palladium Deposition	45
6.2.	Synthesis of Supported Palladium Nanoparticles	49
6.2.1.	Pretreated Carbon Foam Supports	49
6.2.2.	Hierarchical Supports - Carbon Nanotubes-Grafted Foam Supports.....	54
6.3.	Statistical Analysis.....	60
6.3.1.	Nanoparticles Size Distribution Profiles.....	60
6.3.2.	The Number of Pd Nanoparticles Attached Per Micron Length of CNT.....	61
6.3.3.	Contact Angle Measurements of Pd-NPs on CNT.....	67
6.3.4.	The Number of Pd-Nanoparticles Per-Unit Area of the Support	67
6.3.5.	Surface Area Calculations of Pd-NPs	69
6.3.6.	XPS Analysis Done at Intermediate Steps of the Synthesis Process	71
6.3.7.	Qualitative Analysis of Pd-NPs on Bare HOPG and CNT-Grafted HOPG.....	98
7.	RESULTS AND DISCUSSIONS: Bench-Scale Dechlorination of Carbon Tetrachloride Using Palladium Catalyst.....	100
7.1.	Reductive Dechlorination Test: Objective	100
7.2.	Background.....	100
7.2.1.	Carbon Tetrachloride	101
7.2.2.	Common Contaminant Elimination Techniques.....	102
7.2.3.	Catalytic Reduction or Dehalogenation	102
7.3.	Supports Used in this Study	105
7.4.	Gas Chromatograph	108

7.5.	Materials and Methods.....	109
7.5.1.	Chemicals.....	109
7.5.2.	CT - Stock Solutions and Standards	109
7.5.3.	Batch Experiments Methods	110
7.6.	Dechlorination Results.....	111
7.7.	Catalyst Durability Investigation – SEM, EDAX, and XPS.....	120
8.	CONCLUSIONS AND FUTURE WORKS	126
	APPENDIX A – Abbreviations and Chemical Compounds	128
	APPENDIX B - Pd Loading in Different Levels of Pores.....	131
	APPENDIX C - Batch Test Analytical Data	133
	REFERENCES	136

DEDICATION

This thesis is dedicated to my Mom, Dad, Sister, and Brother and to my Family.

ACKNOWLEDGEMENT

I owe my deepest gratitude to my advisor, Dr. Mukhopadhyay, whose encouragement, supervision, and advice has enabled me to expand my knowledge explicitly. I appreciate her contribution of time and ideas, to make my Master's experience productive. She has provided me the support in various ways. Her enthusiasm and passion in science has inspired me to grow as a student and a scientist that I want to be. I am indebted to her in many ways.

I have worked with a great number of people whose contribution to the research and the making of this thesis deserve special mention. I would like to acknowledge Dr. Agrawal, who gave me generous access to their labs and gas chromatography equipments for catalyst testing. I am also grateful to him, for the encouragement he provided and the time he spent to help me achieve a clearer understanding of the subject. I also thank Dr. Srinivasan, member of my graduate committee for the valuable guidance and the suggestions. I would like to thank Dr. Jackson for his support and encouragement throughout.

Many thanks go in particular to my long time friend Kirtikant Paulla, who always provided me with the motivation and helped me in many ways. The member of Dr. Mukhopadhyay's group contributed to the my stay at Wright State, both personal and academic, Adam Maleszewski, Beth Maurer, Jared Mc Coppin, Anil Karumuri, and Ian Barney.

Lastly, I would like to thank my family for all their love, support, and encouragement. For my parents (Pahalad and Padma Vijwani) who have loved me and believed in me endlessly. For my sister (Roma Vijwani) who supported me in all my pursuits. I would also like to mention those that are no longer with us: My Grand Parents (Narumal and Leela Vijwani) and whose memory live strong with me.

LIST OF FIGURES

Figure 1 Microstructure of Carbon Foam	10
Figure 2 SEM Micrograph of CNT-Grafted on Carbon Foam	13
Figure 3 Working Principle of Scanning Electron Microscope	29
Figure 4 SEM Micrograph Showing Fe-NPs on CNT	35
Figure 5 SEM Micrograph (Left) and Scandium Analyzed SEM Micrograph (Right)	35
Figure 6 XPS Photoelectric Effect	36
Figure 7 Experimental-Setup for Synthesizing Supported Palladium Nanoparticles	41
Figure 8 Low Magnification SEM Images of Varying Adsorption Time	47
Figure 9 Low Magnification SEM Images of Varying Precursor Concentration	48
Figure 10 SEM Micrographs of SINGLE Coating of Pd-NPs on Foam.....	52
Figure 11 SEM Micrographs of DOUBLE coating of Pd-NPs on Foam.....	53
Figure 12 SEM Micrographs Showing Thermal Decomposition of CNT, Heat-Treated in the Oxidizing Environment.....	56
Figure 13 SEM Micrographs of Pd-NPs on CNT-Grafted Foam Fabricated by SINGLE Coating Process Using 62.5 mM TAPN.....	56
Figure 14 SEM Micrographs of Pd-NPs on CNT-Grafted Foam Fabricated by SINGLE Coating Process Using 25 mM TAPN.....	59
Figure 15 SEM Micrographs of Pd-NPs Fabricated on CNT-Grafted Foam by DOUBLE Coating Process Using 62.5 mM TAPN.....	59
Figure 16 Particle Size Distribution Profiles – UNTREATED CARBON FOAM	62
Figure 17 Particle Size Distribution Profiles – NITRIC-ACID TREATED CARBON FOAM....	62
Figure 18 Particle Size Distribution Profiles - SILICA COATED CARBON FOAM.....	63
Figure 19 Particle Size Distribution Profiles - CNT-GRAFTED CARBON FOAM	63
Figure 20 SEM and STEM Micrographs for Analysis of Pd- NPs Per-Unit Length of CNT.....	64

Figure 21 Contact Angle Measurements - Palladium Nanoparticles on CNT	65
Figure 22 Schematic Representation of Nanoparticles on the (A) Foam Support and (B) CNT- Grafted on Foam Support.....	66
Figure 23 Schematic Representation of the Contact Angle Made by the Particle With the Support Surface	66
Figure 24 Survey-Scan of Sample I (Pristine HOPG)	74
Figure 25 Fine-Scans of C 1s and O 1s of Sample I (Pristine HOPG)	76
Figure 26 Survey-Scans of Samples II -V (Pd/HOPG).....	78
Figure 27 Fine-Scan Spectrums of C1s for Samples I – V	79
Figure 28 Comparative Fine-Scans of Pd 3d Core Level Spectra of Sample II - V	82
Figure 29 Resolved Fine-Scan of Pd 3d Spectra of Sample II.....	83
Figure 30 Resolved Fine-Scan of Pd 3d Spectra of Sample III	84
Figure 31 Resolved Fine-Scan of Pd 3d Spectra of Sample IV	85
Figure 32 Resolved Fine-Scan of Pd 3d Spectra of Sample V	86
Figure 33 Fine-Scan Spectrums of O 1s and Pd 3p of Samples II and III	91
Figure 34 Fine-Scan Spectrums of O 1s and Pd 3p of Samples IV and V.....	92
Figure 35 Fine-Scan Spectrums of N 1s for Samples II – V.....	93
Figure 36 Fine-Scan Spectrums of N 1s for Samples II and III.....	94
Figure 37 Fine-Scan of N 1s Spectra of Control #2.....	95
Figure 38 SEM Micrographs and EDAX Scans of (A) Pd/HOPG and (B) Pd/CNT/HOPG	99
Figure 39 XPS Spectra Pd 3d Fine-Scans of (A) Pd/HOPG and (B) Pd/CNT/HOPG.....	99
Figure 40 SEM Micrographs of Supported Pd-NPs Used for CT Dechlorination Test.....	106
Figure 41 Standard Calibration Curve for (A) Carbon Tetrachloride, CT and (B) Chloroform, CF	113
Figure 42 CT Degradation Curves Obtained With Various Catalyst Supports	114

Figure 43 CT degradation Curves Obtained with Single-Size Supports, Pd/Foam and Pd/CNT/Foam.....	114
Figure 44 CT degradation Curves Obtained with Double-Size Supports, 2xPd/Foam and 2xPd/CNT/Foam.....	115
Figure 45 Carbon Tetrachloride Degradation and Chloroform Formation Curves.....	116
Figure 46 Proposed Mechanism for Catalytic Dechlorination of Carbon Tetrachloride	117
Figure 47 SEM Micrographs of Pd/CNT/Foam (A) Before and (B) After CT Dechlorination Test	122
Figure 48 EDAX Results of Pd/CNT/Foam (A) Before and (B) After CT Dechlorination Test.	123
Figure 49 XPS Pd 3 <i>d</i> Fine-Scan Spectra of Pd/CNT/Foam Before and After CT Dechlorination,	124
Figure 50 XPS (A) Cl 2 <i>p</i> Fine-Scan and (B) C 1 <i>s</i> Fine-Scan Spectra of Pd/CNT/Foam Before and After CT Dechlorination.	125

LIST OF TABLES

Table 1 Statistical Data Obtained from the Graphical Representations of the Various Samples ..	70
Table 2 Number of Palladium Nanoparticles Per Unit Length of CNT	70
Table 3 Elemental Ratios Obtained from XPS for Samples at Intermediate Steps.....	96
Table 4 Elemental Ratios from XPS and EDAX	97
Table 5 Estimated Mass of Palladium Loaded on Foam and CNT/Foam Supports	107

1. INTRODUCTION AND BACKGROUND

1.1. Catalysis

Catalysis plays a vital role in the economical, ecological, and the effective development of most of the current day technologies. It is essential for petroleum and chemical manufacture, pharmaceutical, contemporary energy conversion, and environmental technologies. Many industrial and chemical products including fertilizers, fuels, medicines, and chemicals are prepared using catalysts [1, 2]. Catalysis is a process that employs a catalyst material which converts the reactants into products in a sequential manner by participating in the process, while being regenerated to its original form upon the completion of the process. Catalyst changes the rate of chemical reactions by lowering the activation energy, but does not influence the thermodynamics of the reactions [2]. Catalysis can be categorized into two main types – homogeneous catalysis and heterogeneous catalysis. In homogeneous catalysis, the catalyst is in same phase as that of the reactants forming a single phase system (among solid-liquid-gaseous phases). Homogeneous catalysts are usually dissolved in the solvent along with the reactants (e.g. A liquid catalyst being dissolved in liquid reactants). In heterogeneous catalysis (also known as surface catalysis), the catalyst is in different phase from that of the reactants forming a system of two or more phases. A typical heterogeneous system consists of a solid catalyst with the reactants that are either in liquid or in gaseous phase.

Most transition elements and rare earth metals play an important role as solid catalysts in heterogeneous catalysis. The suggested intermediate steps of heterogeneous catalysis can be explained as follows, (i) dissociative adsorption of reactants on the surface (on the active sites) of the catalyst, (ii) chemical rearrangements such as bond

breaking or forming, at the surface forming the products, and (iii) desorption of the products from the surface of the catalyst. However, the complete mechanism is not well understood at this time. But it is apparent that the catalytic activity for such systems mainly depends on the active sites that are available on the surface of the metal catalyst for the reaction, making it a surface-dependent process [2].

1.2. Palladium as Heterogeneous Catalyst

Among various transition and rare earth metals, Palladium (Pd) is widely recognized as heterogeneous catalyst. A remarkable property of Pd is its ability to absorb hydrogen while being impervious to other gases [3]. At room temperature and moderate pressure, hydrogen can readily diffuse into the metal lattice, thereby introducing strain in the lattice. So Pd coexists in both metallic and metal-hydride phases simultaneously [4, 5]. The absorption of hydrogen into Pd is very rapid and highly reversible, which makes it a pertinent element for fuel cell catalysts, biosensors, dechlorination catalysts, etc. [6]. Pd-hydride systems are known for many hydrogen-related applications: Extraction, separation, storage, transport, and sensing of hydrogen gas [5, 7]. The hydrogenation and dehydrogenation reactions, as well as the most common coupling reactions such as Suzuki, Heck and Sonogashira reactions, are known to be Pd-catalyzed reactions [8, 9]. A majority of hydrogenation and dehydrogenation reactions studies have been examined on palladium metal as catalyst [10].

1.3. Metal Nanoparticles

Nanoparticles (NPs), also termed as nano-clusters, are particles which are in the size range of a nanometer (a unit of length which is one billionth of a meter, 10^{-9} m) to one hundred nanometers, although the term may also apply to particles in the hundreds of

nanometers-range as well. Nanoparticles, compared to their bulk counterparts, have a high percentage of the constituent atoms available at the surface. The percentage of surface atoms increases as the size of the particle decreases. The high surface area to volume ratios provided by NPs allows more accessible atoms for chemical reactions, making them ideal for effective catalytic applications. While heterogeneous catalysis, involves precious metals such as palladium, it is desirable to use nanoparticles of such metals instead of their bulk counterparts for economic reasons [11].

The additional advantages of the catalysts at nano-scale are also witnessed. Materials having at least one dimension in the nanoscale range exhibit phenomena known as “nano-effects” due to the quantum confinements that result in unique chemical, mechanical, electrical, and optical properties which may or may not reflect their own bulk properties [11, 12]. The catalytic properties (such as activity or selectivity towards a reaction path) of the metals change dramatically at nanoscale compared to their bulk counterparts and may also vary with the size of the nanoparticles [13].

Nano-catalyst systems involve nanoparticles of pure metals (mono- or multi-metals), alloys, and mixed phases either by themselves or, more commonly, attached to larger supports [14]. NPs, when present by themselves tend to agglomerate, compromising their reactivity. The metal colloidal solution is one way of stabilizing nanoparticles but they are stable only in the solutions due to the presence of solvent and the electrostatic forces [11]. Therefore stabilization of such NPs becomes important for many catalytic applications. This stabilization process is challenging and often involves the use of agents such as ligands, polymers, or surfactants known as capping agents to hinder sintering, re-crystallization, or aggregation in order to control the particle size. Synthetic macromolecular polymers or copolymers are also used in order to obtain

various shapes and crystalline structures of the particles [11, 12, 15-18]. While these external agents stabilize the particles, they also often coat or envelope the surface of the particles that may lead to either improved or reduced catalytic activity. Therefore the selection of stabilizers or capping agents is critical to catalytic activity of metal nanoparticles for specific applications.

1.4. Supports

For many different reasons, NPs are often adhered onto supports. They are generally denoted by metal/support, e.g. Pd/C is written to indicate Pd-NPs on a carbon support. Supports aid in stabilizing and handling metal nanoparticles, leading to a preference for supported metal nanoparticles over the unsupported metal nanoparticles for catalysis [19]. Supports are very important because they provide the underlying structure for the nanoparticles to stabilize and also facilitate the formation of very small particles having remarkable thermal stability. The catalyst support materials suitable for effective catalysis should possess (i) high specific surface area, (ii) thermal stability, (iii) chemical stability, (iv) high conductivity, and (v) recyclability so as to recover the metal catalyst easily [14, 19].

The common materials that have been adopted to support metal nanoparticles for catalytic applications include oxides and carbon materials such as silica, alumina, activated carbon, graphite, and nanostructures of carbon. The supports are not catalytically inert and they may influence the catalytic activity of the metal particles supported on it through specific metal-support interactions [19, 20]. A strong metal-support interaction indicates suppressed catalytic activity due to inherent changes in the electronic properties of the supported metal [20]. For example, well-dispersed

nanoparticles of various noble metals supported on titania (TiO_2) showed reduced or no activity towards chemisorptions of hydrogen (H_2) and carbon monoxide (CO). Their studies illustrate that the loss of H_2/CO sorption was due to inter-metallic interaction between the noble metals and the titania support [21].

In comparison to oxides, carbon-base materials have additional advantages as supports due to their thermal stability and chemical inertness as well as weak metal-support interactions. For example, the activity of Pt in the oxidation of carbon monoxide varies with different supports such as alumina, silica, and carbon as observed by D.J. Suh et al. Pt on carbon support had high activity which relates to the weak metal-support interactions [22].

1.4.1. Carbon Nanostructures – Family of Fullerenes

Carbon is an element which forms two types of stable covalent bonds (sp^2 and sp^3) and also has the ability to form very long chain of interconnecting carbon atoms. It is therefore capable of forming a range of hybridized structures called allotropes of carbon such as diamond (sp^3 bonding), graphite (sp^2 bonding), amorphous carbon, and a wide variety of network-like structures known as family of fullerenes. Graphite, the most widely recognized carbon allotrope used for catalytic supports, consists of sheets of hexagonal lattices of covalently (sp^2) bonded carbon atoms stacked together by weak Van der waal's forces. One individual sheet of these carbon atoms is known as 'graphene'. Fullerenes are the nanostructures, made of such sheets of carbon atoms, differing in atomic orientations and they possess very high specific surface area. The fullerene family includes, spherical fullerenes known as buckyball and cylindrical fullerenes known as carbon nanotubes (CNT). Since their discoveries, these novel nanostructures of carbon

have been studied extensively in research fields for various applications in sensors, biomedical, gas storage, electrical applications, etc. [23].

The tubular fullerenes, CNT, are known to have two major structural forms. One form, single wall carbon nanotubes (SWCNT), is a tubular form of a single layer of coaxial carbon atoms and it can be visualized as a rolled sheet of graphene. Another structural form of CNT is multi- wall carbon nanotubes (MWCNT), in which the tube consists of several concentric layers of carbon tubes. These can be simply envisioned as multiple sheets of graphene stacked and rolled together in concentric cylinders. CNT are among the strongest known materials in tension and they also exhibit extraordinary thermal and electrical properties [23]. These properties, coupled with their high specific surface area, render CNT as an attractive catalyst support. Carbon supports are also considered economically and ecologically effective as they facilitate easy recovery, refining and recycling of precious metals by a simple process of combustion. Combustion allows for maximum recovery of precious metal catalysts while producing minimal solid waste in the form of remnant ashes [24, 25].

The selection of the support in the design of heterogeneous nano-catalysts is critical as it can influence the catalytic activity of the supported metal. A considerable amount of research has been reported on the synthesis of Pd-NPs on various supports, including both flat and porous surfaces [26]. These supports provide the robustness needed in the structure for easy handling of catalyst, but may be limited by the surface area required for hosting large amounts of well-dispersed metal loading. Carbon supports such as activated carbon, free-standing carbon nanotubes, and carbon nano-fibers (CNFs) that have high surface areas have been extensively used as catalysts supports [27]. But such isolated or free standing CNT lack the ease of handling, loading, unloading, and

regenerating of supported metal catalyst from the liquid electrolyte or the reactant solutions. The demand for effective handling of free standing CNT guided researchers to the discovery of buckypaper. Buckypapers are thin films made of SWCNT, MWCNT, and/or CNF that are held intact by the weak Van der Waals forces. Buckypapers have gained attention for thermal and electrical applications. Metal NPs grown on buckypaper have been recently reported in the literature that were used as fuel cell catalysts [28].

The demands for an effective and economical catalyst support have been addressed in this study. The challenges involve exploiting multi-scale hierarchical structures of graphitic carbon that can provide the required robustness and increase the available surface area per unit volume by orders of magnitude when compared to the conventional supports.

1.5. Carbon Supports Used in this Study

A new class of carbon support, microcellular carbon foam, will prove to be an ideal support for effective catalysis because it is both robust and porous coupled with high specific surface area.

1.5.1. Microcellular Carbon Foam

Carbon foams are strong, rigid, lightweight, permeable, thermally conductive, relatively inexpensive, and have high surface area. Microcellular carbon foam, is a subset of carbon foam. It is an open cell structure which is porous and lightweight material having three dimensional arrays of interconnected seamless pores with porosities ranging from 68% to 94% [29]. It is also one of the thermodynamically stable allotropes of carbon. It is chemically identical to graphite and has well-oriented interconnected graphitic planes forming a periodic 3-D network [30]. The properties of carbon foams can

be tuned while processing and they vary according to the level of graphitization, while excessive graphitization can make the foam more brittle and hydrophobic in nature. Adequately graphitized carbon foam structures are known for higher mechanical strength, lower coefficient of thermal expansion, good thermal and electrical properties. They have potential aerospace and thermal applications. Due to its rigid structure and porosity coupled with thermal and chemical stability, they can be used as effective catalyst support materials.

The microcellular graphitic carbon foam samples were obtained as large blocks from Koppers Inc. The foam used in this study is L1a grade (company-defined grade) foam that has approximately 80% porosity and it has an estimated surface area per volume of $\sim 6.2 \times 10^3 \text{ m}^2 \text{ m}^{-3}$ [29].

While the high surface to volume ratio and the rigidity of carbon foam are advantageous for supporting metal nanoparticles, this solid is also hydrophobic in nature due to graphitization. This nature will hinder the interaction of the support with precursor solution, when it is not treated and hence calls for the implementation of surface enhancement steps for effective metal loading. Various surface pretreatment or surface modification techniques via chemical routes (plasma enhanced and liquid phase reactions) were implemented to attach surface functional groups. These treatments alter the surface chemistry of carbon foam and make it hydrophilic which facilitates infiltration of aqueous solutions. These pretreatment techniques are effective for attaching carbon nanotubes onto carbon foams or fibers [31-34].

The SEM image as shown in Figure 1 illustrates the microstructure of carbon foam showing an open cell structure and string-like ligaments. Closer examination shows that the cell walls of pores consist of micro-cracks. The cracks are created as a result of

fabrication process of foam. The carbon foam structure consists of pores in three-dimensional network. The nomenclature used in this study for simplicity is shown in Figure 1. An effort has been made here to explain the microstructure of foam having different levels of pores and ligaments.

1. *Top Ligament* – the area or the strip joining the interconnected pores that is exposed to the surface.
2. *First Pore* – a pore on the outer layer of foam. The pores are truncated and the cell walls are exposed to the outer surface. The size and depth of the various first pores may vary.
3. *Second Pore* – an interconnected pore which is one level down from the surface pore and it opens through the first pore.
4. *Third Pore* – an interconnected pore that opens through the second pore. It is two levels down from the surface as seen from the electron microscopy point of view and this pore is rarely visible.

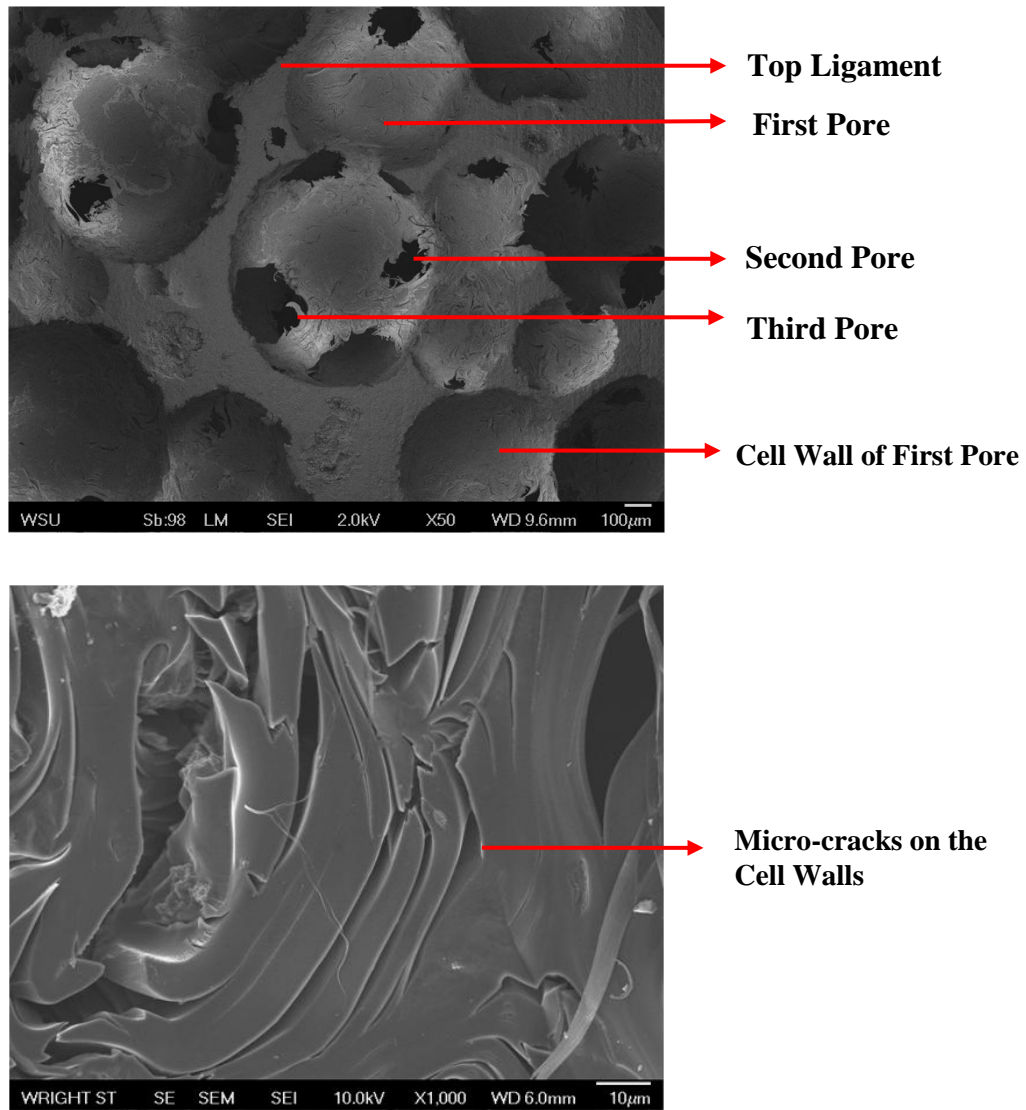


Figure 1 Microstructure of Carbon Foam

1.5.2. Hierarchical Structures - Carbon Nanotubes Grafted on Carbon Foam

Hierarchical structures are materials with multi-scale components. The important aspect of hierarchical structures is the enhancement of surface area. Many natural materials exhibit structures or components on more than one length scale in hierarchical patterns to accommodate nature's underlying challenges. Imitating nature's own trait to form microscopic hierarchical structures has received much attention for many engineering applications and it is significantly challenging. Few of the manmade microscopic hierarchical structures seen in the literature are CNT grafted on free standing fibers or weaved fibers [35]. These materials can be incorporated in composite structures that provide enhanced interfacial bonding and strength [32, 36].

A unique approach adopted by our group is grafting carbon nanotubes onto microcellular graphitic porous foam by 'Catalytic Chemical Vapor Deposition' (CCVD) technique. The hybrid structure is relatively new and is novel 3-D hierarchical structure, whose surface area is increased by several orders of magnitude without adding any weight to the support [29]. The base structure used in this study is microcellular carbon foam whose specific surface area is $\sim 6.2 \times 10^3 \text{ m}^2 \text{m}^{-3}$ [29]. The surface area per unit volume has been increased further by several orders of magnitude, by grafting CNT onto the base structures. This established composite design stands as a novel support for hosting large number of metal NPs. To the best of our knowledge such a phenomenal hierarchical rigid support, having a carbon-carbon hierarchical interface, for supporting metal particles has not been reported in literature previously. The closer composite design seen in the literature is CNT/carbon paper. It demonstrates CNT grown on carbon paper as a support for depositing metal NPs for fuel cell catalysts [37].

In this study, CNT were grown on the micro-cellular carbon foam using iron as a catalyst in CCVD process. Details of the process are given in the experimental section. Figure 2 shows the SEM micrograph of CNT grown on carbon foam. The process has been optimized and previously published by this research group [29]. Taking into account the sensitivity of CCVD process, attaching CNT onto 3-D, solid, porous, and uneven supports like carbon foam can be fairly challenging compared to that on flat supports. Previous work addresses the controlled growth of CNT on the foam surface and also within the pores.

1.5.3. Flat Graphite Support – Model Study

In parallel with microcellular foam, a model study for surface sensitive compositional analysis was carried out on a flat graphite support - highly oriented pyrolytic graphite (HOPG). HOPG has been extensively used as a conventional support for growing metal NPs [38]. The graphitic structure of HOPG can be seen in carbon foam and also in novel carbon structures, making both carbon foam and CNT chemically identical to graphite (HOPG). Its structure is significantly well understood and determined to the scientists as well as innumerable papers have been published on its surface analysis [39, 40]. HOPG is therefore selected as a support in this study for surface sensitive analysis.

HOPG was exploited as a support for growing CNT by the identical process of CCVD used for carbon foam. This hybrid design was employed for growing supported palladium nanoparticles surface analysis.

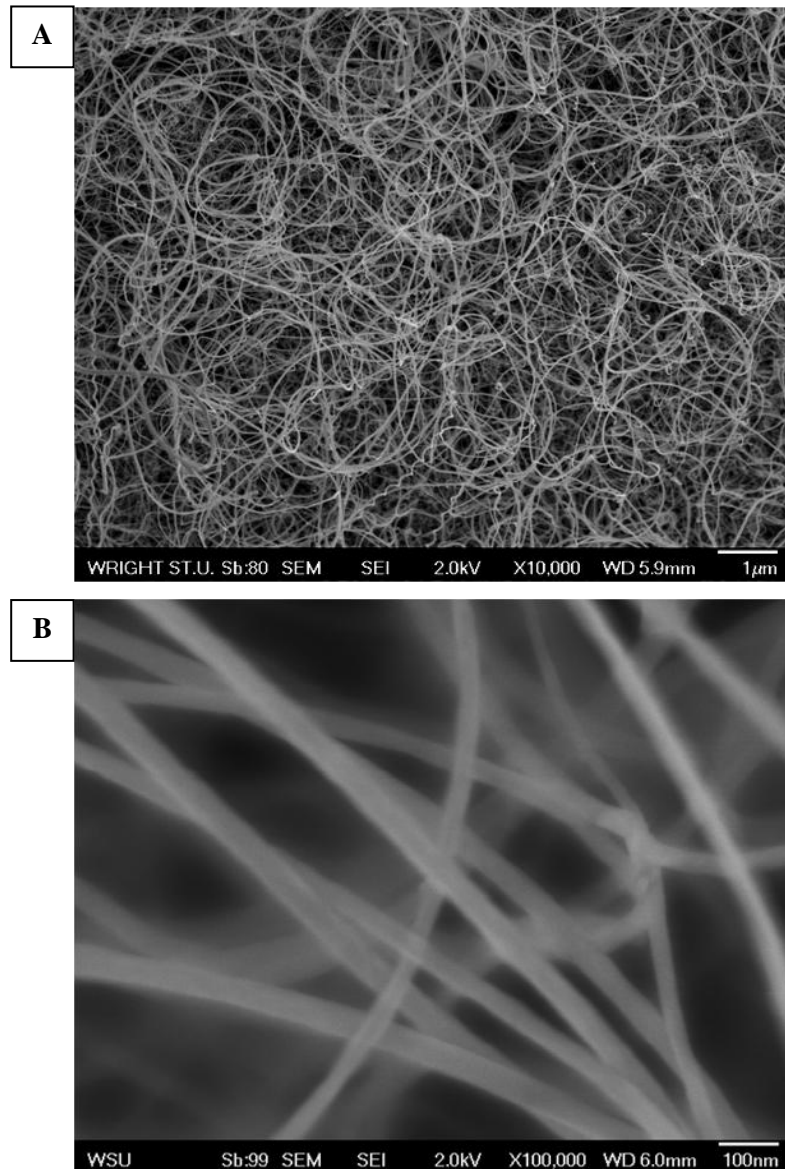


Figure 2 SEM Micrograph of CNT-Grafted on Carbon Foam

Image of First Pore at (A) 10,000x magnification and (B) 100,000x magnification

2. SCOPE OF THE THESIS

The overall idea of the thesis is to attach uniformly dispersed palladium nanoparticles (Pd-NPs) on porous carbon structures whose surface area have been enhanced by grafting carbon nanotubes (CNT) inside the pore. The goal is to have controlled amount of Pd-NPs that are highly dispersed throughout the supports including inside the pores. The focus is to investigate the influence of support pretreatment and CNT-attachment on the amount of Pd loading by suitable characterization techniques. To determine the chemical state of deposited Pd-NPs and to obtain quantitative surface analysis, flat graphite (highly oriented pyrolytic graphite- HOPG) was used as a model support.

The results of this research can be divided into two parts. The first and major part involves fabrication and characterization of Pd-NPs supported on hierarchical, porous, and robust carbon hybrid structures. The second part entails the catalytic investigation of the activity of Pd-NPs attached to these hybrid structures, meticulously for the improved activity in catalytic applications.

The characterization study of Pd-NPs is directed to the microstructural and chemical analysis using scanning electron microscopy (SEM), energy dispersive spectroscopy (EDAX), and x-ray photoelectron spectroscopy (XPS). Statistical analysis study on the microscopy images for particle size distribution and surface area analysis using commercial software is also included.

The latter part of the study was accomplished by experiments on bench-scale investigation of catalytic reductive dechlorination of aqueous phase carbon tetrachloride (CT) with the carbon-supported palladium metal nanoparticles. The study is targeted to

investigate how different carbon supported Pd-NPs influence the rate of CT transformation. In addition the durability of these catalysts have been studied by monitoring the chemical and physical state of Pd-NPs, before and after catalyst utilization, using XPS, SEM, and EDAX techniques.

3. LITERATURE REVIEW: Nanoparticles Synthesis Techniques

The synthesis of metal nanoparticles with precise control over size, shape, crystalline structure, and functionalization is critical to many nanotechnology applications in various fields including catalysis, medicine, and electronics. A synthesis technique for catalytic purposes, should aim at producing well dispersed, highly active, chemically and thermally stable, durable, and long-lasting catalyst nanoparticles, where the defined technique must be simple and be capable of reproducing the catalyst material accurately as well as should be a cost-effective technique.

Metal nanoparticles are fabricated by techniques that en-route chemical, physical and electrochemical synthesis processes. These fabrication processes are therefore classified into two main categories, ‘top-down’ and ‘bottom-up’ approaches. The top-down approach involves miniaturization of the bulk solid to smaller dimensions in order to obtain nano-structured materials. On the other hand, a bottom-up approach begins with atoms, ions and molecules as a foundation to start with and later assembles into nano-scale materials.

The top-down fabrication approaches has its roots in the conventional mechanical methods and also in the traditional material removal techniques. In the mechanically induced conventional nano-structural processing like ball milling, the bulk solid is subjected to mechanical grinding followed by stabilization using protecting agents in order to obtain stable metallic nanoparticles [41, 42]. The synthesis of metal nanoparticles by bottom-up approaches involves condensation of atoms or molecular components into larger entities usually in a gas phase or in a liquid phase. The fabrication of nanoparticles by bottom-up methods can be explained by the traditional nucleation,

growth, and agglomeration mechanisms [15, 43]. After the stable nucleation step, the particle growth greatly depends on its surface energy. If the activation energies are sufficiently low and the surface energies are significantly higher than the entropy loss, its excessive energy contributes to the enthalpy of the system. The particles then increase in size undergoing a process known as ‘Ostwald ripening’ [43, 44]. At this stage, if nucleation and growth both occur simultaneously, it results in a broad size distribution of the particles known as poly-dispersity [45]. In order to obtain mono-dispersed particles or to control the particles size, passivation of the metal surface by external agents is often carried out. There are many different ways of synthesizing metal nanoparticles, some of the important synthesizing methods with the effective measures for controlling size of particles are shown here.

3.1. Lithographic Technique

Lithography is widely used in micro and nano-electronics industry including silicon industry. A lithography technique features selective removal of the bulk material using a predetermined pattern to obtain the desired nano-pattern on the material [46]. For example, as in case of photolithography, the required geometric pattern is replicated from an image or an optical mask. The mask is formed on a radiation-sensitive polymer coated support by exposing to radiation. This is followed by a series of chemical treatments which yields the desired topography. Photolithography is however limited to resolutions below 100 nm as it relies on ultra short wavelengths of radiation [47]. On the other hand, electron beam (e-beam) lithography is a superior technique that uses an electron resist and a high energy (20 keV) electron beam. It can fabricate sub-100nm nanoparticles or nano-features. Modern lithography techniques such as SCAPEL e-beam lithography,

nano-sphere lithography have the potential to generate regular arrays of nanostructures and metal nanoparticles of 1nm in size [48-50]. These methods provide precise control over nanoparticles size, spatial parameters, and inter-particle distances which can prove effective in catalysis. Eppler et al. used electron beam lithography technique and obtained highly ordered two-dimensional arrays of platinum nanoparticles with particle diameters of 40nm having uniform inter-particle distances on silica supports [51].

Lithography techniques are often coupled with bottom-up approaches in template based fabrication of highly ordered metal nanoparticles and carbon nanotubes. Akey et al obtained 3-dimensionally controlled size and dispersion of Fe_2O_3 or CdSe nanoparticles by subsequent manipulation of silicon template using electron-beam lithography and trapping the metal solvent by micro-fluidic flow technique into the patterned wells and then thermally evaporating the solvent [52]. Selective growth of CNT was also obtained by bottom up approaches on template based synthesis by pre-depositing metal catalysts on the particular areas [53]. Lithography technique yields high precision in metal nanoparticles dispersion, but this technique involves high equipment cost and are however limited to only few types of supports.

3.2. Laser Ablation or Pulse Laser Deposition

Laser ablation, sometimes also known as pulse laser deposition, is a thin film deposition technique which has been used as a powerful tool to fabricate nanoparticles in different environments such as high vacuum, inert atmosphere, and liquid environment [51, 54, 55]. A pulsed or continuous laser beam in the controlled environment is focused on a bulk material that is to be ablated. In high vacuum ablation, the bulk material is vaporized that forms a plasma plume, while a target (support) on which NPs are to be

deposited is placed in the direction of this plume. The support can be rotated to avoid the pit formation in order to deposit a uniform layer of nanoparticles. The size of the nanoparticles can be controlled by varying the pulse duration, number of pulses, and the intensity of the laser beam [55]. Nanoparticles are deposited on a support in high vacuums which typically range from 10^{-5} to 10^{-7} Torr. Alternatively, an inert atmosphere can be used by flowing gases like argon or helium into the ablation chamber to obtain metallic nanoparticles. Reactive gases such as oxygen can be used to deposit metal-oxide nanoparticles. Colloidal solutions of nanoparticles are prepared in water (hydrosols) or organic solvents (organosols) [55, 56]. In these colloidal ablations, the bulk solid is irradiated in a solution where the material undergoes sublimation and forms nanoparticles. By using this method, Pd nanoparticles were synthesized via pulsed laser ablation of palladium in acetone. In this process, a nanosecond pulse of an Nd:YAG laser was employed resulting in a Pd colloidal solution with a mean particle size of 7 nm. Supported Pd nanoparticles were further obtained by depositing drops of colloidal solution on the silicon support and allowing it to dry at room temperature [57].

One of the most viable routes for laser ablation in vacuum is carried out by consistent use of ultra short laser pulses in the ranges of femto-seconds (fs) and nanoseconds (ns) to obtain highly controlled particle sizes. By varying the number of pulses, silver nanoparticles of mean diameters in the range of 5 nm to 60 nm have been deposited on a glass support using a Nd:YAG laser in vacuum [58]. Although laser ablation has high operation and equipment cost, it can be used as a cost effective high throughput technique by using advanced setups. It has a rotating target holder on which multiple targets materials can be mounted and well-ordered multi-metallic nanoparticles can also be synthesized in vacuum via this versatile technique [59].

3.3. Liquid-Phase Synthesis Techniques (LPS)

The liquid-phase synthesis techniques have been extensively used for synthesis of supported metal nanoparticles and the approach is quite-versatile for emplacing metals or metal compound particles onto uneven supports. It involves exposing the support to an aqueous solution containing soluble metal salt (a precursor solution containing the active component). The support can be coated with the precursor solution either by the proper wetting conditions, i.e. no excess solution being left behind known as ‘dry adsorption’, or by immersing the support in the excess amount of precursor solution known as ‘equilibrium adsorption’. The prominent key variables of the LPS method are the concentration of the metal precursor solution and its interaction with the support. The support in contact with the solution or coated with the metal complex ions is reduced into metal or metal oxides by additional chemical and/or thermal reduction processing.

Chemical Reduction

The chemical reduction is carried out in the presence of a chemically derived compound known as reducing agent. It is done by introducing an external chemical agent into the support containing precursor solution. This involves in increasing the pH or in some cases decreasing the pH, changing the valence state of the precursor, or changing the concentration of the metal ion complexes followed by reduction resulting in metallic particles [60 - 63]. Jin et al. have investigated the deposition of Pd on activated carbon fibers by alkaline hydrolysis of palladium chloride (PdCl_2). This results in the deposition of $\text{Pd}(\text{OH})_2$ on the carbon surface that is followed by a liquid-phase reduction using formaldehyde as a reducing agent [64].

In the chemical reduction process, using reducing agent alone may result in poly-dispersed nanoparticles and it requires additional measures to constrain the particle distribution. To control the size of the nanoparticles and to inhibit agglomeration, other compounds like capping agents, stabilizers, or surfactants are used. It is often done by the process in which the metal salt solution is reduced under heating and continuous stirring in the presence of a reducing and a capping agent [65]. A citrate capping electroless process first introduced by Turkevich et al. in 1951 is the most cited method. Here the citrate was used as both a reducing and a capping agent to make colloidal Au-NPs in which particles of 20 nm in diameter were obtained [15]. Innumerable studies have been carried out thereafter to develop the process in order to control the size of the particles and also to attach them onto the supports. Qin et al. obtained Pd-NPs of about 3.8 nm in diameter on CNF by citrate reduction of PdCl_2 using NaBH_4 and tri-sodium citrate [66]. The chemical reduction technique can also be modified to synthesize various shapes and well-controlled sizes of metal NPs for many different applications by using stabilizers or surfactants like thiols, dendrimers, ligands (sulfur based), and micro-emulsions (water in oil or oil in water) [16, 17, 67-69]. Lee et al. obtained well-defined morphologies such as cubic, multi-arm, and dendritic shaped Pd nanoparticles by varying the injection sequence of the reductant and surfactant under other similar experimental conditions [70]. Polymer stabilized NPs have also been reported in the literature using some common polymers such as poly(vinyl propylene), poly(vinyl alcohol), and also block copolymers. Piao et al. obtained uniform Pd-NPs of various shapes and sizes stabilized by a tri-block copolymer and adjusting the pH of the solution [71].

Thermal Reduction

In the thermal reduction, the solid support recovered from the precursor solution is followed by subsequent steps of drying, calcining, or reducing. The coated support is dried to eliminate the hydrating solvents and then heated at elevated temperatures to decompose the metal precursor compounds. This latter step is also known as ‘calcination’ or ‘pyrolysis’. It can be carried out in both oxidizing or inert environment specific to metals and their applications. The primary advantage of this step is to remove the undesirable groups like organics, nitrates, halides, and sulfides that were introduced from the precursor solution [72]. The removal of precursor groups leads to the formation of metal or metal oxides. In the reduction step, the metal oxides are made to react with a reducing gas at elevated temperatures in inert atmosphere or vacuum to form zero-valent metals [73]. The metal oxides or metals formed by the thermal reduction methods may undergo ripening process, where the growth and nucleation of nanoparticles happens simultaneously. This results in a broader size distribution of metal nanoparticles. The strategy of obtaining well defined particles distribution lies in the thorough understanding of the process.

Gurrath et al. prepared palladium catalyst supported on activated carbon by coating with various precursor solutions followed by thermal reduction. Carbon was coated with the aqueous H_2PdCl_4 , $\text{Pd}(\text{OAc})_2$ in acetone, or cationic Pd nitrate complex followed by drying in an oven at 380K that was reduced in pure hydrogen atmosphere to obtain metallic Pd [74].

Owing to its versatile nature, LPS methods for synthesizing metal nanoparticles are among the most frequently cited and widely used methods for the synthesis of supported metal oxide or metallic nanoparticles.

3.4. Sol-Gel Technique

A sol is a colloidal suspension of solid particles in a liquid and a gel is commonly referred to as a continuous solid and liquid phase of the colloidal suspension. The sol-gel is a process in which a gel is formed by the aggregation of particles of the precursor sol in such a way as to form a network known as 'liogel' or 'hydrogel' [75]. The common precursors are organosilicates (e.g. TEOS - tetraethoxysilane) that results in the silicate sol-gel materials. The porosity of final gels can be tailored by various modes of drying. Drying of the wet gels by ambient evaporation results in 'xerogel', whereas 'aerogel' are formed by supercritical drying. Another way of drying is by freeze-drying that forms 'cryogels' [76]. These solid gels have high degree of homogeneity and differ in physical morphologies such as porosity and surface area and they resemble the structure of foam.

Besides tailoring the porosity, the foams prepared from sol-gel process can be doped with external agents such as metal nanoparticles for use as potential catalysts. As the sol-gel process initiates with a sol suspension it is possible to basically add any compound as a guest molecule or a dopant, such as metal precursor compound or metal nanoparticles. The gels doped with metal precursor compounds are followed by subsequent traditional treatments to reduce the metal ions into metal nanoparticles. Patricia et al. have successfully prepared palladium composites from tetraethoxysilane (TEOS) and PdCl_2 , by dissolving suitable amounts in ethyl alcohol and water followed by continuous stirring to form wet gels. Pd nanoparticles loaded silicate xerogels were formed by ambient evaporation and appropriate reduction of the metal [77]. However, sol-gel process is not restricted only to silicon compounds, carbon based aerogels can also be prepared similarly while doping with metal compound or metal nanoparticles [78, 79]. S. Cacchi et al. prepared Pd-carbon aerogel catalysts by doping Pd-NPs in the initial

sols and used the resulting material as a catalyst. They demonstrated that such supported catalyst are active and can be effectively retained as well as used multiple times [79].

The combinations of sol-gels with transition metal particles or CNT-grafted metal particles have lead catalysis to a promising future [77-80]. Pt/CNT and Pt/CNT/TiO₂ were fabricated by Chen et al. by proper mixing of respective compounds or salts in the solvent solution of benzene and HCl followed by heat treatment undergoes solidification and results in the aerogels [80]. Photo-catalytic analysis revealed that Pt/CNT/TiO₂ composite had higher catalytic activity.

The gelation produces polymeric chains with physically entrapped colloids or nanoparticles, where the significant amount of expensive metal or CNT incorporated in gels may be masked by the solid material which will not participate in catalysis [81]. A characteristic of sol-gel technology is the fact that samples can be obtained as porous bulks, thin films, or powders. Therefore, these supports can be used as templates for various other material synthesis processes [82]. For example, silica templates formed by sol-gel method were used as supports for attaching metal nanoparticles. In other cases, the metal doped porous support such as silica or alumina films doped with FeO particles, prepared by sol-gel technique were used as templates for synthesis of CNT [83].

3.5. Overview of Synthesis Techniques

Supported metal nanoparticles can be synthesized by one method or by combinations of the aforementioned methods (not limited to mentioned methods). An overview is given here based on the literature review.

- Lithography and laser ablation techniques produce highly ordered, well-defined, and contaminant-free metal nanoparticles. The main disadvantage of these techniques is the cost and the maintenance of such systems.
- Liquid phase synthesis (LPS) techniques are cost effective techniques, but its major problem lies in the inefficiency of producing both uniform size nanoparticles and contaminant-free metal surfaces [74, 85-86]. The additional chemical measures adopted for controlling the size of nanoparticles will inevitably coat the surface of the particle yielding an contaminated metal surface.
- Highly ordered supports via lithography technique and highly porous structures via sol-gel methods can be prepared. These structures can be used as base support for synthesizing highly ordered metal NPs and/or to selectively grow CNT by bottom-up approaches.
- Metal colloids can be synthesized by laser ablation or liquid phase synthesis methods. Colloidal solutions of metal or metal-functionalized CNT are often dispersed in the sols to make supported metal NPs via sol-gel techniques. Such composite structures closely resemble to the hierarchical structures used in this study.
- CNT grown on such highly oriented or porous supports can serve as a hierarchical structure for hosting metal nanoparticles. This composite is similar to the supports used in this study. To the best of our knowledge such hybrid materials for supporting metal NPs has not been reported in the literature.
- A more widespread synthesis route for obtaining supported metal nanoparticles is via evaporation of the colloidal solution onto the above discussed supports.

- In this study, a LPS technique by the equilibrium adsorption of precursor, combined with thermal reduction technique, has been implemented to fabricate Pd-NPs on porous carbon foam supports as well as on CNT-grafted carbon foam supports.
 - Tetraamine palladium (II) nitrate (TAPN) solution was used as a metal precursor solution followed by thermal reduction method using H₂ gas as a reducing agent. TAPN was chosen as the precursor in this study, as the amine and the nitrate groups of the precursor at the elevated temperatures will decompose into respective gases, leaving a highly desirable contaminant-free surface. Such is not the case for halide or sulfate precursors that are reduced thermally [85].
 - TAPN has been used previously to synthesize Pd-NPs onto the porous supports and activated carbon [74, 85-86]. To the best of our knowledge, TAPN has not been employed as a precursor on CNT or hierarchical CNT supports previously. Also, synthesizing Pd-NPs via thermal reduction technique on the CNT-grafted porous supports has not been reported in the literature and it is unique to this project.

4. CHARACTERIZATION TECHNIQUES

Once the supported nanoparticles are synthesized, effective characterization techniques were used in order to study its surface morphology and surface composition. It is essential to recognize the synthesizing conditions and the resulting materials to reproduce effectively. Surface morphology of metallic nanoparticles and hierarchical architectures were observed using JEOL 7401F Field Emission Scanning Electron Microscope (FE-SEM). The FE-SEM is coupled with Energy Dispersive Spectroscopy (EDAX) that provides elemental data analysis. It is one of the most popular tools for nanotechnology. X-ray Photoelectron Spectroscopy (XPS) was performed using Kratos (Axis Ultra) system for element compositional analysis. Quantitative analysis was carried out on SEM images using Scandium© SEM imaging software provided by JEOL 7401F for FESEM. The mechanism of the aforementioned characterization techniques and their contributions in this study are briefly discussed in this chapter.

4.1. Field Emission Scanning Electron Microscopy

The discovery of SEM has revolutionized most of the current technologies. Field emission scanning electron microscopy (FESEM) is one of the most important characterization technique used in this study to meet the challenges of materials microstructural characterization. The schematic representation of the mechanism of SEM is shown in Figure 3. It uses a high energy beam of electrons produced by an electron gun that scans the surface of the sample in a raster form, under a high vacuum. The electrons from the electron gun follow a path through the electromagnetic lenses that focuses the beam onto the sample. As the beam reaches the sample, electrons (secondary, backscatter, transmission, and auger electrons) and x-rays are ejected from the sample

(Fig. 3). The electrons or x-rays are collected by the various detectors placed as shown in Figure 3. The detectors convert these electrons into the signals that contain information about the sample's surface topography and composition. The number of electrons emitted from the sample surface that are detected, are transformed into a variable gray scale and arranged to produce an image, the pixels of which correspond to the positions of the beam on the sample surface. Therefore, it is possible to provide information on the surface topography in the form of an image with varying contrast and brightness [87]. Conventional SEM has resolution of about magnification few nanometers, but FESEM takes the characterization limits a step ahead by providing a very high resolution (~1 nm) allowing useful imaging up to 1,000,000x magnification. Unlike traditional SEM, FESEM produces high quality images as it uses a cold cathode field emission gun with narrow electron beam and high depth of field in an ultra high vacuum, providing the feasibility of imaging at both low and high accelerating voltages. FESEM has various operational modes that can be used for different imaging applications. The different modes of operation that have been used in this study are discussed below.

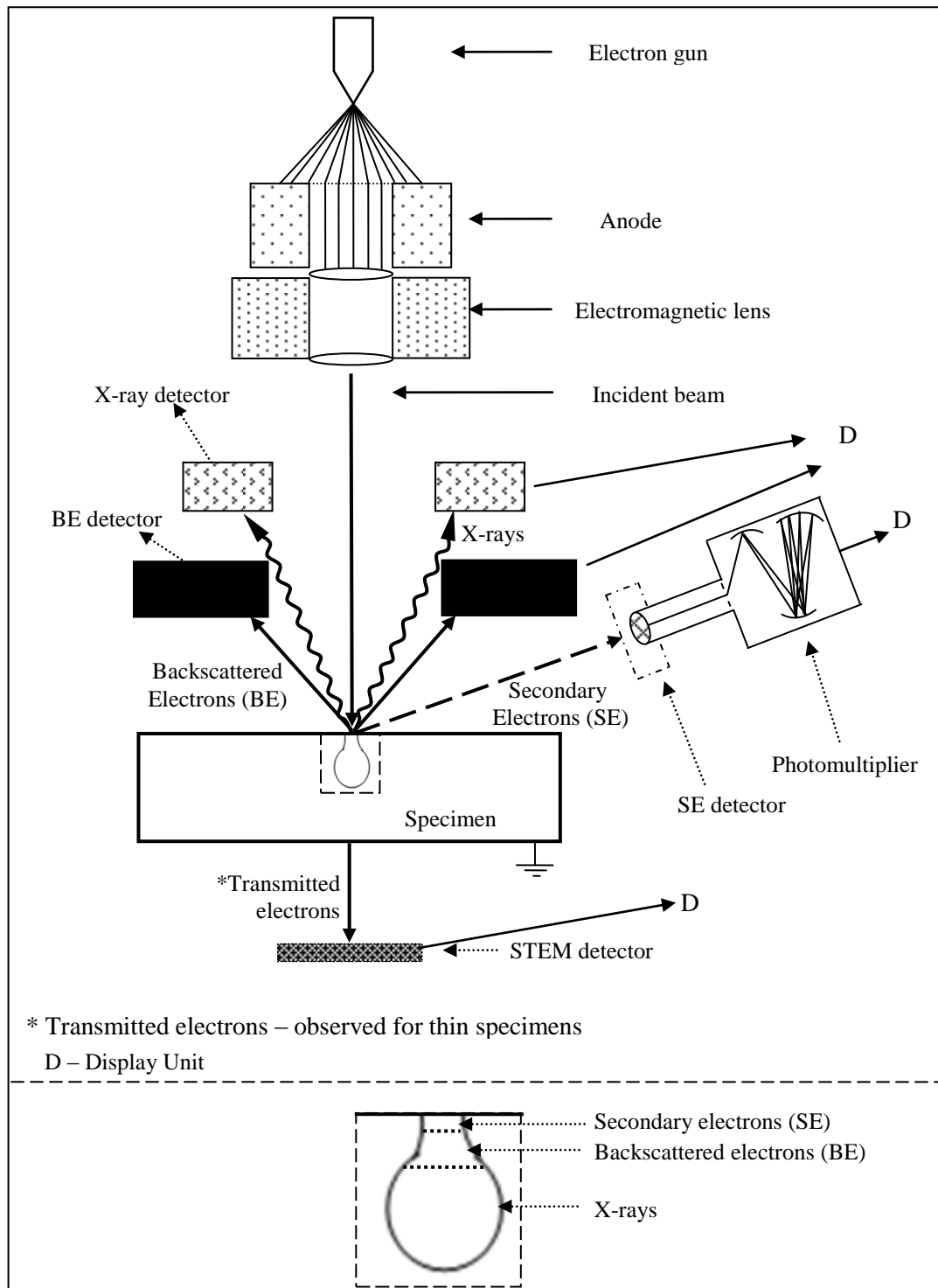


Figure 3 Working Principle of Scanning Electron Microscope

Reference [87]

4.1.1. Secondary Electron Mode (SE/SB Mode)

Secondary electron mode is the standard detection mode that collects the secondary electrons emitted from the sample as shown in Figure 3. Secondary electron imaging provides very high resolution images of up to few nanometers. Secondary electrons are emitted within few nanometers from the surface which provide quality information with high resolution images (Fig. 3). These electrons once emitted from the sample are attracted by an electrically-biased grid towards the secondary electron detector. The detector is a scintillator-photomultiplier type of detector that converts the detected electrons into light pulses (scintillation) and then via an electron multiplier into an amplified signal. It is finally converted to a digital image and appears on the display unit. The SEM analysis on Pd-NPs samples utilized secondary images and mixtures of secondary and backscattered images.

4.1.2. Backscatter Electron Mode (BE/BS mode)

Backscattered electron mode is used in order to identify areas in the sample with different elements or chemical phases. In the BE/BS mode, the image is represented as a function of atomic number (Z), in a fashion such that heavy elements are represented by bright areas of the image. The BE/BS mode employs back-scattered electrons, the electrons that are reflected back due to scattering interactions with the sample. These electrons are emitted from a depth in the sample and the resolution of BE/BS mode images is lower than secondary mode. The back-scattered detector is in a doughnut form and it is positioned right above (90°) the sample unit in the UHV chamber of SEM. The detector can be of scintillation type or semi-conducting type. The variation in contrast and brightness of the image is a result of number of electrons reaching the detector. As

heavy elements backscatter more electrons than light elements, they appear brighter in the image. In this study, the BE/BS mode was employed to spot the iron nanoparticles (Fe-NPs) coverage on as-prepared CNT-grafted samples, a condition highly sensitive to CCVD process parameters. A sample consisting of excessive Fe-NPs covered on the CNT as shown in Figure 4 is not acceptable for growing Pd-NPs.

4.1.3. Scanning-Transmission Electron Microscopy (STEM Mode)

As the name suggests, STEM has typical characteristics of both Scanning electron microscopy (SEM) and Transmission electron microscopy (TEM). In STEM mode, a high energy and extremely narrow beam of electrons interacts with the sample in a raster pattern and the transmitted electrons are captured by the detector which is mounted beneath the sample holder unit. The detector used for STEM imaging is an annular dark field detector (ADF), a disc like detector with a bright field detector (BF) at the center. Depending on the number of electrons being transmitted through the sample, the gray scale the image varies. Large atomic number elements transmit fewer electrons through it and *vice versa* interpreted as dark and light areas respectively. Therefore, it is useful for investigating outer and inner microstructural details such as core of the hollow nanomaterials, nano sized defects, embedded nanoparticles and varying nano-elemental compositions. But it is limited to small sample size ('less than' $< 10\ \mu\text{m}$). To detect the transmitted electrons of the sample, a special kind of holder is used which consists of thin mesh-like films for holding samples. In this study, STEM was used to identify and characterize the Pd-NPs coverage on the CNT support and to determine the contact angle of the nanoparticles on CNT. The Pd attached CNT were gently scratched from the

surface of foam using a razor blade and transferred onto the copper grid provided for STEM analysis.

4.1.4. Energy Dispersive X-Ray Spectroscopy (EDAX)

Energy dispersive x-ray spectroscopy in SEM is capable of providing qualitative elemental analysis of the sample surface up to a surface depth of several μm . It not only identifies the elements present in a sample but also quantifies their chemical ratio. The beam of electrons interacts with the atoms and causes transition of electron in the orbital shells which results in the emission of x-rays from the sample. The x-rays from sample are collected by the x-rays detector which converts them into signals. The intensity of the characteristic x-rays allows the elemental composition of the sample to be measured. In this study, EDAX Genesis© software was used to obtain qualitative elemental analysis of the Pd fabricated samples.

4.2. Scandium© SEM Imaging Software for Statistical Analysis

The Scandium© software provided by JEOL FESEM enables statistical image analysis of the SEM micrographs. It effectively allows us to analyze the images by laboriously portraying various shapes such as a point, length, area, or angle using respective tools. A typical example of the SEM micrograph analyzed for particle size distribution using the Scandium© length tool is shown in Figure 5. The marked data is obtained in the excel sheet format.

Quantitative image analysis was carried out to determine the size distribution profiles of Pd-NPs on carbon supports, number of particles per unit length of CNT, and the contact angle measurements of the Pd-NPs with CNT. Using the appropriate tool,

manual marking was done carefully to minimize operator errors. An automated excel sheet was therefore generated and the data was analyzed.

4.3. X-Ray Photoelectron Spectroscopy (XPS)

XPS technique also known as electron spectroscopy for chemical analysis (ESCA) is the most widely used surface analysis technique. It determines the quantitative atomic percentages, chemical bonding, and the electronic state of the elements present in the first few layers of the surface of the material. The working principle of XPS is based on photoelectric effect (Fig. 6). XPS uses an ultra high vacuum (UHV $\sim 10^{-9}$ Torr) where the sample surface is irradiated with a source of photons, usually Mg K α (1253.6 eV) or Al K α (1486.6 eV), yielding electrons emitted from the sample surface. The X-rays penetrate the sample to a surface depth of 1 μm but the useful electrons that contribute to the analysis are emitted from the surface depth of about few angstroms (10 Å to 100 Å). Due to these short range photoemissions, XPS is considered a surface specific chemical characterization. The electrons that are emitted from a depth usually collide with the other atoms on their exiting path, losing the energy and hence contribute to noise. The electrons are emitted with certain kinetic energies that can be detected and analyzed by an electron energy analyzer. The efficiency of the electron energy analyzer depends on various parameters such as pass energy and the analysis spot. The core shell electrons from the atoms encompass the prominent characteristics of the particular element.

As we know the energy of the x-ray photon from Einstein's relation,

$$E_{\text{photon}} = h\nu$$

The binding energy of the electrons is thus determined by the following equation,

$$E_B = E_{\text{photon}} - E_K \quad (\text{or})$$

$$BE = h\nu - KE$$

Where, E_B is the binding energy (BE) of the electron, E_{photon} is the total energy of the x-ray photons and E_K is the kinetic energy (KE) of the electron.

The data obtained are the graphs of binding energies with respect to the intensities of the electrons. The graphs will have peaks at certain binding energy values known as peak positions that are representative of the elements. The assignment of the elements or compounds to the obtained peak positions is done with the help of standards. Quantitative analysis is obtained using the published data in the literature on binding energies, for the peak positions, peak shapes, full width at half maximum (FWHM), and relative intensities, as the reference. All elements except hydrogen and helium can be detected by XPS. Single peak is observed for 's' orbital whereas two peaks are observed for 'p', 'd', and 'f' orbital having peak area ratios of 1:2, 2:3, and 3:4 respectively indicating different spin orbitals. The spin orbital splitting is the distance between the two peaks which can also be helpful in identifying the elemental compounds present. A correction of energies may be required on all the species that shift due to charging effects [88, 89].

In this study, XPS was performed using Kratos (Axis Ultra) system with monochromatized Al $K\alpha$ x-rays. The chemical states and compositional analysis of the fabricated palladium nanoparticles supported on carbon samples were obtained. The quantitative chemical processing and characterization was obtained using 'CasaXPS®' software for XPS.

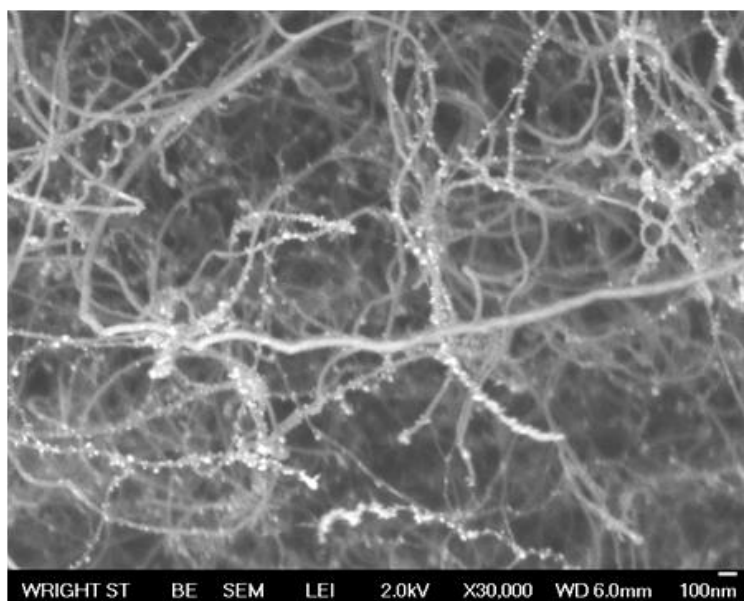


Figure 4 SEM Micrograph Showing Fe-NPs on CNT
Taken in Backscattered (BE/BS) Mode

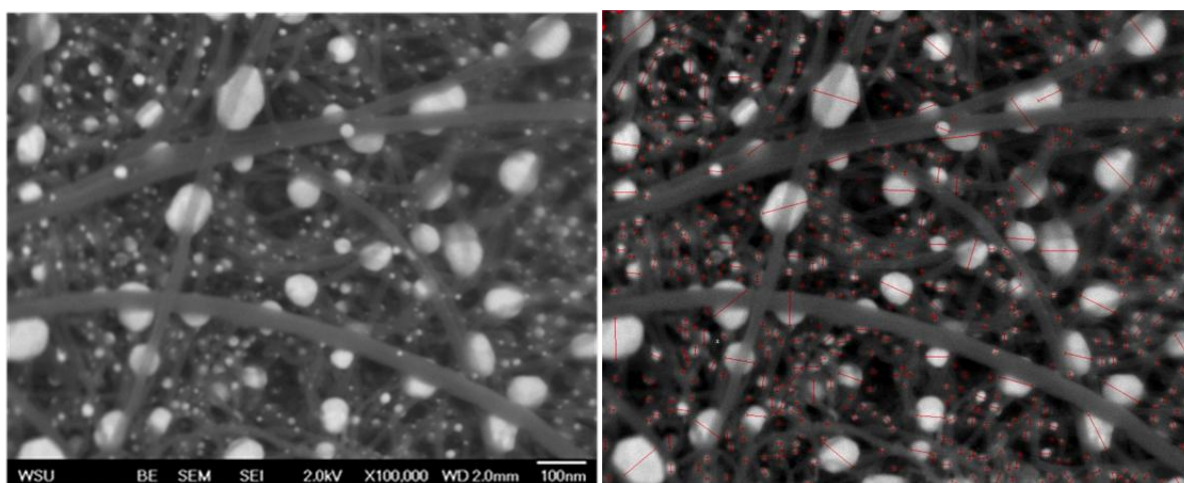


Figure 5 SEM Micrograph (Left) and Scandium Analyzed SEM Micrograph (Right)
Pd-NPs fabricated on CNT-grafted on foam (Left), particle size annotations obtained using
Scandium software (Right)

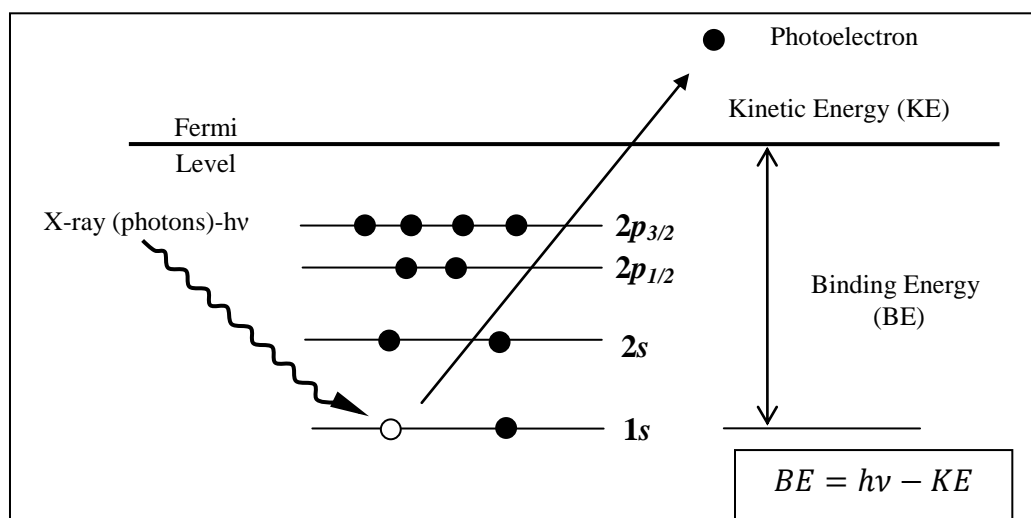


Figure 6 XPS Photoelectric Effect

Reference [88-89]

5. EXPERIMENTAL

This chapter provides an insight to the procedures adopted and established for the current research. It explains the process for fabricating Pd-NPs on hierarchical and uneven supports in details.

5.1. Materials and Chemicals

The L1a grade microcellular graphitic carbon foam used in this study was acquired in the form of blocks provided by Koppers© Inc (Pittsburg, PA). The sheets of highly oriented pyrolytic graphite (HOPG) were obtained from Molecular Imaging Ltd. All the reagents were of analytical grade and used without further purification including Hexamethyl-di-siloxane (HMDSO, Sigma-Aldrich chemicals), Xylene (PTI Process Chemicals), Ferrocene (99%, Alfa-Aesar Ltd), Tetraamine Palladium (II) Nitrate solution (0.375M, 99.9% TAPN, 5% Pd, Alfa- Aesar Ltd), methanol and concentrated nitric acid (HNO_3 , 70%). The water used in this study was distilled water.

5.2. Microcellular Carbon Foam -Support Preparations

The microcellular carbon foam of thickness 2 mm was used as a support for growing both CNT and Pd-NPs. The blocks were cut into desired size and shape using a band saw machine. These samples were further polished to maintain a uniform thickness and smoothness of $2 \text{ mm} \pm 0.1 \text{ mm}$, using various grades of sand paper. After subsequent sanding, the extra or loose carbon that was left behind in the pores was removed by blowing compressed air through the foam. The lateral dimensions of foam were specific to the study.

5.3. Surface-Pretreatment Techniques for the Activation of the Foam

The following surface activation techniques have been employed which were carried out prior to the palladium coating treatment. Hence these surface activation techniques are referred as surface pretreatment techniques.

5.3.1. Plasma-Enhanced Silicon Oxide (SiO_x) Surface Pretreatment

A silicon oxide (Silica, SiO_x) coating was done on the as-prepared carbon foam support. The oxide coating of silicon was carried out using a plasma assisted microwave reactor (V15GL manufactured by PlasmaTech Inc.). The support placed in the microwave chamber was exposed to different amount of oxygen and hexa-methyl di-siloxane (HMDSO) in successive steps of cleaning, coating (5 minutes), and stabilizing [33, 34, 89]. Longer times of coating step resulted in thicker coatings of silica. A silica coating step of 10 minutes was performed that results in a nano-layer of silica throughout the foam, successfully making it hydrophilic.

5.3.2. Liquid-Phase Surface Pretreatment with Nitric Acid

The liquid-phase surface activation process was done by immersing the foam support in an aqueous solution of 16M nitric-acid (HNO_3) for 10 minutes [34, 89]. The foam support was then removed and rinsed thoroughly with distilled water followed by ultra-sonication in the same for 15 minutes. The supports were stored in water (no longer than 15 – 30 minutes) until used for fabrication of Pd-NPs.

5.4. Carbon Nanotubes Grafted on Carbon Foam - Support Preparations

Carbon nanotubes (CNT) were grafted on the carbon supports by catalytic chemical vapor deposition (CCVD) process which has been optimized previously by this group [29, 32, 89]. In this study, CNT were essentially grown on microcellular carbon foam and HOPG, by a slightly modified CCVD process. The process includes pre-coating of the support with silica in a plasma reactor followed by carbon nanotubes coating in a two stage furnace by CCVD process.

Growing carbon nanotubes on the micro cellular carbon foam is challenging due to the complex support geometry. Our goal is to obtain uniform CNT throughout the pores of the foam. An obvious attempt was to have a smaller thickness of the support. The thickness of carbon foam support for growing CNT was uniformly maintained at 2.0 ± 0.1 mm by subsequent sanding followed by cleaning. The lateral dimensions of the carbon foam were roughly selected to be $6 \times 4 \text{ cm}^2$. After coating with silica the foam supports were cut to the shape of an ellipse of 5 cm major diameter and 3 cm minor diameter with a small V-notch on one end of the major diameter [29].

The thickness of the obtained sheets of HOPG was 3.1 mm. The sheets were cut into blocks of lateral dimensions $5 \times 1 \text{ cm}^2$ and used as supports for growing CNT.

5.4.1. Silica Coating by Plasma Deposition

In the first step of coating CNT, the carbon foam supports were pre-coated with silica by a gas-phase plasma technique. The supports were placed on a wire mesh in the microwave chamber for coating. Silica coating process as discussed in the previous section was performed (Section 5.3.1.). Silica coating time of 15 minutes was done, by repeating the successive steps of coating (5 minutes) and stabilizing in a cyclic manner

after an initial cleaning step. In order to obtain a uniform coating of silica throughout the pores of the foam, a similar 15 minutes silica coating was followed on the other side (bottom side) of the foam by flipping the support.

5.4.2. Grafting CNT by Catalytic Chemical Vapor Deposition (CCVD)

Carbon nanotubes were fabricated in a two-stage furnace on the silica coated carbon supports using CCVD process. The typical two stage furnace consists of a preheat furnace and a main furnace. A mullite tube (length 750 mm, inner diameter 30 mm) closed with stainless steel ends cap is placed in the furnace. The supports were placed in the center of the main furnace making an inclination with the tube. A solution of ferrocene (0.1 g) dissolved in xylene (10 mL) was used as a floating catalyst and a prominent source of carbon. The solution was injected at a temperature of 220 °C maintained by a preheat furnace. The reactions were allowed to take place at 750 °C for a specific length of time in an Ar/H₂ environment to facilitate the growth of CNT. A reaction time of 20 minutes was carried out to grow CNT on the carbon supports used in this study. The furnace was allowed to cool down to room temperature in a reduced flow of Ar.

5.5. Liquid-Phase Synthesis (LPS) of Supported Palladium Nano-particles

Palladium nanoparticles on the carbon supports were synthesized by a two stage process that includes precursor equilibrium adsorption followed by a thermal reduction [74, 84-86]. The dimensions of the supports used in this study were 10x5x2 mm³.

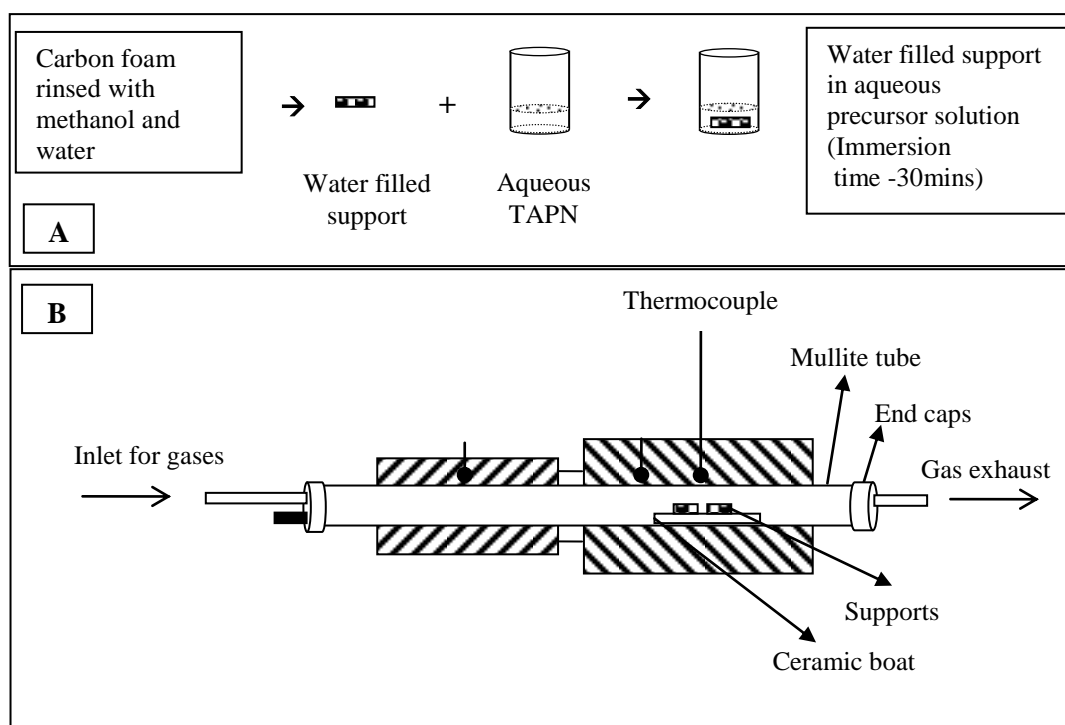


Figure 7 Experimental-Setup for Synthesizing Supported Palladium Nanoparticles

(A) Precursor Adsorption and (B) Thermal Reduction

5.5.1. Precursor Equilibrium-Adsorption – Stage I

The supports were pre-cleaned with methanol and water prior to immersing in the metal-precursor solution. These water filled carbon supports were now immersed in an aqueous precursor solution of tetraamine palladium (II) nitrate (TAPN) for certain period of time. The molar concentration used in this study was 62.5 mM TAPN and the supports were immersed in the solution for 30 minutes, unless specified otherwise. The solid supports were recovered from the TAPN solution and the excess non-interacting solution on the sample was washed-off by briefly dipping the support in methanol. The samples were placed on a ceramic boat and were immediately transferred to the furnace for thermal reduction processing.

5.5.2. Thermal Reduction – Stage II

The thermal reduction was carried out in a mullite tube (length 750 mm, inner diameter 30 mm) placed in the heating furnace. Figure 7 shows the sketch of furnace setup used in this study. The ends of the mullite tube were closed with stainless steel end caps that had openings for inlet and exhaust gas flows. The precursor coated samples were placed on a ceramic boat that was placed in the tube at the center of the heating furnace as shown in Figure 7.

The thermal treatment consists of three individual steps known as drying, calcining, and reducing steps. In the drying step (also known as dehydrating step), the precursor coated samples were dried at 100 °C for 12 hrs in the ambient atmosphere to eliminate excess water from the samples. Calcination, often referred to as heat treatment or pyrolysis step, was carried out in either oxygen-rich air atmosphere or oxygen-deficient inert atmosphere (argon - Ar). The thermal profile in this step was controlled with a ramp

rate of 10 °C/min and held at 450 °C for 2 hrs. This process of controlled heating was adapted to avoid sintering. In this step the amines and nitrates groups of TAPN decompose thermally forming Pd oxide. The final step known as reduction step includes the thermal gas-phase reduction of Pd oxides to metallic Pd. The thermal and gas profiles in this step were as follows, temperature was held at 500 °C (10 °C/min) for 2 hrs using hydrogen gas as a reducing agent in an inert atmosphere of Ar (H₂:Ar – 1:20). The furnace was allowed to cool down to room temperature in the reduced flow of H₂ and Ar.

(a) Initial Optimization of the Useful Process Parameters

The two of many process parameters of the synthesis process that were analyzed are as follows, concentration of the solute in the aqueous solution and the equilibrium precursor adsorption time. Precursor adsorption time is defined as the time for which the porous carbon support was in contact with or fully immersed in the aqueous TAPN solution. The Pd samples were prepared with varying precursor adsorption time by immersing the support in the as-received concentration (375 mM TAPN) for 10, 30, and 60 minutes. Similarly, the varying or decreasing the molar concentration of TAPN was performed by immersing the support for 30 minutes in 250 mM, 125 mM, and 62.5 mM TAPN solution.

(b) Multiple Coating Process of Palladium

The LPS process with thermal reduction process for fabricating Pd-NPs facilitates repetition of the process for further Pd loading which is done by repeating intermediate steps in a certain sequence. The process of single coating of Pd-NPs can be defined as the fabrication process that involves precursor adsorption, drying, calcining, and reducing steps. Whereas the multiple Pd coating process includes repetition of precursor

adsorption, drying, and calcining steps in a cyclic manner for more Pd deposition followed by a final reduction step. In this study, a single and double coating process of Pd on all the above mentioned supports has been carried out. The carbon foam supports were heat treated in oxygen-rich air environment and the CNT-grafted foam supports were heat treated in oxygen-deficient inert environment of Ar.

6. RESULTS AND DISCUSSIONS: Processing and Characterization

6.1. Initial Optimization of Palladium Deposition

The fabrication of Pd-NPs involves a two stage process; the precursor equilibrium-adsorption stage and the thermal reduction stage. The precursor adsorption time and the concentration of the precursor solution were optimized for the most effective permeation of the precursor solution in the water filled carbon supports. This optimization was accomplished by keeping the other parameters constant.

Initial Optimization of the Process Parameters

This study was carried out on silica coated carbon foam supports of dimensions 10x5x2 mm³. SEM images were taken on the cell walls of first pores across the Pd-fabricated foam samples in order to determine the uniformity of Pd loading across the sample. The variation in Pd loading across the sample was the determinant factor for uniform distribution of the precursor solution determined by the equilibrium adsorption time.

Figure 8 shows the SEM micrographs of first pores for the palladium samples prepared with varying precursor adsorption times. The SEM micrographs shown here are at different first pores in the sample. These micrographs reveal that the carbon foam supports immersed in precursor solution for 10 minutes showed a non-uniform coating of Pd across the sample, whereas the ones immersed for more than 30 minutes had a significantly more uniform coating of Pd across the sample. This suggests that immersing the support for 30 minutes was sufficient enough to obtain an equilibrium permeation of precursor solution in the water filled supports. Although, it is important to note that the high concentration of aqueous precursor solution (375 mM TAPN) used here, resulted in

an undesirable thick layer like coating, but this concentration was very effective to determine the variation in Pd loading with adsorption time.

Figure 9 shows the SEM micrographs of the pores of Pd fabricated foam samples prepared by varying the concentrations of the aqueous precursor solution. The concentrations of 250 mM (10%), 125 mM (5%), and 62.5 mM (2.5%) TAPN were used with a constant precursor adsorption time of 30 minutes. The higher concentrations (125 mM and 250 mM TAPN) of Pd precursor solution yielded micron-sized particles. Samples prepared with the molar concentration of 62.5 mM TAPN solution resulted in Pd particles of nano-dimensions on the carbon foam supports. The amount of particles loading and the Pd film thickness were observed to be decreasing with reduction in the concentrations of precursor solution (from 375 mM to 62.5 mM TAPN) in an orderly fashion. However, some disparities in the Pd particle sizes and dispersions were observed, which can be attributed to the complex geometry of the foam relative to the flat supports.

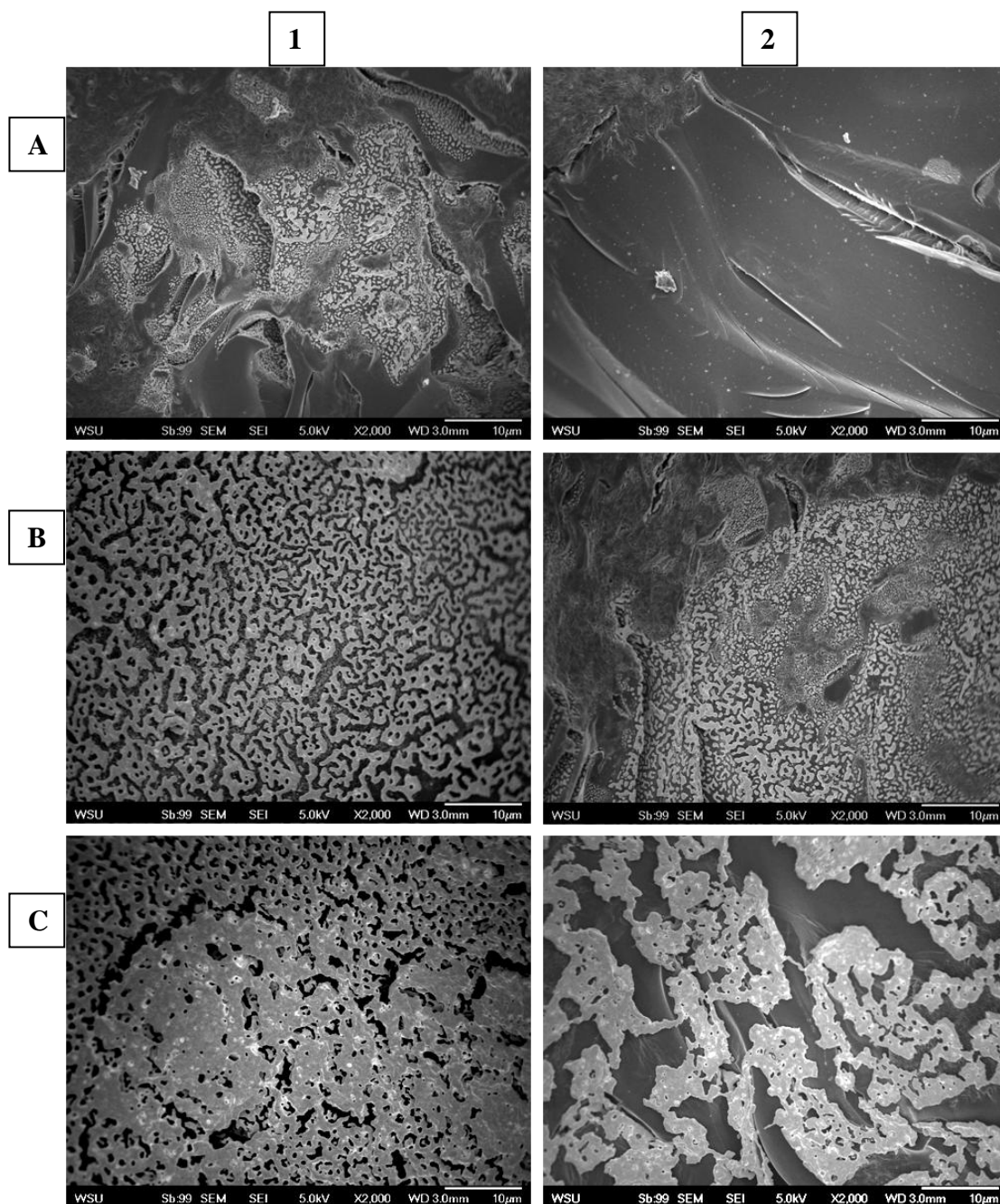


Figure 8 Low Magnification SEM Images of Varying Adsorption Time

(A) 10, (B) 30, and (C) 60 minutes in 375 mM TAPN.

Images Showing Palladium on Two Different First Pores for Each Sample

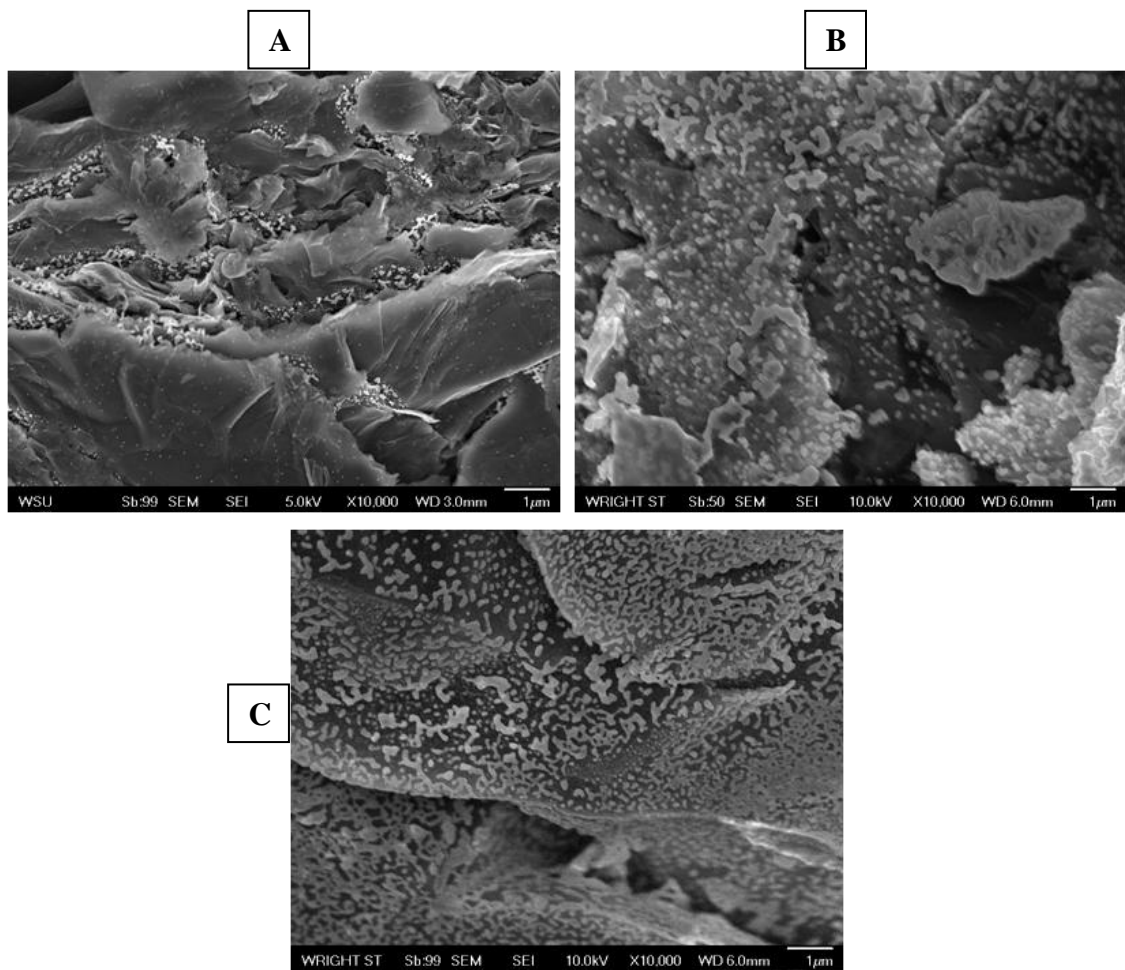


Figure 9 Low Magnification SEM Images of Varying Precursor Concentration
 (A) 62.5 mM, (B) 125 mM, and (C) 250 mM TAPN immersed for 30 minutes.

6.2. Synthesis of Supported Palladium Nanoparticles

As discussed in the experimental section, the fabrication method based on precursor adsorption and thermal reduction process enabled to synthesize one or more number of coatings of Pd-NPs on the supports. In this study, (a) a single coating of Pd-NPs and (b) a double coating of Pd-NPs were fabricated on various pretreated carbon foam supports as well as on CNT-grafted carbon foam supports. The effect that different types of carbon supports may have on the amount of palladium loading will be discussed.

6.2.1. Pretreated Carbon Foam Supports

The pretreatment processes are drafted in the experimental section (see section 5.3.). The influence of palladium loading and dispersion on the pretreated or activated carbon foam supports was studied. For comparative study, three types of pretreated carbon foam supports of dimensions $10 \times 5 \times 2 \text{ mm}^3$ were prepared that are as follows,

- Untreated (pristine) carbon foam support
- Nitric-acid (HNO_3) treated carbon foam support
- Silica-coated carbon foam support

(a) Single Coating of Pd-NPs on Carbon Foam

SEM micrographs of the cell walls of first pores of the untreated, nitric-acid treated, and silica-coated carbon foam supports were taken after Pd-NPs fabrication. Figure 10 shows micrographs of the Pd-NPs synthesized on the untreated, nitric-acid treated, and silica-coated foams via a single coating process.

Relative to the other two supports, silica-coated supports appeared to be the most effective for depositing Pd-NPs. One of the properties of graphitized carbon foam is their

hydrophobic nature. The silica-coated sample consists of a uniform nano-layer of oxide on the surface which enables the porous hydrophobic foam to become durably hydrophilic. It improves the wetting ability of support as well as the interaction with the metal-precursor solution. As a consequence, a high density of Pd-NPs on silica-coated porous foam was obtained as shown in Figure 10C.

An alternative pretreatment method for oxidizing the support with HNO_3 , is a conventional approach that etches the surface. This results in attachment of oxygen functional groups which is desirable for the nucleation of the metal nanoparticles. The nitric-acid treated foam was washed thoroughly with distilled water for two reasons: (i) To stop additional oxidization [89], and (ii) To avoid the effects of varying pH in the precursor solution [74]. But this may result in the discharging or removal of some surface oxygen groups leading to low metal-support interactions. Figure 10B shows the Pd-NPs attached to HNO_3 -treated foam. The untreated foam exhibits a lower density of Pd particles compared to that of the two pretreated foams (Fig. 10A). This difference can be attributed to the insufficient interaction of the untreated foam with the metal-precursor solution and it is also due to the lack of functional groups.

The overall deposition of particles on the foam supports was observed to have some areas with disparity in the particle sizes (unusual particle sizes) and density as well as the sizes of Pd-NPs. This can be attributed to the complex geometry of foam. However, it was inferred that the precursor solution had infiltrated throughout the porous support, since Pd particles were successfully deposited throughout the pores of the foam. But, the amount of Pd loading varies from top-ligament to the inner pores of the foam as shown in Appendix B (Figure B1). The figure B1 reveals that the variations were minimal.

(b) Double Coating of Pd-NPs on Carbon Foam

In an effort to increase the amount of Pd loading, a double coating process of palladium on all the above three types of carbon foam supports was used. SEM micrographs, as shown in Figure 11, reveal that the double coating of palladium significantly enhances the amount of nanoparticles loaded on the support. Remarkably uniform and well-dispersed smaller Pd-NPs were obtained with double coating process as compared to their single coated counterparts. It was also observed that the double coating of palladium on untreated, nitric-acid treated and silica-coated carbon foam samples followed a similar trend of increase in Pd-NPs loading densities, as was seen in the samples with single coating of palladium (untreated < HNO₃ < silica). This indicates that the surface pretreatment plays an important role in the synthesis of Pd-NPs. It was also noticed that the areas with disparity in Pd-NPs loading density were significantly reduced with the double coating process.

It can be concluded from this study that the surface pretreatment of foam improves its wetting ability which improves the interaction of the foam support with the metal-precursor solution as well as alters the surface morphology facilitating active nucleation sites for Pd-NPs.

On the silica-coated foam samples (Figure 10C and Figure 11C), it is important to note that after functionalizing with palladium some irregular nano-patterning of silica, hosting a large number of tiny particles was observed. To the best of our knowledge, such a phenomenon has not been reported earlier in the literature.

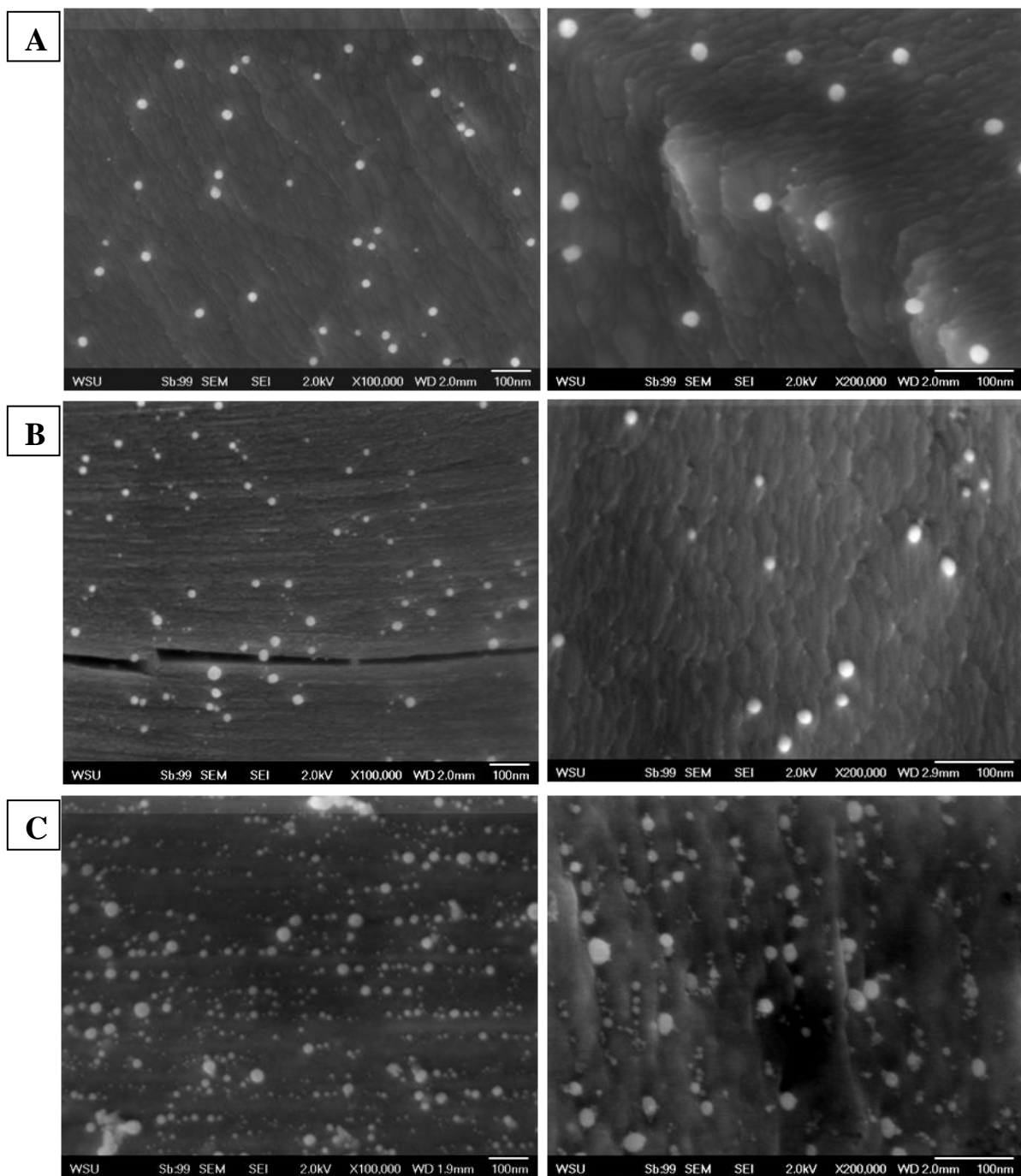


Figure 10 SEM Micrographs of SINGLE Coating of Pd-NPs on Foam Fabricated on (A) Untreated, (B) Nitric-Acid Treated, and (C) Silica-Coated Carbon Foam. Images at 100,000x (Left) and 200,000x (Right) Magnification.

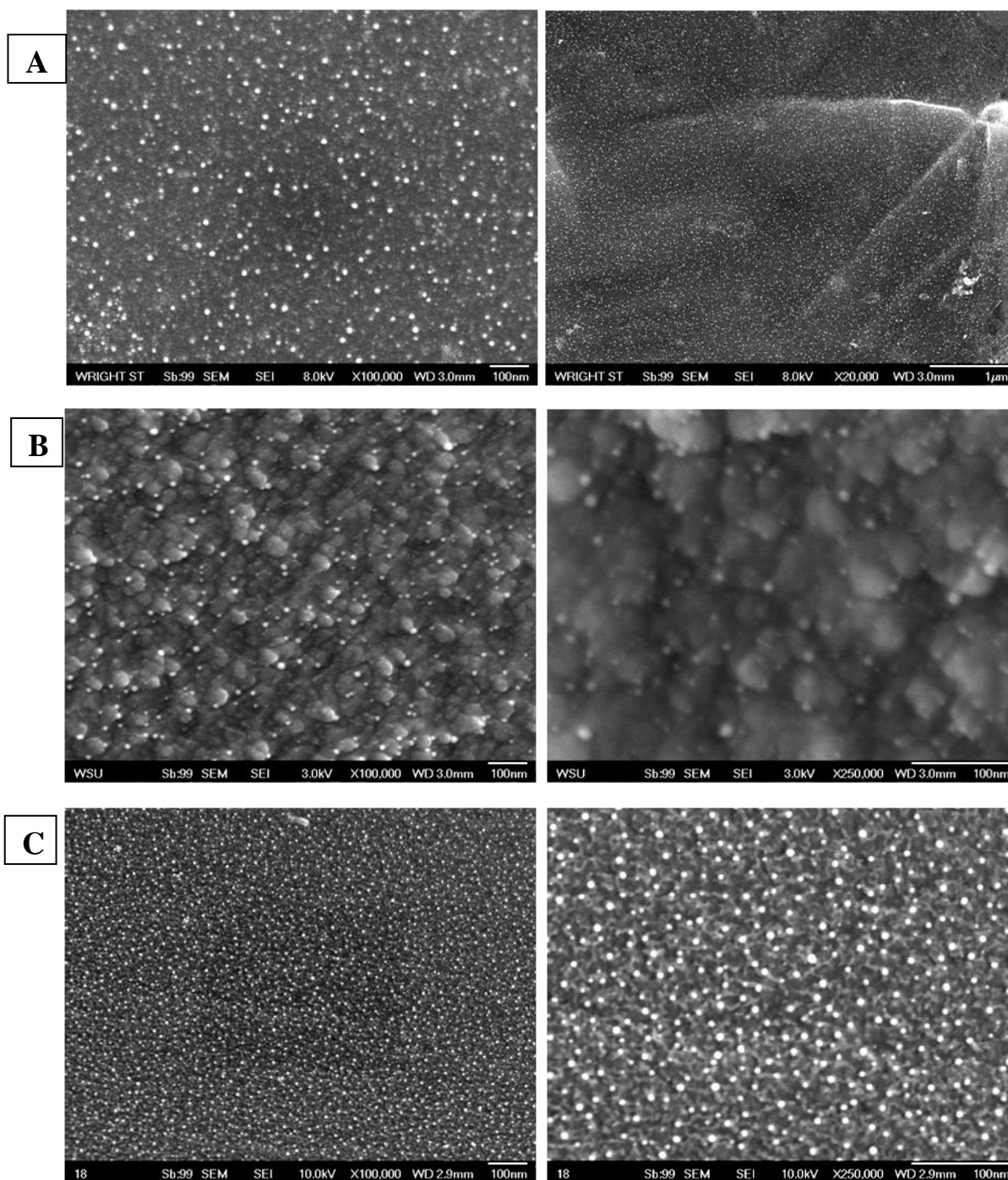


Figure 11 SEM Micrographs of DOUBLE coating of Pd-NPs on Foam

Fabricated on (A) Untreated, (B) Nitric-Acid Treated, and (C) Silica-Coated Carbon Foam. Images on Left 100,000x Magnification

SEM Images on Right Are of Different Magnifications (Lower/Higher)

6.2.2. Hierarchical Supports - Carbon Nanotubes-Grafted Foam Supports

Palladium nanoparticles were fabricated on CNT-grafted foam samples by a similar synthesis process that was used for foam supports. The single coating and double coating process of Pd-NPs on CNT-grafted foam samples were performed in this study. While synthesizing Pd-NPs, the influence of calcining environment on the CNT was also studied and it will be discussed here.

The SEM micrographs (Fig. 2) show that CNT-grafted on carbon foam by a CCVD process may result in forest like nanotubes that provide at least an order of magnitude increase in the available surface area. It is worthwhile to note that the CNT grafted on foam supports were not subjected to any intense pretreatment process in order to activate the surface prior to attaching metal NPs, as often discussed in the literature [90-91]. Nevertheless, the supports were cleaned with methanol and water prior to dipping in precursor solution to overcome the low wettability of CNT. This was done. The high surface tension of water was overcome by the low surface tension of methanol, which resulted in the wetting of the hydrophobic surface. This process is sometimes referred as “breaking the surface tension”, in which water is made to wet hydrophobic materials. The CNT that were grown by the CCVD method as discussed in experimental section (a) were prone to bends and twines that may result in nanosized structural defects, and (b) also have functional groups (e.g. -COOH) attached to it (CNT). Such functional groups were present by default from the growth process. However, this proved to be very advantageous because no pretreatment step was required that could otherwise result in some degree of damage to the CNT. It may also introduce undesirable alien agents resulting in surface contaminations.

(a) Influence of the Calcining Environment

Calcining environment is the environment in which the supports were heat treated at elevated temperatures (above 400 °C). This step in the thermal treatment, removes the amines and the nitrates of the tetraamine precursor solution from the support. In the process of making Pd-NPs on the CNT-grafted foam supports, the supports were subjected to calcining steps in the following two environments.

- Oxygen-rich environment (air)
- Oxygen-deficient inert environment (Ar)

Figure 12 shows SEM images for Pd-NPs fabricated CNT samples, calcined in air atmosphere. The CNT were observed to be thermally decomposing when calcined in air (Fig. 12). However, when the samples were calcined in an inert atmosphere of Ar no decomposition of CNT was observed (Fig 13). Although it was inferred (qualitatively) that a leak in the inert environment system at 450 °C over a period of 2 hrs could cause damage to the CNT. Therefore, to preserve the CNT and its hierarchical nature, Pd-NPs were fabricated on the CNT samples in oxygen deficient inert atmosphere of argon and care was taken to avoid gas leaks in the system.

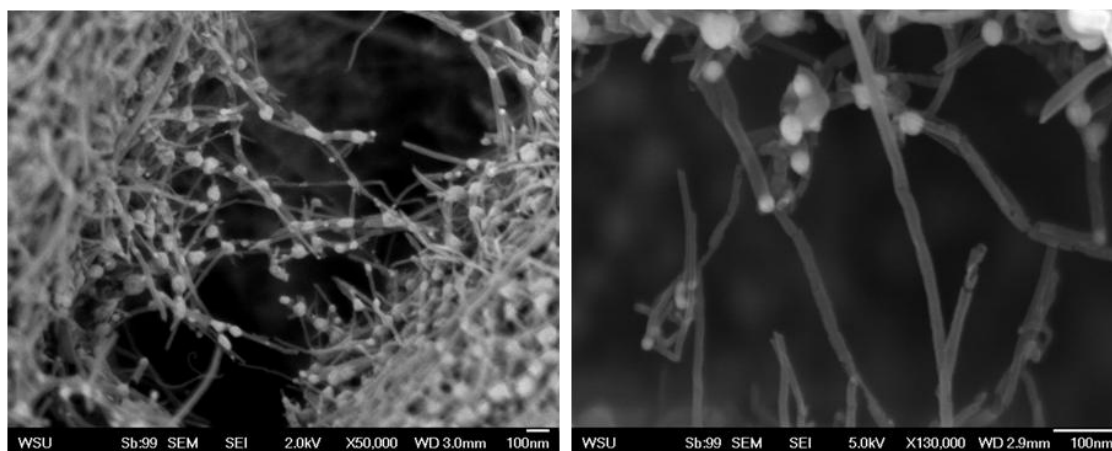


Figure 12 SEM Micrographs Showing Thermal Decomposition of CNT, Heat-Treated in the Oxidizing Environment

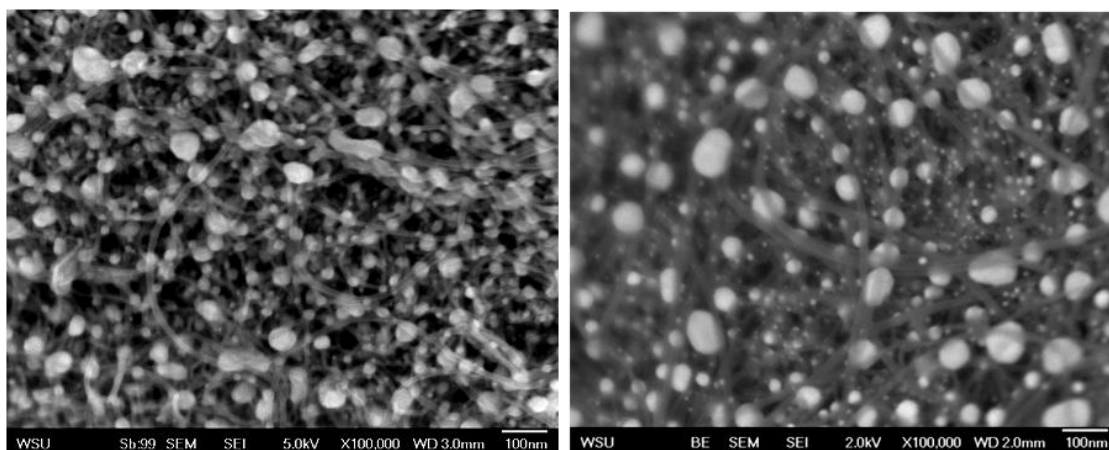


Figure 13 SEM Micrographs of Pd-NPs on CNT-Grafted Foam Fabricated by SINGLE Coating Process Using 62.5 mM TAPN

(b) Single Coating of Pd-NPs on CNT

Figure 13 shows the SEM micrographs of Pd-NPs attached to the CNT-grafted foam sample by the single coating process using 62.5 mM TAPN solution in an Ar environment. It was evident that large number of Pd-NPs were obtained on CNT-grafted foam samples, showing a remarkable increase in the number of nanoparticles per area of the sample. The high surface area available by attaching CNT plays a vital role for Pd-NP nucleation. The high density of Pd-NPs loading can also be attributed to the strong interactions of CNT-grafted foam support with the metal precursor solution. Figure 14 shows the SEM image of Pd-NPs on CNT-grafted foam that was prepared by a lower concentration of TAPN solution (25.0 mM) which has smaller Pd-NPs. But the analysis of Pd-NPs on the CNT samples presented in this thesis was carried out on samples prepared only with 62.5 mM TAPN solution (same concentration as used for foam). The amount of Pd-NPs loading has some variations from top-ligament to the inner pores as shown in Appendix B for a CNT-grafted foam sample (Figure B2).

(c) Double Coating of Pd-NPs on CNT

The double coating method of fabricating Pd significantly increases the amount of Pd loading on the supports. The SEM micrograph in Figure 15 shows the double coated Pd-NPs on CNT-grafted foam samples (62.5 mM TAPN). There is a remarkable increase in the amount of Pd-NPs attached onto the CNT forest. It was also observed that the particle sizes invariantly increased with double coating method on CNT samples. This result was in contrast to that of carbon foam supports, where the mean particles size decreased with the double coating method.

The particles obtained on both single and double coated Pd on CNT-grafted supports were much larger when compared to that on the carbon foam supports. Such an effect can be attributed to the (i) high interaction of CNT with the precursor solution, (ii) high concentration of precursor solution and/or (iii) the heat treating environment. The Pd-CNT samples were calcined at elevated temperatures in the inert (Ar) atmosphere. From literature, it has been inferred that the mobility of particles is enhanced due to the absence of oxygen or decomposition of anchored oxygen groups, those resulting in sintering of particles [74, 92].

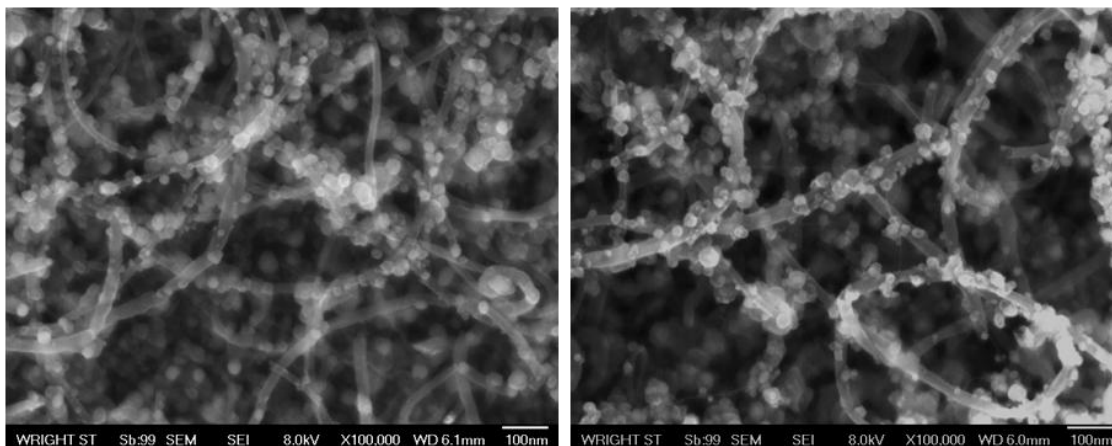


Figure 14 SEM Micrographs of Pd-NPs on CNT-Grafted Foam Fabricated by SINGLE Coating Process Using 25 mM TAPN

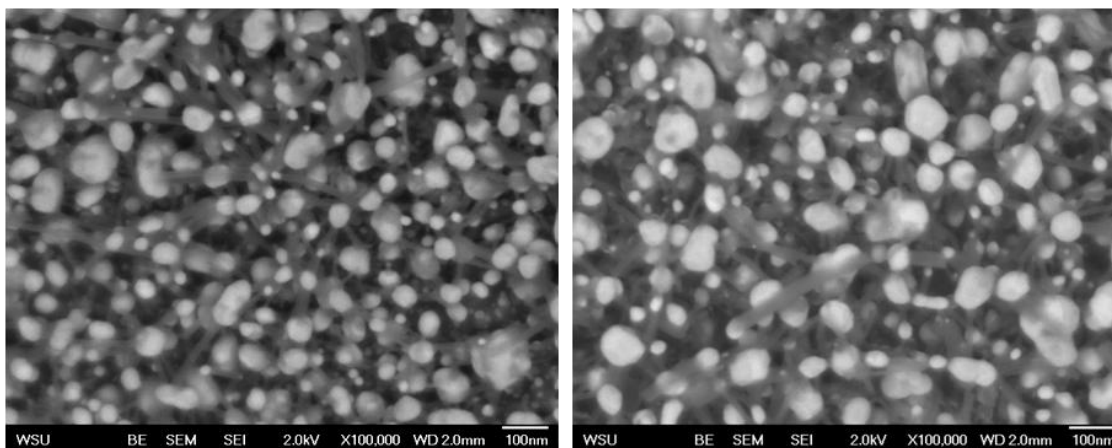


Figure 15 SEM Micrographs of Pd-NPs Fabricated on CNT-Grafted Foam by DOUBLE Coating Process Using 62.5 mM TAPN

6.3. Statistical Analysis

This chapter provides an outlook to the quantitative analysis that was carried out to offer a better understanding of the fabrication process of Pd-NPs. The statistical analysis on SEM micrographs was performed using the scandium SEM software as described in the characterization techniques section. This section contains the following data:

- The size distribution of Pd-NPs for all the samples
- Contact angle measurements of Pd-NPs on CNT
- The number of Pd-NPs per unit length of CNT in CNT-grafted foam samples
- The number of Pd-NPs per unit area of the supports
- Surface area calculations of Pd-NPs on all sample types

6.3.1. Nanoparticles Size Distribution Profiles

The particle size distribution profiles of single and double coated Pd-NPs on the different supports were obtained by analyzing SEM micrographs. The SEM micrographs of the various first pores (3 to 10 were observed) of high magnifications were taken for all the Pd-NPs fabricated foam and CNT samples. At least two samples for each type of support were analyzed. To determine the dispersion and density of Pd particles, SEM micrographs were chosen to be as representative of bulk sample as possible and but were biased so as to avoid the irregular patterned (patchy) areas. The irregular area of Pd deposition is referred as areas that have unusual sizes of NPs (greater than 50

nm on foam supports) and such areas contribute to only much smaller percentage of the sample.

Figures 16-18 show the size distribution profiles for single and double coatings of Pd-NPs on the untreated, nitric-acid treated and silica-coated carbon foam supports. The size distribution graphs for the single coating of Pd on foam supports tails towards the larger diameters indicating disparity in the particle sizes. This tailing for the double coated samples mostly disappeared leading to a smaller mean particle diameter in these samples.

The distribution profiles associated with single and double coated Pd-NPs on CNT supports are shown in Figure 19. It should also be noted that, due to the presence of larger particles on the CNT-support samples, the scale in Figure 19 has been expanded to show particles sizes up to 50 nm. The double coated CNT support shows a much broader size distribution than single coated CNT support, a result in contrary with the narrow size distribution of double coating of Pd on bare foam supports. The Pd particles on CNT supports were of diameters ranging from 5nm-150nm.

6.3.2. The Number of Pd Nanoparticles Attached Per Micron Length of CNT

This analysis was done on three samples of a single coating of Pd on CNT. In order to determine number of NPs per unit length of CNT, at least 25 images including both SEM and scanning-transmission mode (STEM) images were analyzed. Figure 20 shows the SEM including the scandium image and a STEM image. SEM image analysis resulted in 28 Pd particles where as STEM image analysis revealed a close result of 33 Pd particles, averaging the two to 31 particles per unit micron length of CNT (N_{Pd-CNT}).

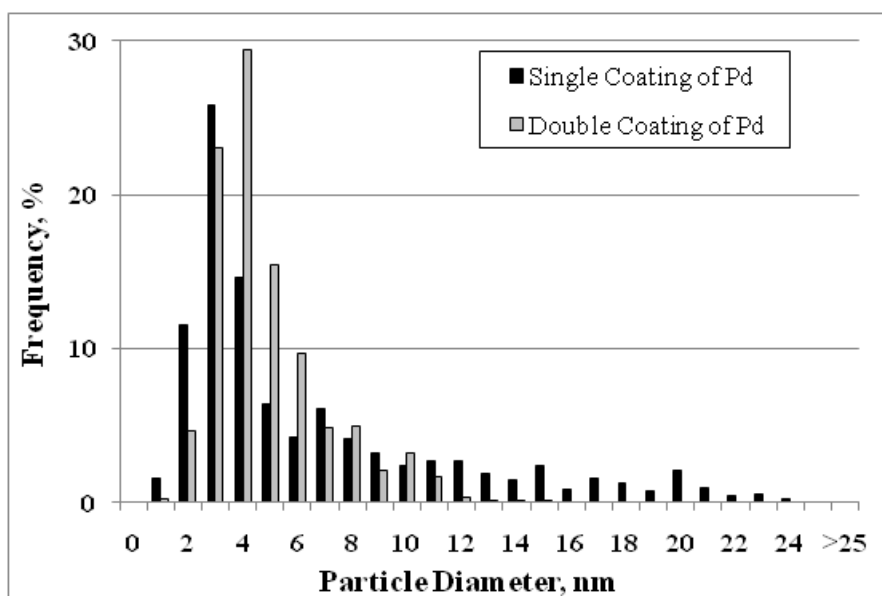


Figure 16 Particle Size Distribution Profiles – UNTREATED CARBON FOAM
Comparing Single and Double Coating of Palladium

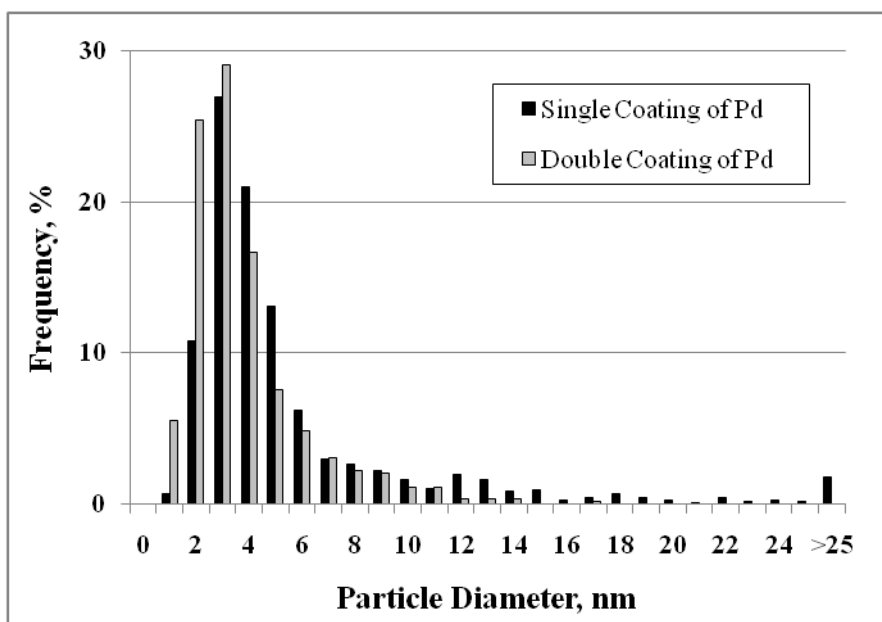


Figure 17 Particle Size Distribution Profiles – NITRIC-ACID TREATED CARBON FOAM
Comparing Single and Double Coating of Palladium

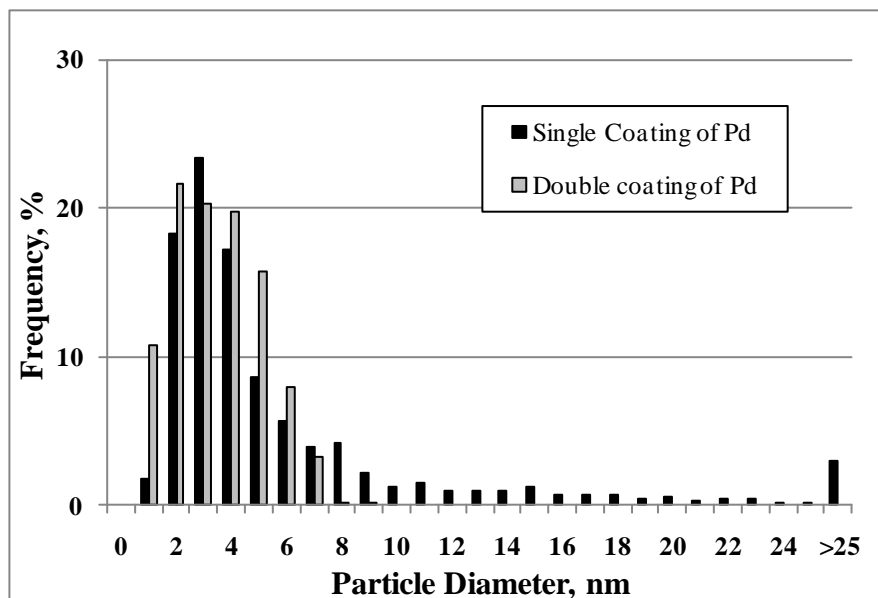


Figure 18 Particle Size Distribution Profiles - SILICA COATED CARBON FOAM
Comparing Single and Double Coating of Palladium

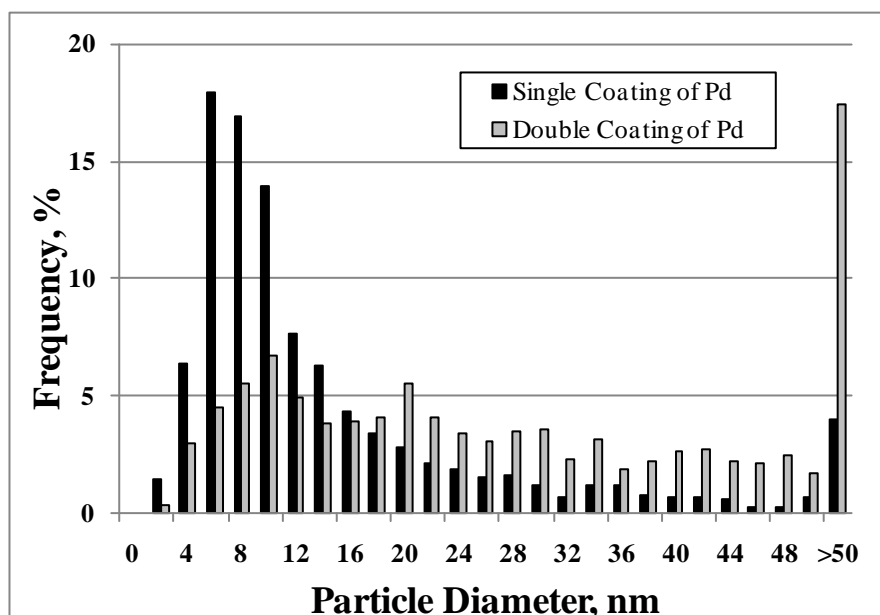


Figure 19 Particle Size Distribution Profiles - CNT-GRAFTED CARBON FOAM
Comparing Single and Double Coating of Palladium

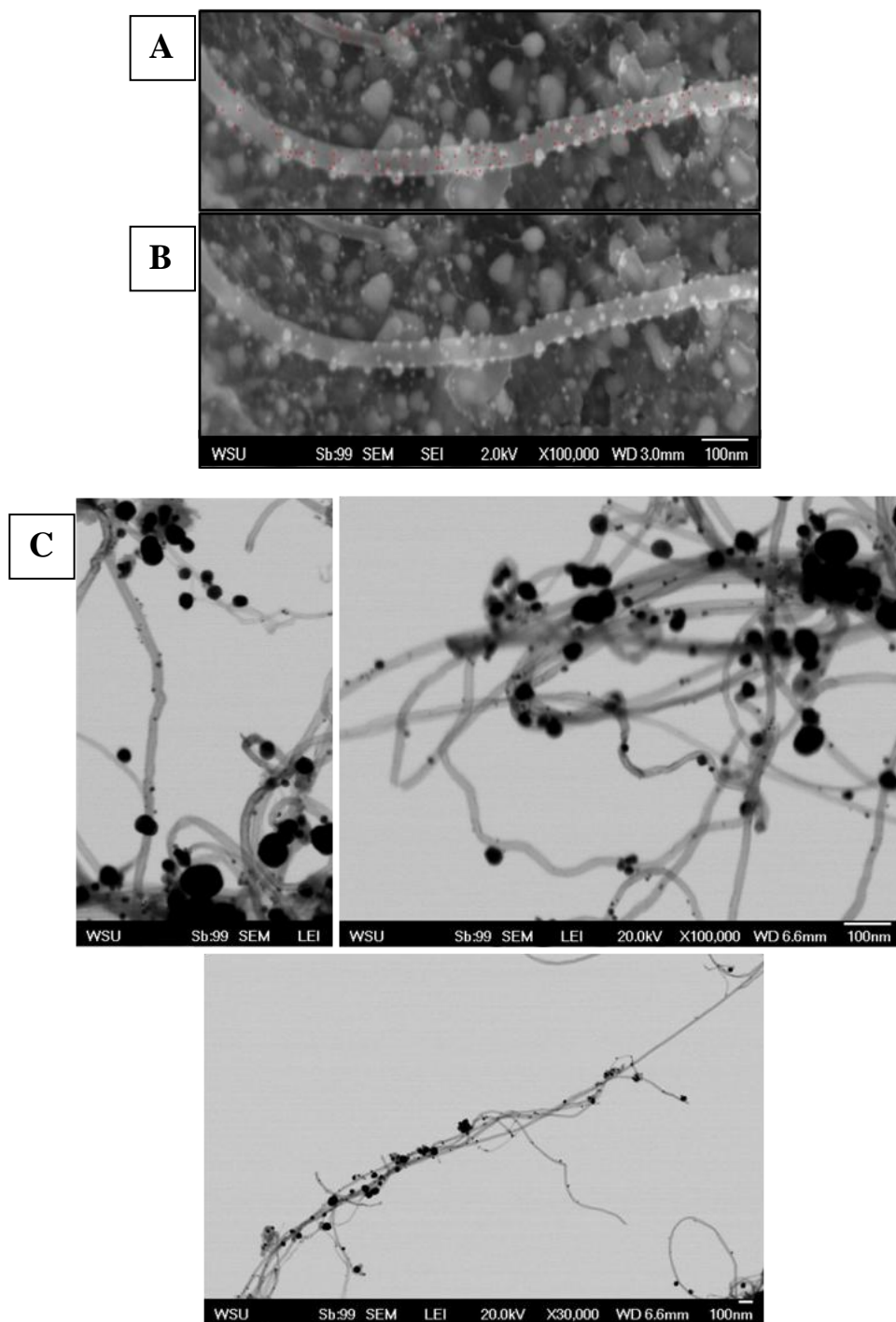


Figure 20 SEM and STEM Micrographs for Analysis of Pd- NPs Per-Unit Length of CNT

Palladium Nanoparticles Attached to CNT (A) Scandium Marked Points on SEM (B) Original SEM at 100,000x Magnification, and (C) STEM Micrographs of Pd-NPs Attached to CNT (Different Magnification).

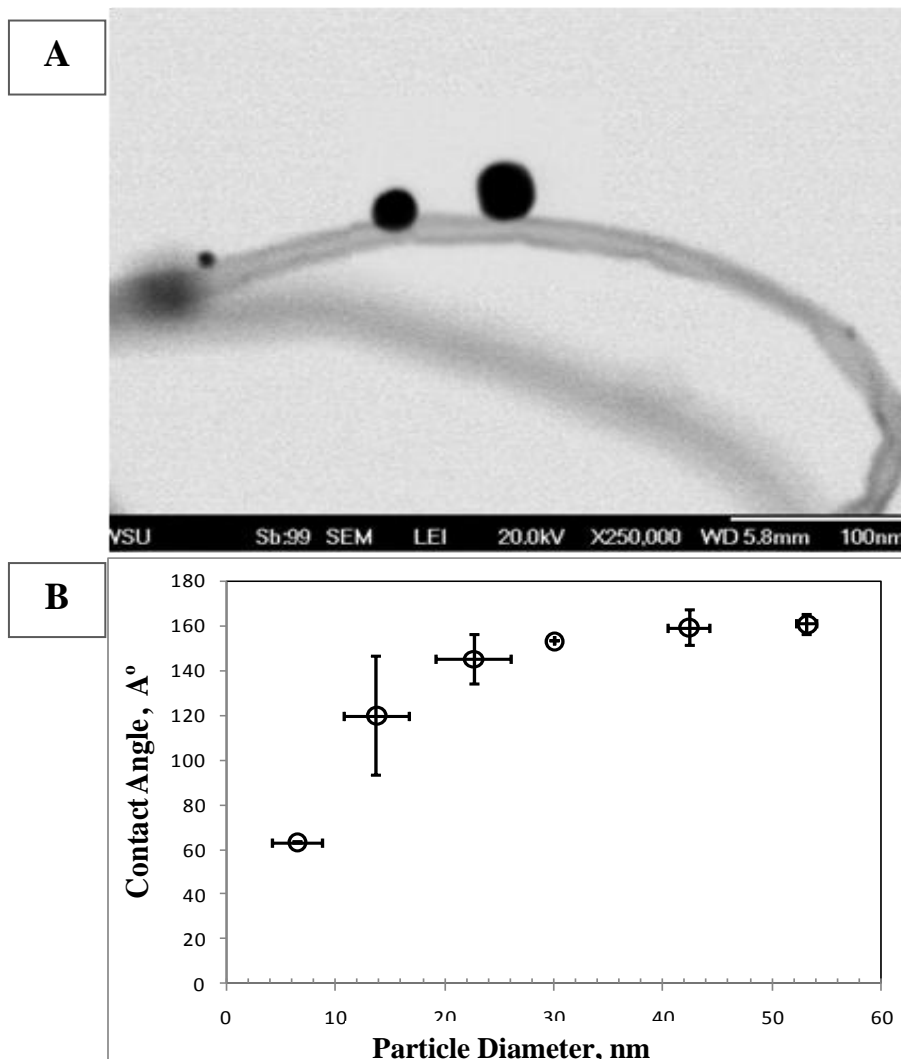


Figure 21 Contact Angle Measurements - Palladium Nanoparticles on CNT

(A) STEM Image of Pd-NPs on CNT-grafted foam (B) Graph Representing Size Dependent Contact Angle Measurements for Pd-NPs on CNT

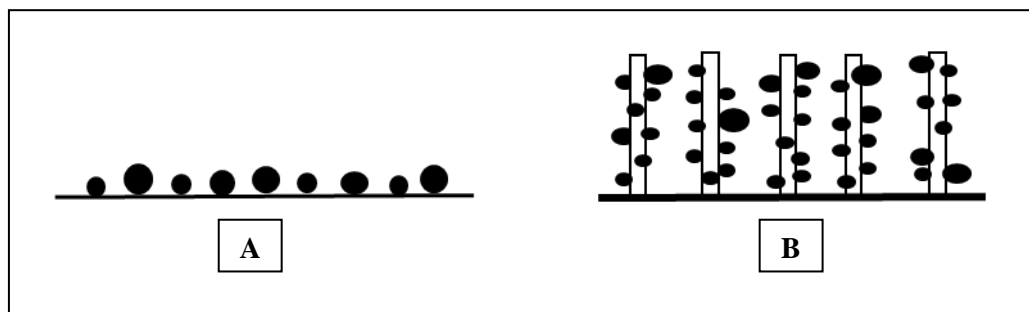


Figure 22 Schematic Representation of Nanoparticles on the (A) Foam Support and (B) CNT-Grafted on Foam Support

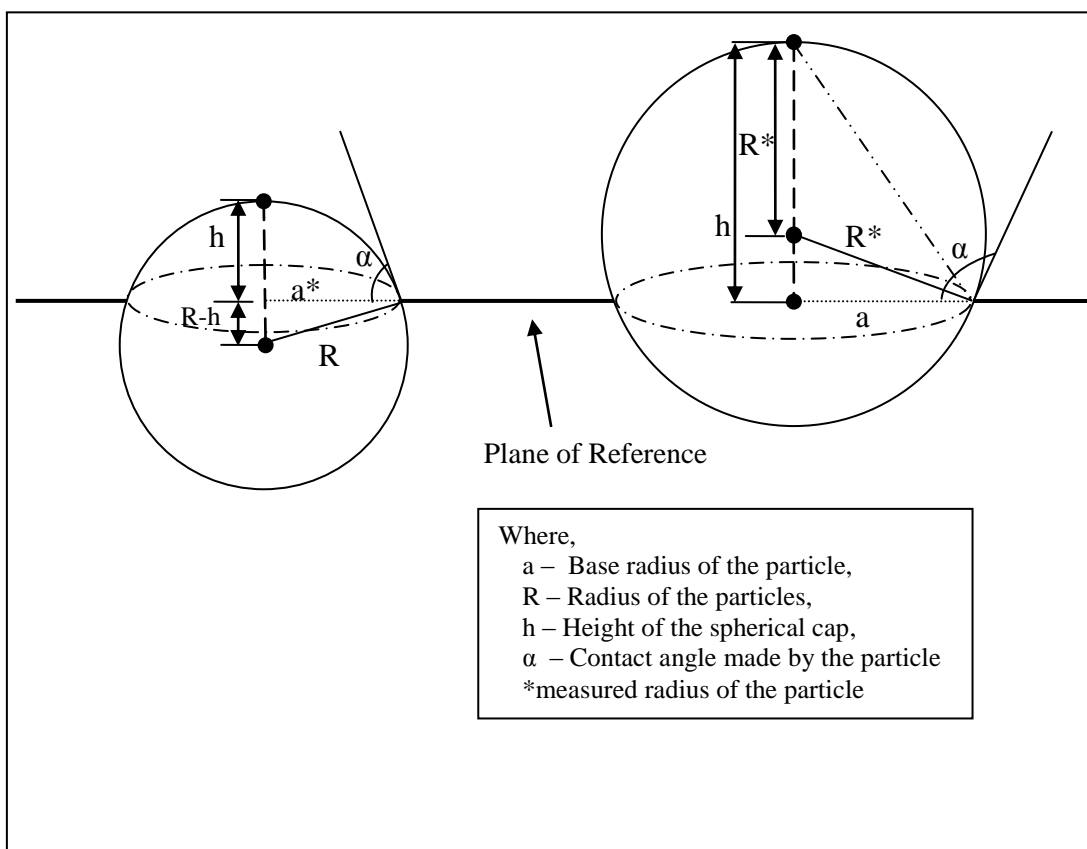


Figure 23 Schematic Representation of the Contact Angle Made by the Particle With the Support Surface

Re-drawn from reference [94]

6.3.3. Contact Angle Measurements of Pd-NPs on CNT

For the contact angle measurements of Pd-NPs on CNT samples, both SEM and transmission mode STEM images were analyzed using Scandium© angle tool. The images were collected for the particles that were visibly sitting on the edge of the CNT (from SEM incident viewpoint) as shown in Figure 21A. The contact angles for over 30 particles in the size ranges of up to 50 nm attached to CNT (of sizes ranging from 10 nm – 25 nm) were determined. The obtained data reveals that the contact angle of particles on CNT is a size dependant phenomenon given these conditions. Figure 21B shows the graph of contact angle as a function of particles diameter plotted with standard deviations obtained on both axes. This analysis showed that the Pd particles of sizes less than 10 nm show a hemisphere shape having contact angles ‘less than’ $< 90^\circ$ and the particles above 25 nm tend to stand out on the CNT having a contact angle ‘greater than’ $> 150^\circ$. Even though the contact angle data could only be taken on CNT supports, we have assumed same contact angle distribution for all the supports.

6.3.4. The Number of Pd-Nanoparticles Per-Unit Area of the Support

The statistical data such as mean diameter and standard deviation obtained from size distribution analysis for all the supports are summarized in Table 1. Also the SEM images were used to obtain the total number of particles per area (μm^2) of the carbon foam supports. These are tabulated in Table 1 as #Pd-NPs/ μm^2 . This analysis is quite straight forward on a relatively flat surface such as cell walls of foam, but not suitable for a hierarchical support such as CNT-grafted on foam.

Figure 22 shows the schematic representation of the Pd-NPs attached on the carbon foam (A), and CNT-grafted foam samples (B). But with the SEM area image

analysis, only the upper region of CNT can be analyzed shadowing the region beneath it. Therefore, when analyzing with SEM area micrographs the count of Pd-NPs per image is necessarily underestimated. A complete different route as discussed below was implemented to minimize the shadowing effects.

Total number of Pd-NPs per unit area (μm^2) for single coated Pd on CNT-grafted foam samples is given by the following equation,

$$N_{Pd}^a = N_{Pd}^{l_{CNT}} * l_{CNT} * N_{CNT}^a$$

Where,

N_{Pd}^a - Estimated number of Pd-NPs per unit area of overall support surface (μm^2)

$N_{Pd}^{l_{CNT}}$ -Average number of Pd-NPs per unit length of CNT (μm)

l_{CNT} -Average length of CNT grafted on the support

N_{CNT}^a -Estimated number of CNT per unit area (μm^2)

The average number of CNT grown per μm^2 has been estimated in earlier research [29, 93]. In this study, the silica coating time is 15mins and CNT growth time is 20mins.

Based on that, following assumptions have been made,

1. The average length of CNT (l_{CNT}) was assumed to be 10 μm .
2. Both SEM and STEM images individually does not provide complete information.
 - In SEM images, Pd-NPs hosted on the other side of CNT (side other than being imaged) were being shadowed.
 - In order to perform STEM analysis, some CNT were scrapped off the surface of foam.

3. Some Fe-NPs native to CNT growth process may be present in the CNT-supports that can be mistakenly counted as Pd-NPs. But, the number of Fe-NPs is much less than the number of Pd-NPs present in the sample.
4. The Pd-NPs per unit length of the CNT were counted independent of the size of particle i.e. no size distribution of the NPs was made across the length of CNT.

The data obtained from this analysis is calculated using the above equations and assumptions. These results are tabulated in Table 2.

6.3.5. Surface Area Calculations of Pd-NPs

For the average particle sizes of 5 – 6 nm as observed for foam samples (Table 1), the contact angle of particle is considered to be 60° based on the earlier assumptions (Section 6.3.3.). For an average particle size of 15 nm as observed for CNT supports (Table 1) the contact angle is considered to be 120° (Fig 21B).

The surface area of such particles is calculated using the formula for the surface area of the spherical cap as shown in the Figure 23 [94]. The surface area of the spherical cap i.e. the surface area of the deposited Pd-NPs, S_{NP} , is given as,

$$S_{NP} = \pi(a^2 + h^2)$$

And, the volume of the spherical cap is given as,

$$V_{NP} = \frac{\pi}{6}h(3a^2 + h^2)$$

Table 1 Statistical Data Obtained from the Graphical Representations of the Various Samples

Estimated Available Surface Area and Volume of Pd-NPs per unit Area of the Support

Single Coating of Pd-NPs				
Type of Foam	Mean (d) \pm SD, nm	#PdNPs/ μm^2	Surface area Pd, $10^{-3} \mu\text{m}^2$ (Per μm^2)	Volume Pd, $10^{-6} \mu\text{m}^3$ (Per μm^2)
Untreated	6.6 ± 5.2	282	13	10
HNO ₃ Treated	5.9 ± 6.0	382	14	10
Silica Coated	6.1 ± 6.3	988	38	28
CNT Grafted	15.1 ± 15	71100*	150×10^3	842×10^3
* Obtained from the Table 2				
Double Coating of Pd-NPs				
Untreated	5.3 ± 4.2	765	22	14
HNO ₃ Treated	5.4 ± 3.8	987	30	20
Silica Coated	4.7 ± 3.2	2118	49	27
CNT Grafted	30.3 ± 22	-----	-----	-----

Table 2 Number of Palladium Nanoparticles Per Unit Length of CNT

Single Coating of Pd-NPs	#Pd-NPs per micron length (μm) of CNT (A)		Estimated # CNT per μm^2 (B) Ref -	Average length of CNT (μm) (C)	Estimated # Pd-NPs/ μm^2 100% coverage of CNT (A*B*C)
CNT Grafted Foam	SEM	28	237	10	71100
	STEM	33			
	Average	30			

Compositional XPS and EDAX Analysis

The quantitative compositional study was performed on highly oriented pyrolytic graphite (HOPG), a flat model support which has similar surface chemistry as that of carbon foam (See Section 1.5.3). This enables better characterization for the Pd nanoparticles grown on graphite surfaces with and without a forest of carbon nanotubes unlike uneven foam surfaces. Pd-NPs were fabricated on HOPG using identical conditions to the single coating synthesis process as was used for fabricating Pd-NPs on carbon foam supports.

XPS analysis was carried out using monochromatic Al-K α (1486.6 eV) in ultra high vacuum environment (UHV $\sim 10^{-9}$ Torr). The X-ray source at a power of 120W with a 10mA emission current was used. A charge neutralizer was used to neutralize the charge in the sample. Spectra were taken in the analyzer mode of pass energy 20eV. The survey scans also known as general scans (BE: 1000eV-0eV) were taken in retarding sweep modes on each sample. The high resolution fine scans were also collected for performing quantitative chemical analysis. In order to correct the static charge (if any) in the samples, a value of 284.4eV was assigned for C1s spectrum, which is a well known value for HOPG samples [95]. Peak processing and quantification was done on CasaXPS© provided for Windows© PC and the peak intensities were converted into atomic percents using predefined RSF (relative sensitivity factors) for the respective elements provided by CasaXPS© Library.

6.3.6. XPS Analysis Done at Intermediate Steps of the Synthesis Process

A detailed XPS analysis was carried out to provide an insight to the experimental approach presented in this study. The Pd-NPs synthesis process used in this study is a

two stage technique that includes adsorption stage and thermal reduction stage. It can further be classified into four intermediate steps: adsorption, drying, calcining, and reducing. The chemical characterization of growth mechanism was carried out on the untreated bare graphite (HOPG) to rule out the effects caused by other parameters (like coating of silica, or iron catalyst from CNT). The intermediate Pd-HOPG samples were prepared by terminating the process at the appropriate intermediate steps.

The chemical characterization and growth mechanism studies via XPS were carried on the following five types of samples described briefly as given below (refer to section 5.5 for additional experimental details).

1. '*Pristine sample*' (Sample ID: I) – The untreated HOPG was cleaned with a lint-free paper and used as a reference HOPG sample.
2. '*Control sample*' (Sample ID: II) – The control sample is the reference sample for precursor solution. This sample was prepared at adsorption step, which determines the interaction of precursor (TAPN) with carbon support. The sample was retained from precursor solution and was allowed to dry (no heat applied) for about 12 to 24 hours.
3. '*Dried sample*' (Sample ID: III) – The sample was obtained by terminating the synthesis process after the drying step. After the sample was retained from the precursor solution, it was immediately dried in atmospheric air for 12 hours at 100°C to remove excess water. It was then cooled down to room temperature in air atmosphere.
4. '*Calcined sample*' (Sample ID: IV) – The calcined sample was prepared by terminating the synthesis process after the calcining step. After the sample was retained from precursor solution, it was heat dried (as in drying step) followed by

calcination in the oxygen-rich (air) environment for two hours. It was then allowed to cool down to room temperature in air atmosphere.

5. '*Reduced sample*' (Sample ID: V) – The reduced sample is typically similar to the final Pd sample that was obtained by performing the synthesis process completely as discussed in experimental section. The sample was reduced in the H₂/Ar environment and was allowed to cool down in the reduced flow of H₂/Ar.

The XPS survey-scans and fine-scans were taken for the above mentioned five types of samples (at least two samples for each type). The survey scan consists of low-resolution peaks that will provide a quick outlook to the various elements present in a particular sample. Semi-quantitative compositional analysis was also obtained from the survey-scans. A detailed investigation was done on high resolution fine-scan peaks obtained for the core level (orbital) spectra of the corresponding elements. By examining the binding energy (BE), full width at half maximum (FWHM), and the intensities of the component peaks, relative quantitative surface compositional analysis was obtained for the above mentioned samples.

Figure 24 shows the XPS survey-scan collected for the pristine HOPG sample (sample I). The peaks observed in the survey scans are at positions that are assigned to carbon and oxygen peaks. The annotation displayed in the Figure 24 is the semi-quantitative values for surface compositions. It was calculated using quantification regions on the low resolution survey spectrum. The estimated semi-quantitative relative concentration of oxygen on the surface of pristine-HOPG is 6.8 At% as obtained using XPS RSF. It signifies that HOPG comprises mostly of carbon and small amounts of oxygen which is mainly due to surface oxidation of graphite in the ambient environment.

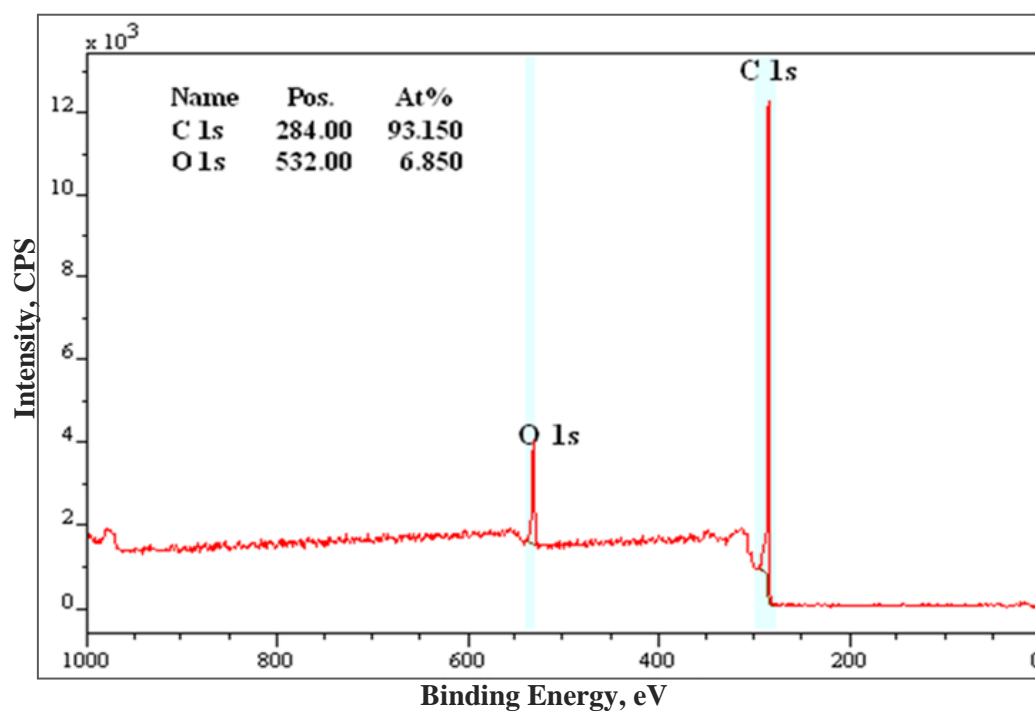


Figure 24 Survey-Scan of Sample I (Pristine HOPG)

The fine-scan of C 1s for HOPG shows an asymmetric peak shape that tails towards the higher binding energy as shown in Figure 25A. Sacher et al. have determined that asymmetry in the peak shape occurs due to the presence of multitude symmetric peaks which represents the subtle differences in bonding of carbon and a few contribute to their shake-up peaks in combinations [96, 97]. The symmetric component peaks of C 1s are designated as shown in Figure 25B (adopted from literature) [97]. The prominent peak C1 at 284.4 eV corresponds to C-C bonding (undisturbed sp² hydrocarbon structure), indicating that HOPG is in graphitic form. The C2 peaks at 285.0 eV represent the disturbed sp² hydrocarbon structure and C3 at 286.0eV indicates sp³ type C-O-bonding that are usually bonded to the exposed graphite surfaces. C4 and C5 peaks at 288.6 eV and 291 eV corresponds to the shake-up peaks ($\pi \rightarrow \pi^*$) of C2 and C1 respectively [96-99]. The resolved C 1s peak for HOPG can be represented by either multiple symmetric peaks or one asymmetric peak as shown in Figure 25C [97, 100-101]. For simplicity one asymmetric peak is used in this study to fit the C 1s peak of the pristine HOPG, which is used as a reference peak shape for C 1s in all the samples. The O 1s peak (Fig 25D) at 532.3 eV for HOPG has been fit to a single component peak (O1) which can be attributed to the surface oxygen groups [100]. Trace amounts of sulfur ('much less than' << 1 At%) was observed (not included) in the pristine HOPG.

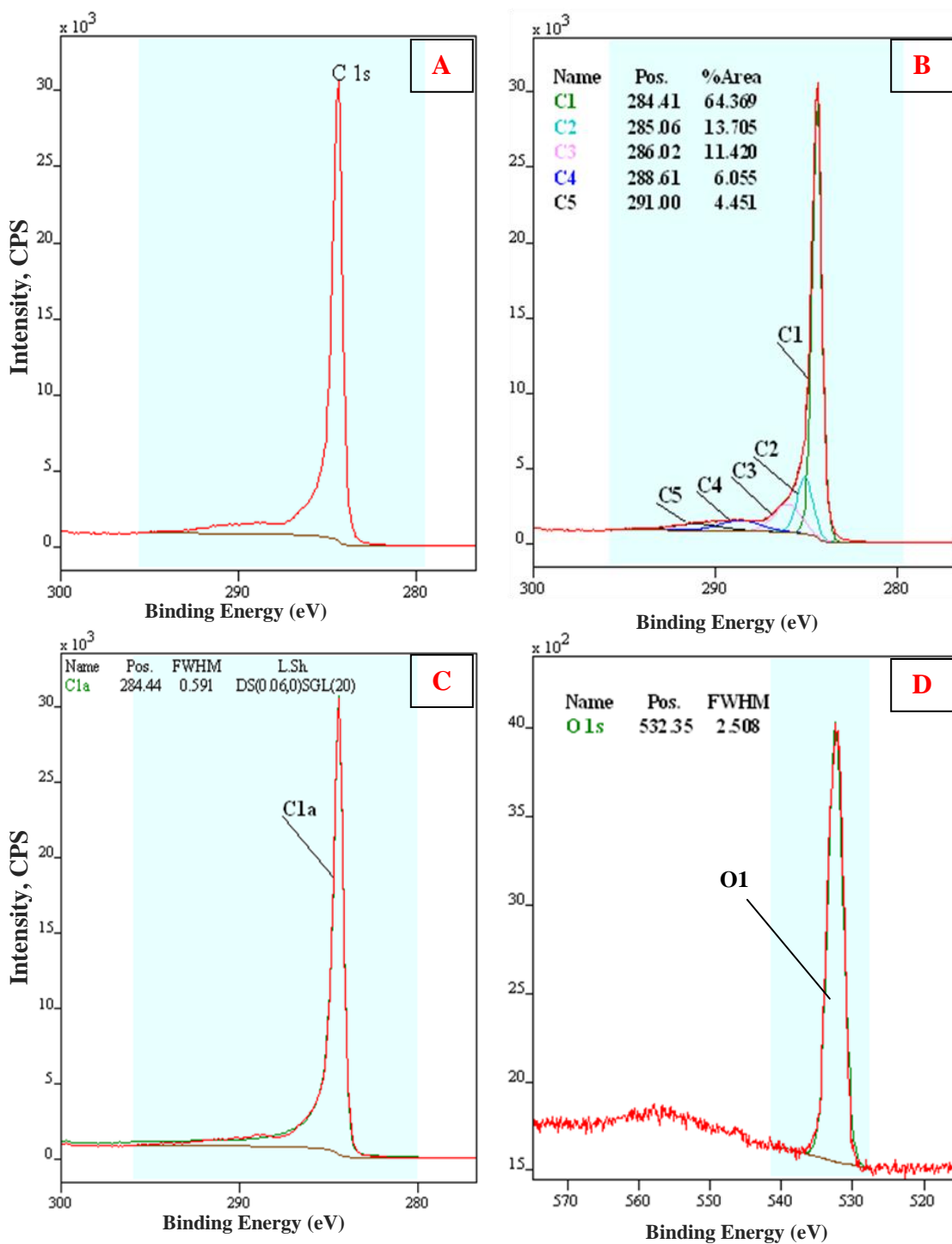


Figure 25 Fine-Scans of C 1s and O 1s of Sample I (Pristine HOPG)

(A) C 1s - Asymmetric Peak, (B) Component Peaks Fit to C1s, (C) C1a - Asymmetric Peak Fit to C 1s, and (D) O 1s – Symmetric Component Peak Fit.

Survey Scan of Sample II-V:

Figure 26 shows the survey scans of the samples II-V: control, dried, calcined, and reduced samples which were prepared at the intermediate steps of adsorption, drying, calcining, and reducing respectively. In Figure 26, the annotations in the left are the semi-quantitative or low resolution spectral analysis obtained from the survey scan of the respective samples. While the scans exhibit strong signals of carbon (C 1s), oxygen (O 1s), and palladium (Pd 3d) peaks obtained from all the four samples as shown in Figure 26, the nitrogen (N 1s) peak, an obvious peak from the tetraamine palladium nitrate compound, is barely seen (present only for control and dried samples) in the survey scans. Fine scans are used to investigate the elements or compounds present in these samples.

Carbon 1s Fine Scans

The C 1s spectra of the samples II-V are the peaks similar to C 1s peak of pristine HOPG samples as shown in Figure 27. The asymmetric peak shape of C1a from pristine HOPG was used to fit the C 1s spectrum. The position of C1 peaks were corrected for charging to 284.4 eV in the samples, where the as-measured and the true values are given in Table 3. The inset in Figure 27 shows that with respect to the large signal count of carbon in HOPG, the spectrum shows minimal variations in the intensities and FWHM (Table 3). This makes it difficult to notice any subtle changes that might have occurred in the carbon bonding at various intermediate processing steps. The BE values, FWHM, elements/compounds atomic percents are tabulated in Table 3.

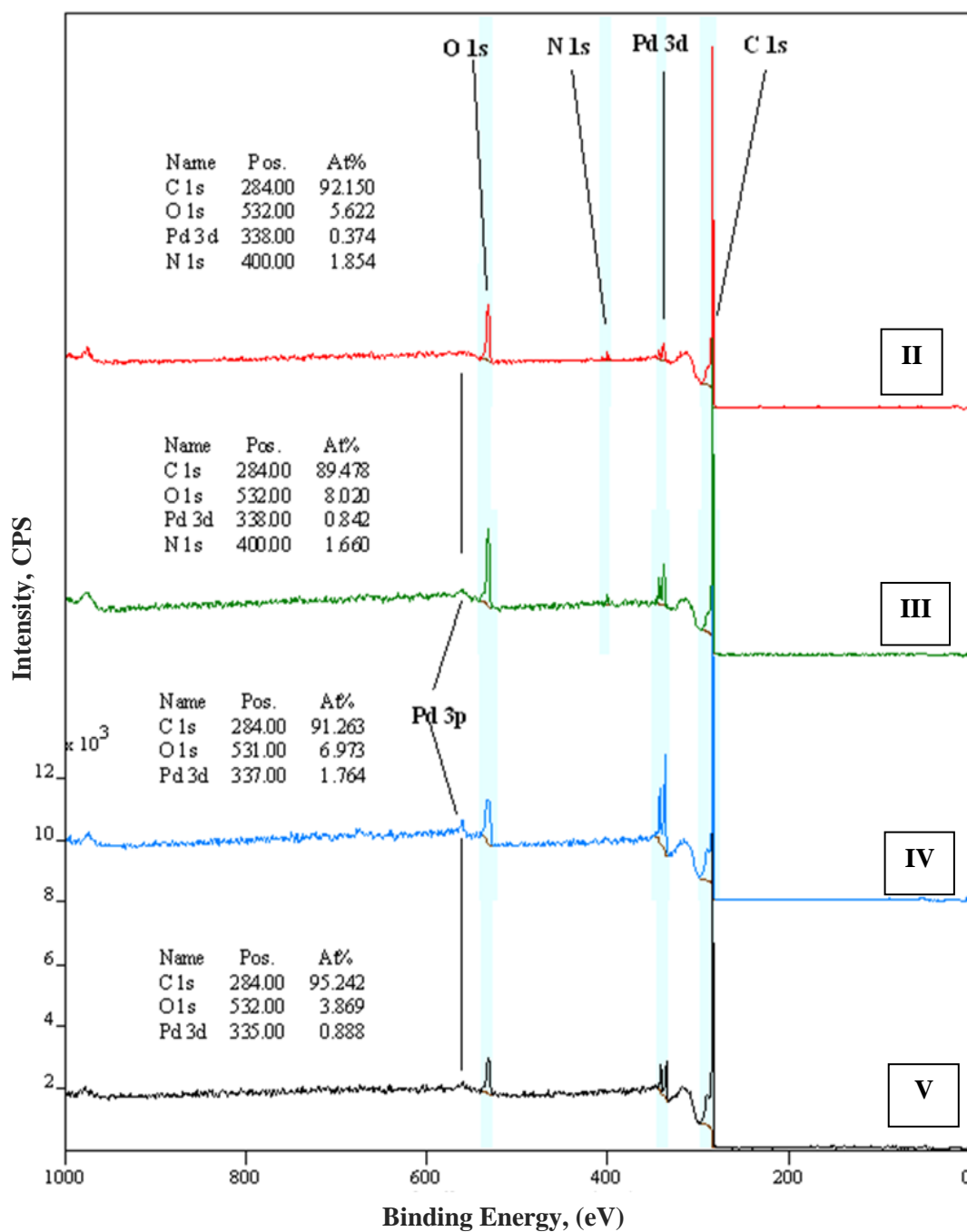


Figure 26 Survey-Scans of Samples II -V (Pd/HOPG)

**Sample: II – Control, III – Dried (De-hydrated),
IV – Calcined, and V – Reduced Samples**

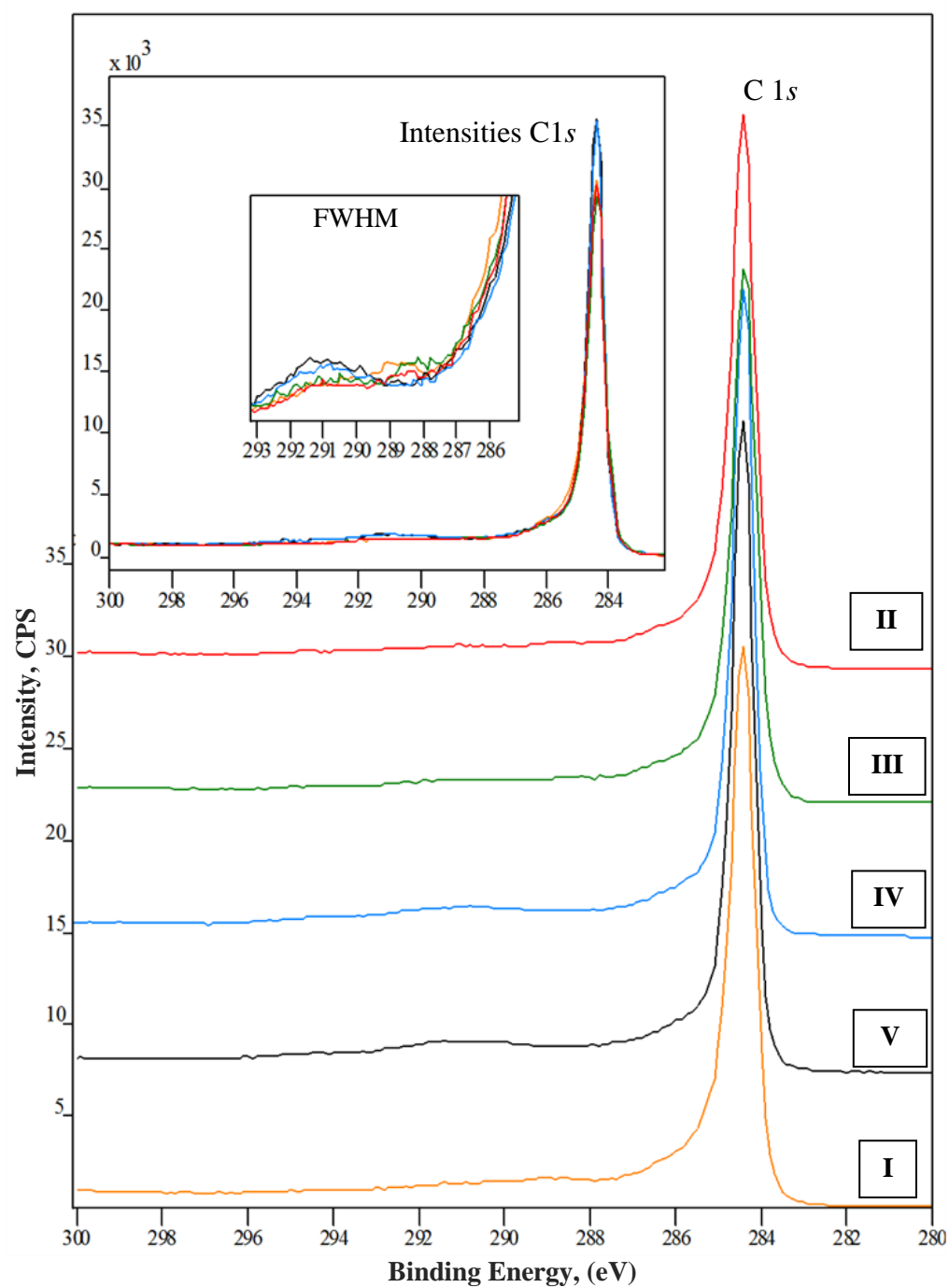


Figure 27 Fine-Scan Spectra of C1s for Samples I – V

**Sample: I – Pristine HOPG, II – Control, III – Dried,
IV – Calcined, and V – Reduced Pd/HOPG**

Palladium 3d Fine Scans

The high resolution spectra of the Pd 3d core levels obtained for samples II-V are shown in the Figures 28-32. Figure 28 shows the combined spectra of the Pd 3d (samples II-V). The Pd 3d_{5/2} peaks, labeled as P2, P3, P4, and P5 for sample II, III, IV, and V are at 338.2 eV, 338.07 eV, 337.09 eV, and 335.15 eV respectively (*P1 does not exist). The shift in the BE of Pd 3d peak (P2-P5), as shown in Figure 28, indicates the chemical shift of Pd. It relates to the transition of Pd from oxidized state (2+) to metallic state (0). The positions of peaks P2 and P3, obtained from sample-II (control) and sample III (dried), can be attributed to Pd(II) as assigned in [Pd(NH₃)₄]²⁺ complex [102,103]. The peak P4 at 337.09 eV, obtained from sample IV (calcined), has distinctively shifted by 1eV towards the lower binding energy, compared to the position of P3. The position of P4 at 337.09 eV is in good agreement with literature for the BE values of Pd-O (PdO, PdO₂, and PdO_x) at 336.5 eV-337.5 eV [104, 105]. The peak P5 at 335.15 eV represents the metallic state of palladium (Pd⁰) obtained for the reduced sample. The Pd 3d_{5/2} at 335.15 eV is in good agreement with the values of metallic Pd as published in the literature (334.9 – 335.5 eV) [104, 105].

Figure 29-32 shows the resolved peaks of P2 – P5, fitted with the components of different line shapes. The annotation in each image provides information of the line shape, position, doublet splitting, and FWHM of the component peaks. The component peaks of P2 and P3 are resolved using symmetric peak shapes as shown in Figure 29 and Figure 30. The XPS spectra for the peak P4 is resolved using symmetric peak shapes as shown in Figure 31. The sharp Pd 3d_{5/2} peak at 337.09 eV is followed by satellite peak at 339.6 eV. The satellite peaks represent the shake-up peaks of Pd-O as discussed in the literature and it contributes to less than 5% of the main peak [105]. For calcined sample

(sample IV), at the main peaks no shoulder peaks were observed that might indicate the presence of multiple binding states of an element. The sharp $3d$ peaks as seen in Figure 31 (which is not accompanied by shoulder peaks) represents the formation of bulk palladium oxide.

Figure 32 shows the resolved spectrum P5 of the reduced sample. It shows clearly that P5 has an asymmetric peak shape, a well known characteristic of the zero-state transition metals [106, 107]. Hence the peaks are fitted using the asymmetric peak model as shown in Figure 32. The doublet splitting of $3d_{3/2}$ and $3d_{5/2}$ peaks for metallic Pd (sample V) observed in this study was 5.27 eV. The BE values, FWHM, elements/compounds atomic percents and Pd $3d$ orbital splitting obtained for all the samples are tabulated in Table 3.

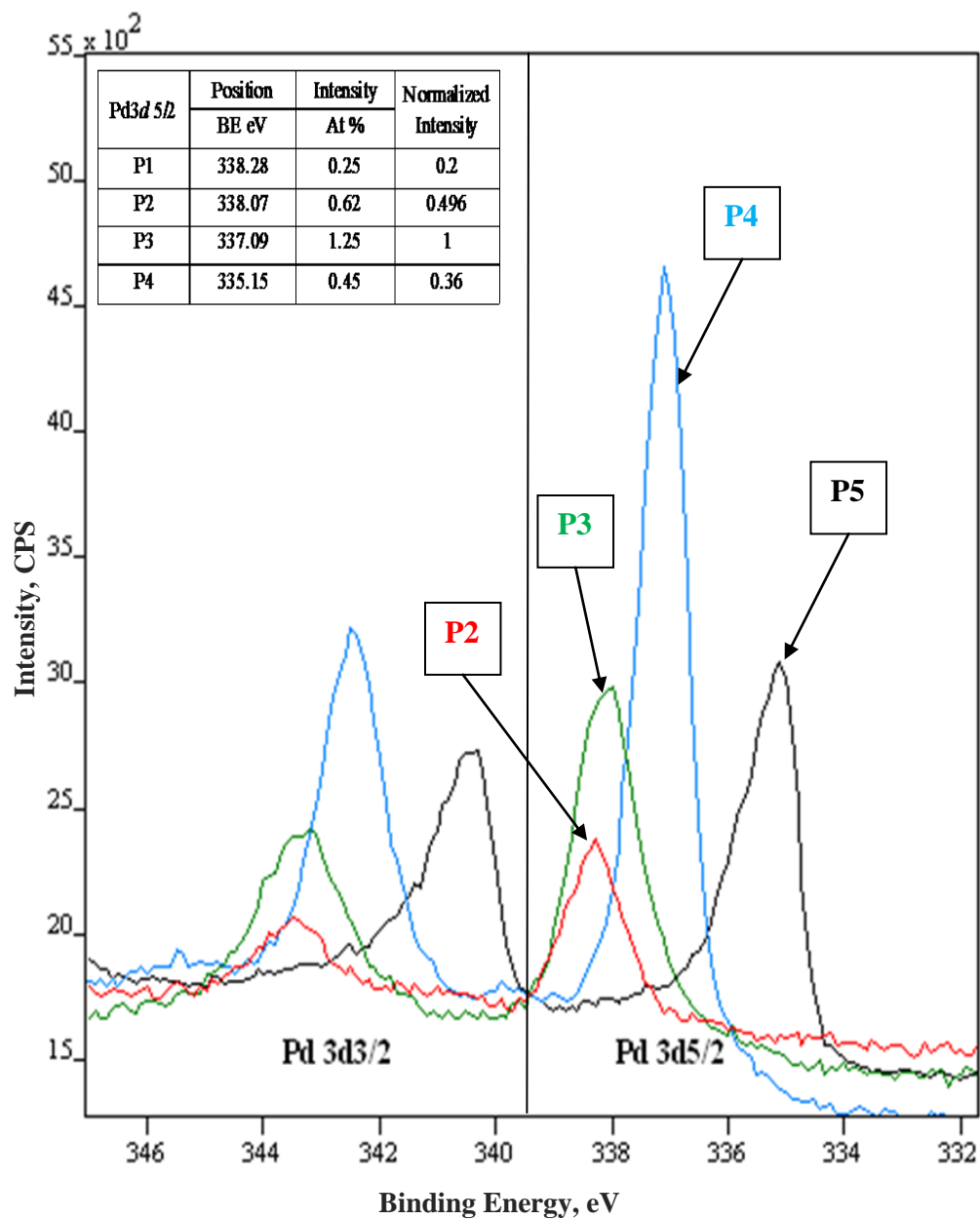
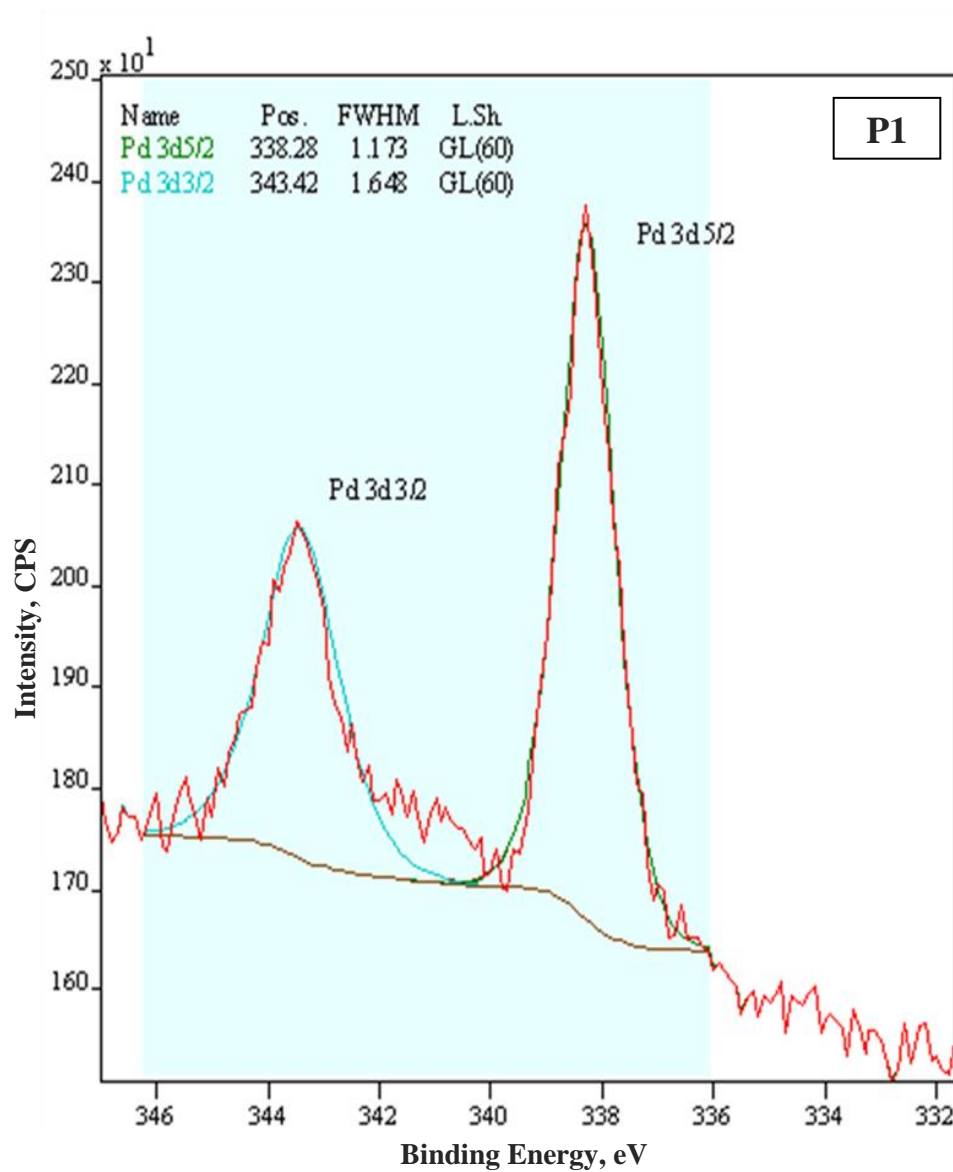
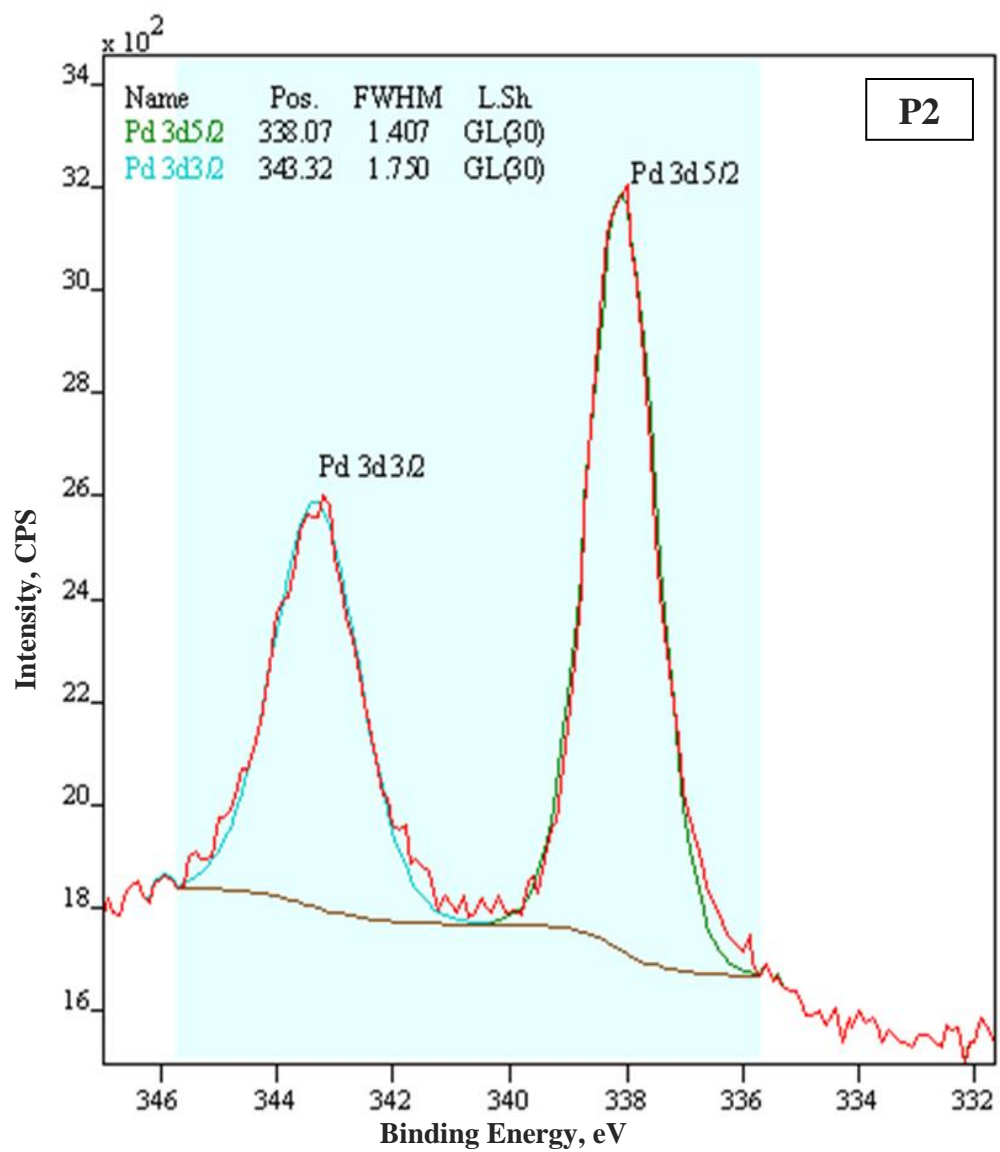


Figure 28 Comparative Fine-Scans of Pd 3d Core Level Spectra of Sample II - V

**II – Control (P2), III – Dried (P3),
IV – Calcined (P4), and V – Reduced (P5) Pd/HOPG**



**Figure 29 Resolved Fine-Scan of Pd 3d Spectra of Sample II
(Control Sample)**



**Figure 30 Resolved Fine-Scan of Pd 3d Spectra of Sample III
(Dried Sample)**

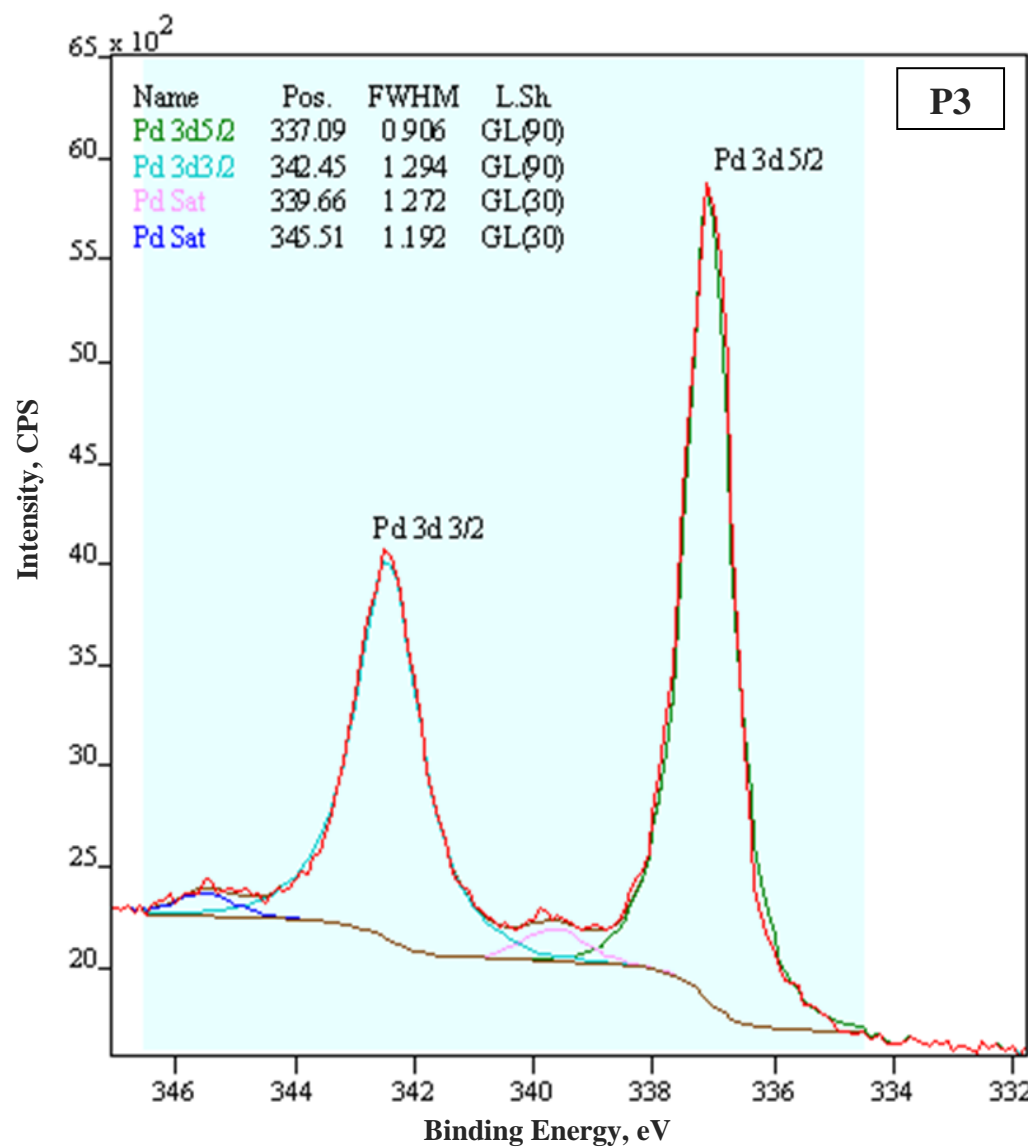


**Figure 31 Resolved Fine-Scan of Pd 3d Spectra of Sample IV
(Calcined Sample)**

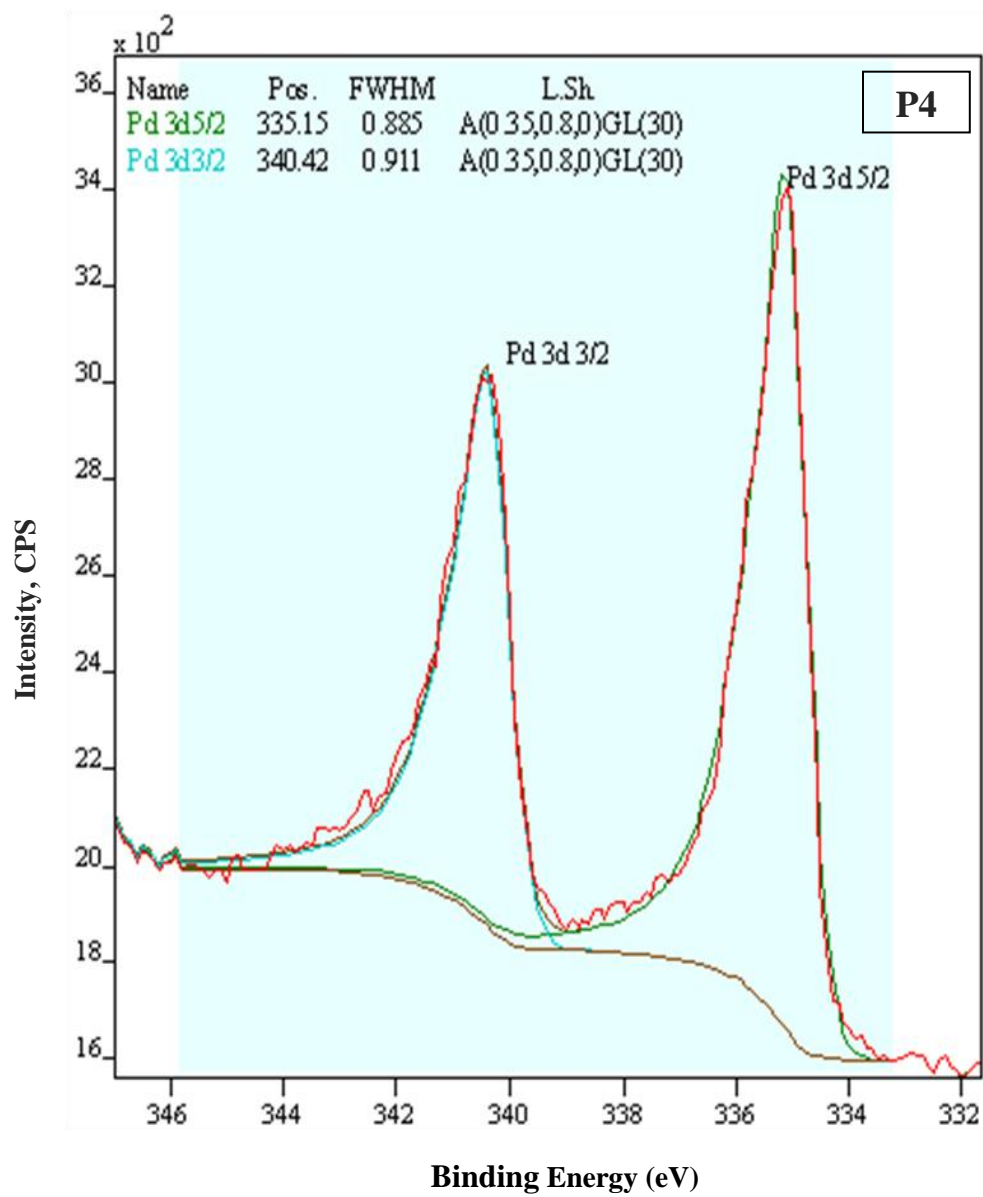


**Figure 32 Resolved Fine-Scan of Pd 3d Spectra of Sample V
(Reduced Sample)**

Oxygen 1s – Palladium 3p Fine Scans

It must be noted that the O 1s peak at 532 eV overlaps with the Pd 3p_{3/2} peak observed between 533.5- 534.5 eV. A high resolution scan, ranging from 575 - 525 eV was recorded for O 1s which includes the position range of Pd 3p_{1/2} peak and it is denoted as O 1s - Pd 3p peak. Figure 33-34 shows the O 1s-Pd 3p spectrum of the samples II-V, where the 3p_{1/2} peak is clearly separated part from O 1s peak unlike 3p_{3/2} peak. By using the intensity ratios of *p*-orbital splitting (3p_{1/2}:3p_{3/2} - 1:2) and suitable relative sensitivity factor (RSF), appropriate peak intensities were assigned to Pd 3p_{3/2} component to resolve the O 1s region. The possible component peaks related to different bonding types of O 1s in all the samples are designated as O1, O2, O3, and O4. The O 1s for sample II and III was resolved in two components of oxygen as shown in Figure 33. The component O1 in the 531.7 eV-531.8 eV region corresponds to the adsorbed oxygen species on the graphitic carbon as seen in pristine HOPG samples (Fig. 25D). The component O2 in the vicinity of 533.0 eV-533.1 eV can be attributed to the position of N-O bonding of the nitrate groups [108, 109]. Sample IV consists of Pd in oxidized form, where the Pd 3p_{3/2} at 534.3 eV is fairly separated from O 1s peaks and has relatively higher intensity (Figure 34A). The O 1s peak of sample IV has a new component O3 at 530.27 eV which can be attributed to Pd-O type oxide bonding [110]. The atomic percents of O 1s and Pd 3d are given in Table 3 that has an atomic ratio of 1:1.2 (~1:1) which closely relates to the stoichiometry for PdO. The O 1s peak for sample V is shown in Figure 34B. It is mainly O1 component corresponding to the adsorbed oxygen containing species on graphite as in HOPG. The sharp component peak of Pd-O bonding (O3) at 530.2 eV has disappeared, indicating the reduction of Pd oxide in sample V.

Nitrogen 1s Fine Scans

Figure 35 shows the XPS fine spectra of N 1s peak inclusive for all the samples (sample II-V). The N 1s peak of the sample II and III (control and dried samples) show three distinctive peaks whereas these peaks of the sample IV and V (calcined and reduced samples) have vanished completely. In sample IV and V, N 1s peak disappears as a consequence of heat treatment process that was carried out at temperatures above 400 °C (calcination and reduction steps). This temperature is well above the thermal decomposition temperature of tetraamine Pd(II) nitrate (220 °C). Hence at elevated temperatures complete decomposition of tetraamine and nitrate groups takes place and it often occurs as a function of both time and temperature. The removal of the nitrate and amine ligands from the sample leaves behind a contaminant-free metal surface (free from amine and nitrate ligands) as in this case.

Figure 36 shows the resolved N 1s peaks for both control and dried samples. The spectrum for control sample indicates two distinctive peaks (N1 and N2) at 399.9 eV and 406.3 eV, and a shoulder peak (N3) at 403.8 eV. These three distinctive N 1s peaks were also observed for dried samples within the range of ± 0.1 eV. The peak at 399.9 eV (400 eV) is widely assigned to -NH- (amine groups) and the peak at 406.3 eV is commonly assigned to -NO- (nitrate groups) [111, 112]. The observed intensity ratios of NH : NO are larger than the theoretical ratios of tetraamine palladium nitrate, indicating transfer of some ligands due to the support interactions, drying, or UHV conditions. The shoulder peak at 403.8 eV has not been discussed in the literature. It is suspected to be a peak related to -N-M- bonding (M-metal) according to the structure of TAPN as discussed by et al [113].

In an effort to solve N 1s peak, the as-is TAPN solution (375 mM TAPN) was chosen for XPS analysis and it was allowed to air dry for 12 hours on a glass cover slide. After drying, TAPN was transferred onto the carbon tape attached to XPS stub. This sample was held in vacuum ($\sim 10^{-7}$ Torr) for 3 hours prior to collecting the spectrums. The sample ID is chosen as Control#2. Figure 37 shows the N 1s spectrum of concentrated TAPN, corrected for charging +1.5 eV as measured from C 1s peak. (low signal C 1s was observed). One would notice strong signal of nitrogen which is due to high concentration of TAPN. After correction of charge, the distinctive main peaks (N1 and N2) of N 1s spectrum were observed at 399.65 eV and 406.43 eV. These positions correspond to –NH– and –NO– groups respectively [111, 112]. However, the peak at 399.65 eV was accompanied with a satellite peak (N4) at 401.57 eV that was not observed previously. The amine group peaks are sometimes accompanied by shakeup peaks as seen in literature. It is due to the protonation of amine groups under the influence of x-rays or UHV, although it is beyond my knowledge to explain the presence of this peak completely [114]. A shoulder peak (N3) at 403.63 eV was also observed as seen in previous samples and it is too big for a shake-up of nitrates. Although a conclusion could not be made for this peak, but it can be attributed to a bonding type in TAPN salt that suggests nitrogen ligands bonded to metal species [113], or it could be related to NO_x type of bonding [108, 109]. The obtained intensity ratio of the amine and nitrate peaks suggests that the precursor salt have experienced changes (ligand transfer) while drying or while in UHV conditions. Further resolving the N 1s component peaks intensity ratio (Table 3) is beyond my understanding.

It is noteworthy to mention that the intensity of P4 is higher than P3 and P2 (Figure 28 and Table 3). In calcination step at elevated temperatures, the nitrates and

amine ligands decompose into respective gases, leaving behind exposed palladium surfaces. The Pd readily oxidizes in the favorable oxygen-rich air environment at elevated temperatures forming PdO. It should also be pointed out that the intensity of P5 has significantly reduced compared to that of P4, which was otherwise expected to increase with removal of oxygen from palladium. Dwelling into the details of this problem is beyond the scope of this thesis and efforts will be made in the future to resolve this finding.

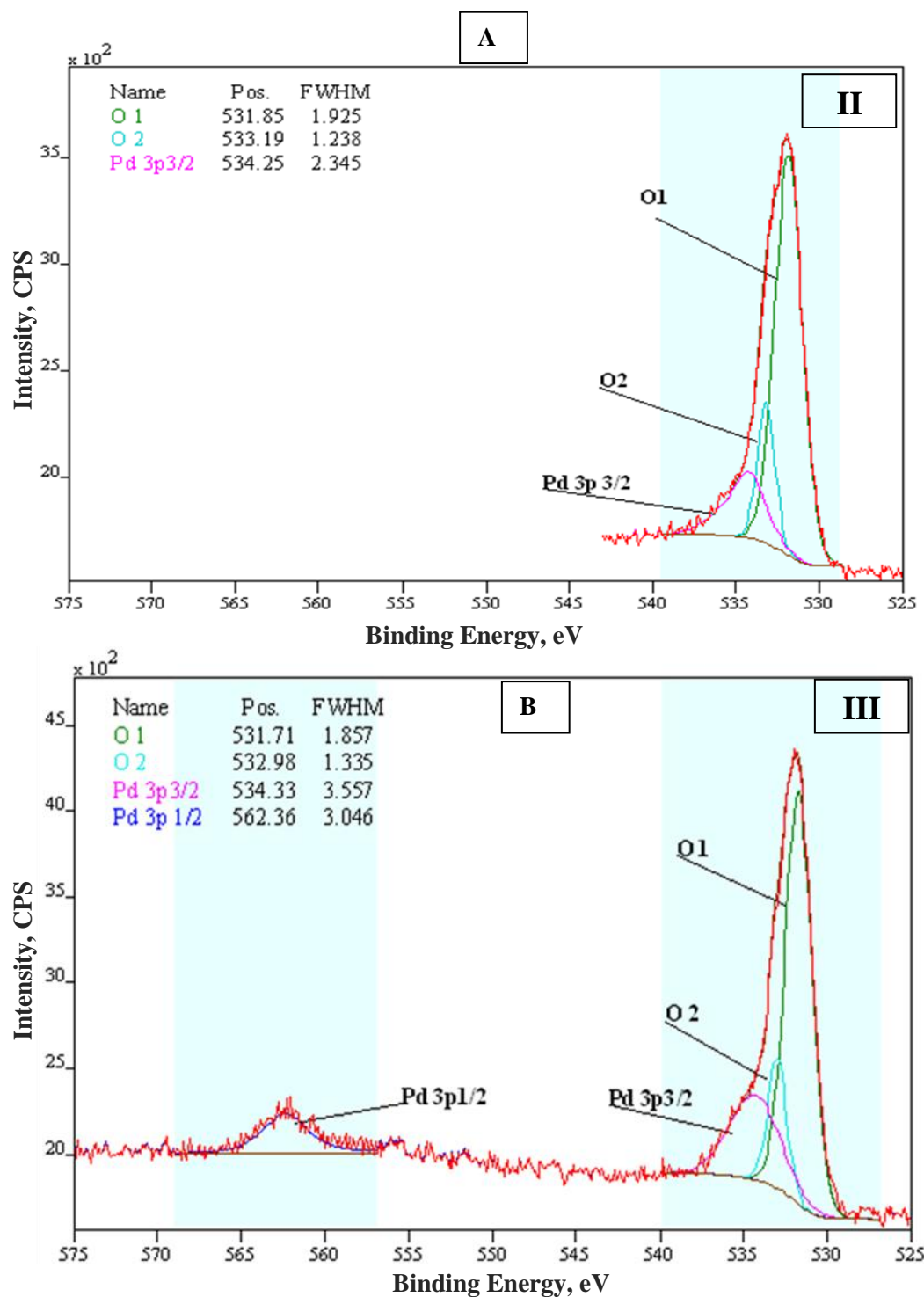


Figure 33 Fine-Scan Spectrums of O 1s and Pd 3p of Samples II and III

(A) Sample II (Control Sample), and (B) Sample III (Dried Sample)

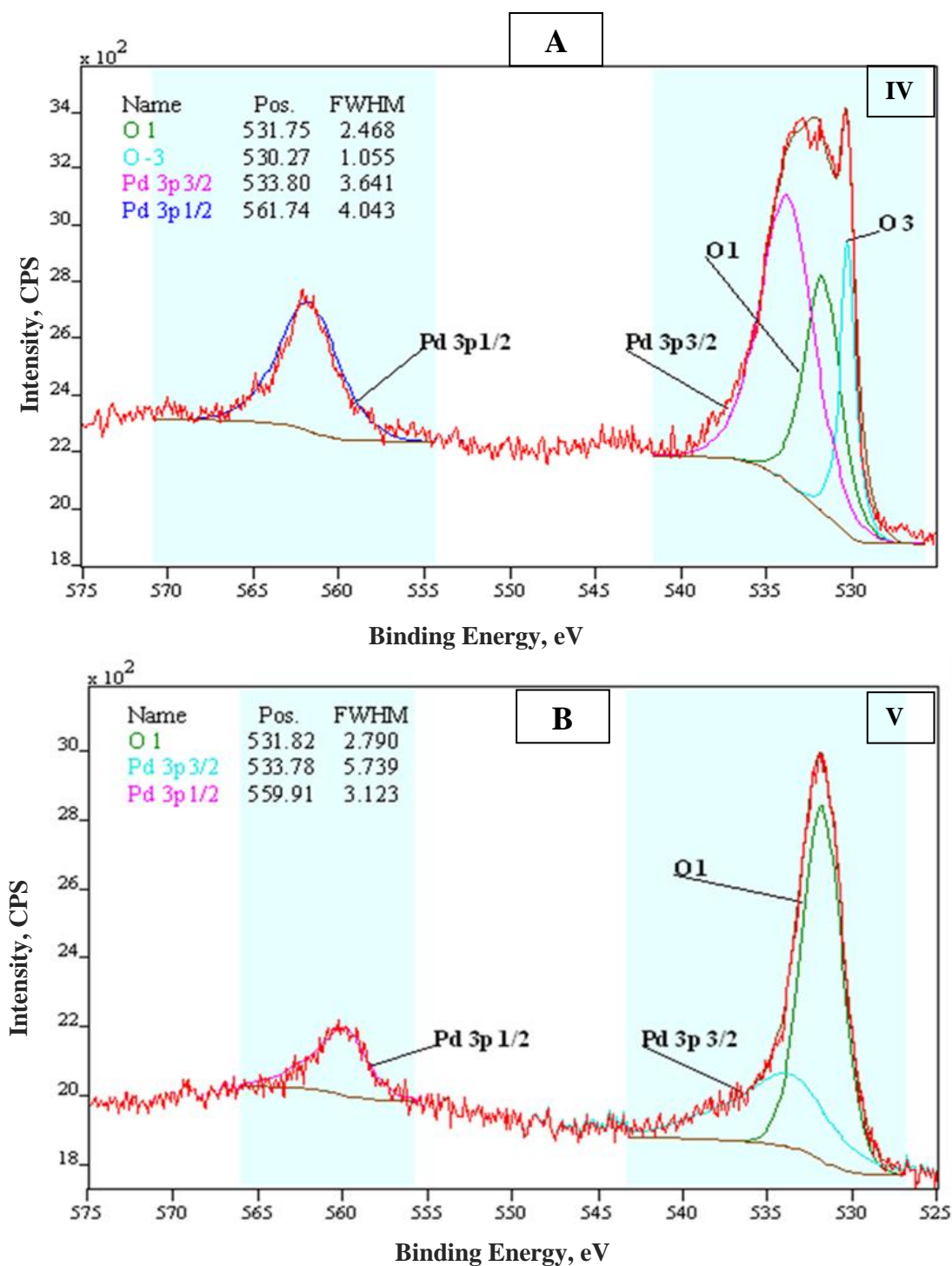


Figure 34 Fine-Scan Spectrums of O 1s and Pd 3p of Samples IV and V
(A) Sample IV (Calcined Sample), and (B) Sample V (Reduced Sample)

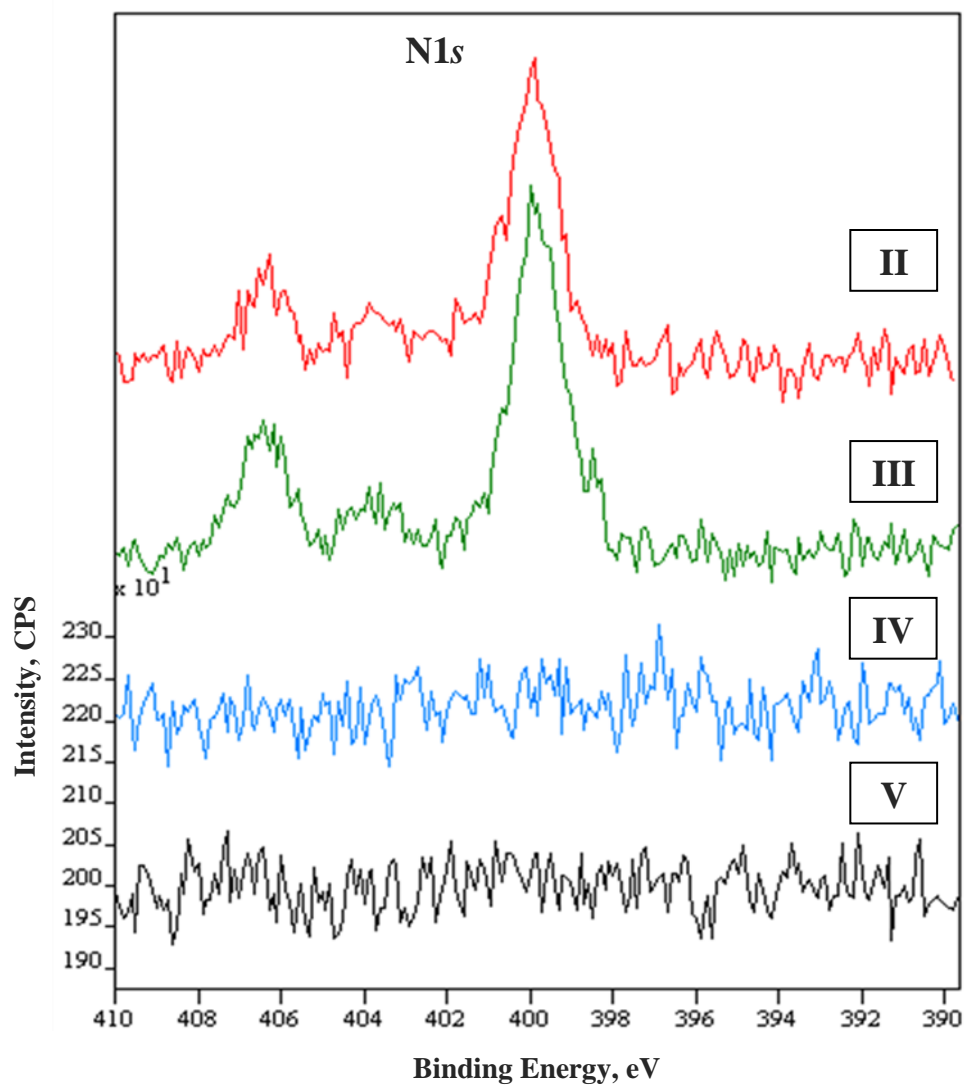


Figure 35 Fine-Scan Spectrums of N 1s for Samples II – V

**Sample: II – Control, III – Dried,
IV – Calcined, and V – Reduced Samples**

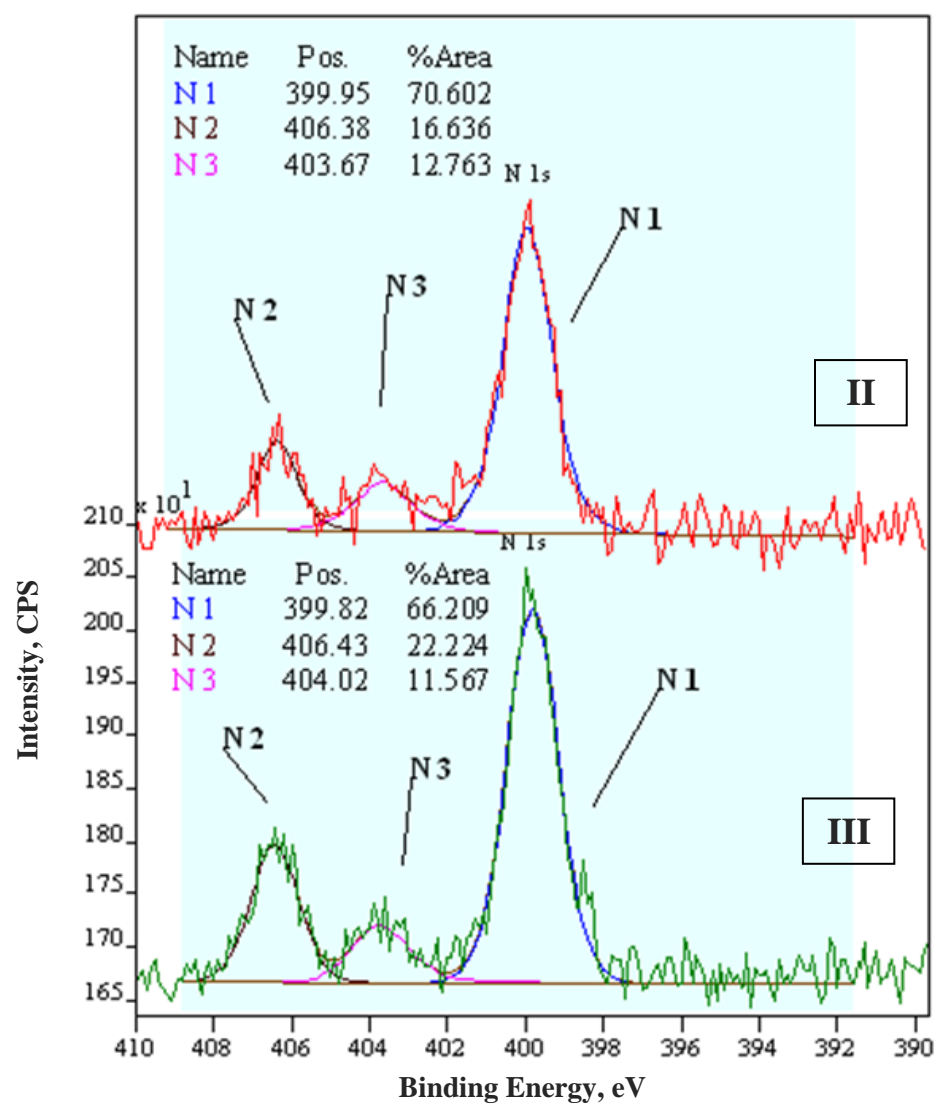


Figure 36 Fine-Scan Spectrums of N 1s for Samples II and III

Sample: II – Control and III – Dried Samples

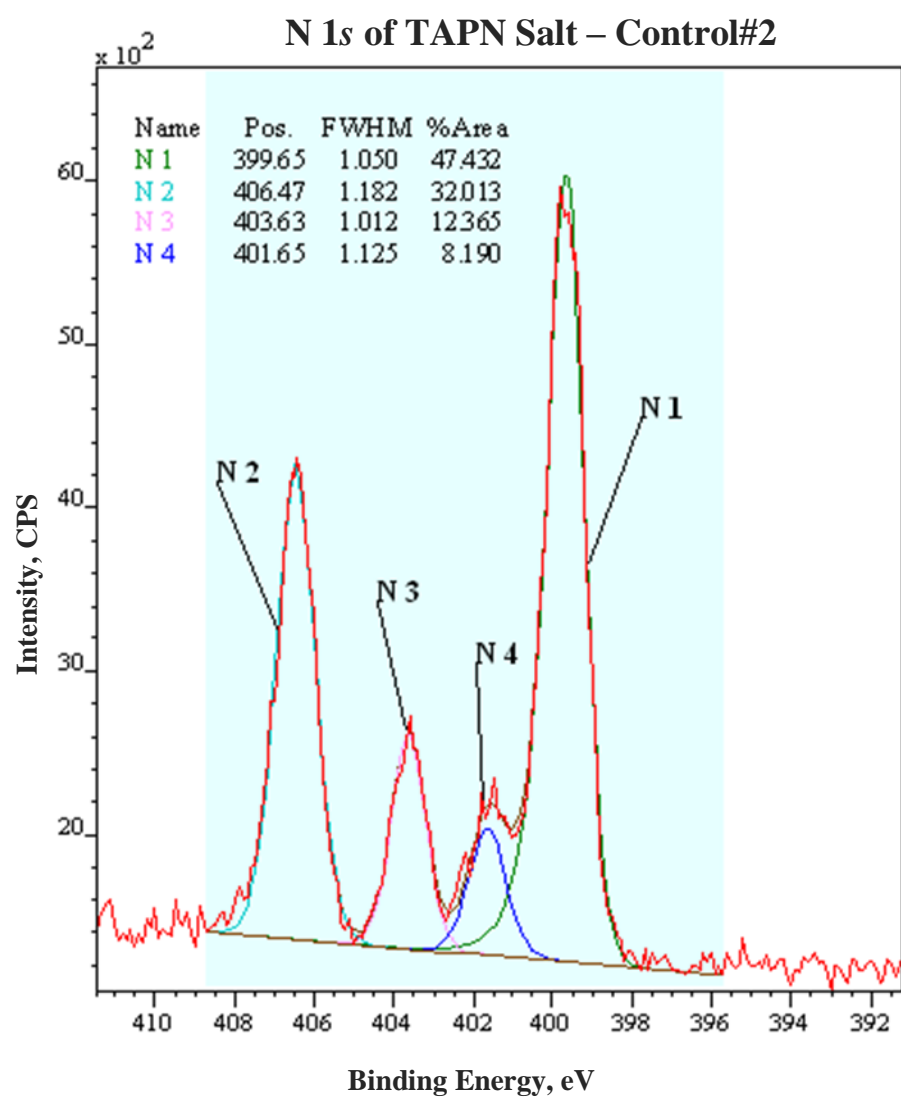


Figure 37 Fine-Scan of N 1s Spectra of Control #2

Table 3 Elemental Ratios Obtained from XPS for Samples at Intermediate Steps

Sample ID→ BE, eV (FWHM, eV) At % ↘	Pristine I	Control II	Dried III	Calcined IV	Reduced V	*Control #2
↓ Core Peaks						
C 1s (C1a)	284.4 (0.59)	284.4 (0.5)	284.4 (0.58)	284.4 (0.52)	284.4, (0.51)	284.39, (1.16) (*282.89 +1.5)
	94.59	94.7	93.13	95.84	97.07	12.87
Pd 3d _{5/2} (**Doublet Splitting, ±0.02eV)	-----	338.28 (1.17) **5.14	338.07 (1.4) **5.25	337.09 (0.9) **5.36	335.15 (0.88) **5.27	338.24 (0.95) **5.21
	-----	0.25	0.62	1.25	0.45	6.66
O1s (O1)	532.3 (2.5)	531.8 (1.92)	531.7, (1.85)	531.7 (2.46)	531.8 (2.79)	---
	5.4	3.287	4.04	1.827	2.48	---
O1s (O2)	-----	533.19 (1.24)	532.98 (1.3)	-----	-----	531.94 (1.39)
	-----	0.74	0.91	-----	-----	40.98 [#]
O1s (O3)	-----	-----	-----	530.27 (1.05)	-----	O4 - 538.9
	-----	-----	-----	1.08	-----	2.73
N1s (N1)	-----	399.95 (1.46)	399.82 (1.55)	-----	-----	399.65 (1.05)
	-----	0.69	0.85	-----	-----	17.4
N1s (N2)	-----	406.38 (1.18)	406.43 (1.43)	-----	-----	406.47 (1.18)
	-----	0.164	0.288	-----	-----	11.7
N1s (N3)	-----	403.67 (1.64)	404.02 (1.63)	-----	-----	403.63 (1.01)
	-----	0.12	0.15	-----	-----	4.5
N1s (N4)	-----	-----	-----	-----	-----	401.65 (1.12)
	-----	-----	-----	-----	-----	3.0

* Corrected BE values to C 1s 284.4eV by 1.5eV

** 3d orbital splitting values

O4- new peak was observed

[#] may include oxygen bonds related to carbon peak

Table 4 Elemental Ratios from XPS and EDAX

	XPS ANALYSIS		EDAX ANALYSIS	
	At%	Wt%	At%	Wt%
Pd/HOPG				
C 1s	98.87	97.3	96.99	94.28
O 1s	0.97	1.27	2.76	3.57
Pd 3d	0.16	1.39	0.25	2.15
Pd/CNT/HOPG				
C 1s	92.69	80.44	83.67	64.07
O 1s	4.65	5.38	10.05	10.25
Si 2p	0.75	1.52	1.57	2.82
Fe 2p	0.55	2.23	2.82	10.04
Pd 3d	1.36	10.44	1.89	12.82

6.3.7. Qualitative Analysis of Pd-NPs on Bare HOPG and CNT-Grafted HOPG

For this study Pd-NPs were fabricated on the two types of supports, (i) untreated bare graphite (Pd/HOPG) and (ii) CNT-grafted graphite (Pd/CNT/HOPG) by single coating Pd process using identical conditions. SEM micrographs followed by EDAX scans for the Pd/HOPG and Pd/CNT/HOPG samples (Fig. 38). The XPS Pd 3*d* fine-scans of the above mentioned two samples are shown in Figure 39. To obtain the chemical state of palladium the fine scans of Pd 3*d* peaks were analyzed. The binding energy positions for Pd 3*d*_{5/2} for Pd/Foam and Pd/CNT/Foam are at 335.3 eV and 340.6 eV respectively. The 3*d* orbital splitting is 5.3 eV for Pd/Foam and Pd/CNT/Foam. The XPS signal clearly shows that the Pd formed by this process is completely reduced to its zero oxidation state. The energy values correlates well with the literature for the positions of metallic Pd and it is within the threshold limits for the BE values obtained for reduced sample as discussed in the previous sections [106, 107]. The SEM images show that, CNT/HOPG support accommodates more number of Pd particles compared to bare HOPG support. The EDAX and XPS analysis confirms the analogous results as shown in Table 4. The iron signal in CNT coated samples is from remnant iron nanoparticles formed during CNT growth, but they do not interfere with the Pd in any way.

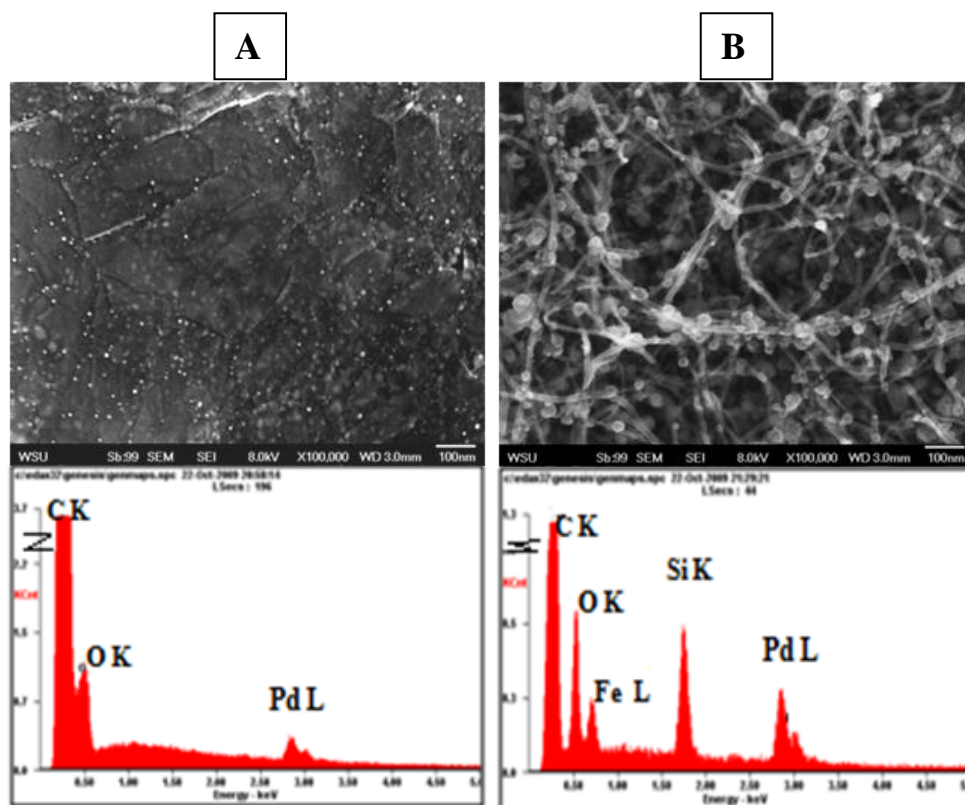


Figure 38 SEM Micrographs and EDAX Scans of (A) Pd/HOPG and (B) Pd/CNT/HOPG

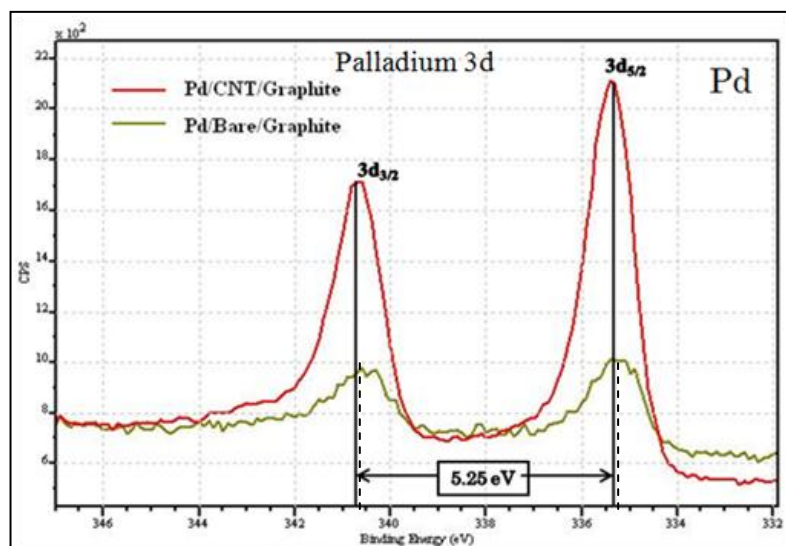


Figure 39 XPS Spectra Pd 3d Fine-Scans of (A) Pd/HOPG and (B) Pd/CNT/HOPG

7. RESULTS AND DISCUSSIONS: Bench-Scale Dechlorination of Carbon Tetrachloride Using Palladium Catalyst

7.1. Reductive Dechlorination Test: Objective

The research carried out in this study focuses on the catalytic activity of palladium nanoparticles (Pd-NPs) loaded on hierarchical, porous, and robust carbon structures. This research is part of this thesis that includes synthesis, characterization, and evaluation of the Pd-NPs supported on new class of carbon nanomaterials as catalysts, to the real world applications in a way which is sustainable for economical and ecological efficiency.

The present study focuses on the bench scale investigation of catalytic reductive dechlorination of carbon tetrachloride (CT) in the aqueous phase using different as-synthesized carbon supported Pd-NPs as catalysts. The results of this study include the following: (1) batch experiments characterized how different carbon supports for Pd-NPs affect the CT transformation, (2) studied the chemical and the physical state of Pd-NPs attached on both carbon foam and carbon nanotubes (CNT) grafted foam supports, before and after catalyst testing using XPS, SEM, and EDAX techniques. The study also focused on the effects of varying support sizes on the kinetics of CT degradation and the formation of daughter products.

7.2. Background

Halogenated hydrocarbons are the common organic contaminants that are present in soil and groundwater across the globe. These organic solvents are persistent in the environment as they have been widely used in fire extinguishers, dry cleaning, metal

processing and degreasing, electronics, paints, refrigerants and many more industrial applications [115]. Unaware of their toxic effects, these products intentionally or accidentally were released into the environments in recent decades. Contamination of ground water by chlorinated organic compounds (COC) such as chlorinated alkanes, alkenes, aromatics and chloro-flouro hydrocarbons (CFCs) is of great concern worldwide, due to their adverse effects on water quality and human health. Among which, tetrachloroethylene (PCE), carbon tetrachloride (CT), and trichloroethylene (TCE) are a few COC that are present quite frequently in the environment. Exposure to such chemicals through drinking water even at very low levels is considered to be highly toxic and hazardous to health. Owing to their ability to volatize, some of halogenated hydrocarbons also play a major role in the depletion of the atmospheric ozone layer [116]. As such, use of these chemicals was either banned or reduced in United States by US-EPA regulations, Montreal Protocol (1996) and colloquially in most other developed countries [116,117].

7.2.1. Carbon Tetrachloride

Carbon tetrachloride (CT), also known as tetra-chloromethane or perchloromethane is among the widespread COC in the ground water. There are a number of reasons for its existence; the major reason is due to its widespread use in industrial and chemical applications. CT was first synthesized, in 1839, by chemical reaction of chlorine with chloroform (CF). It can also be prepared by chlorination of various other compounds like methane, higher hydrocarbons, or carbon disulfide. Prior to regulations, CT was largely used in fire extinguishers, as cleaning and metal degreasing agents, and also as a precursor compound for refrigerants like CFCs [115]. Carbon tetrachloride can

have adverse affects on the nervous system, liver, and kidneys. The US EPA has recognized it as a potential carcinogenic agent (US EPA 1987) and has determined a maximum contaminant level (MCL) of 5 µg/L (US EPA 1998) [118-121]. Due to its chronic toxicity and greenhouse effects, its production and consumption has rapidly declined since 1980's. However, it is still present at hazardous levels at many locations in soil, ground water and atmosphere [121].

7.2.2. Common Contaminant Elimination Techniques

After release, CT can persist in the environment due its resistance to degradation. Many treatment technologies have been developed to remove CT and similar chemicals from the environment and to improve groundwater resources. Some conventional techniques in use for removal of chlorine solvents from the contaminated aquifers include pump and treat, combustion, and osmosis [122]. In pump and treat, the water is pumped above the ground surface and treated. This method requires installation of heavy equipment at the contaminated sites. However, it has limited capability of removing contaminants and once pumping is stopped the dissolved contaminants tend to rebound into the groundwater. The process of pollutant destruction by combustion or incineration also has other polluting effects. The above technologies are less effective and are not contaminant specific, which calls for proper disposing practices that would only increase the cost of the system [122-124].

7.2.3. Catalytic Reduction or Dehalogenation

Over the last two decades, researchers have investigated various effective and environment friendly methods to remove chlorinated organic solvents from the water resources. A common technique is catalytic reduction of chlorinated compounds using

transition metals as catalysts. Transition metals are known for catalyzing wide variety of organic reactions that include reduction, oxidation, hydrogenolysis, hydrogenation, and dehydrogenation. Catalytic reduction of chlorinated solvents has been studied by various following processes like electrochemical dechlorination, reductive dechlorination, radiation dechlorination, and hydro-dechlorination processes [125]. The removal of COC by catalytic dechlorination is advantageous as it yields in selective reduction of the toxic chlorinated compounds to non-toxic or less toxic daughter products. The dechlorination reactions are catalyzed in presence of mono- or multi-metallic systems consisting of noble metals or zero-valent metals (ZVM). Zero valent iron (ZVI) is amongst the most cited metal for dechlorination of COC [126], as a reductant (electron donor). However, ZVI shows slow reduction, and it is susceptible to corrosion and gradual passivation; hence ZVI is often coupled with other noble metals to enhance its catalytic performance [127-129]. The common metals used for catalytic dechlorination of COC include platinum, palladium, rhodium, zinc, silver, gold, copper, etc.; amongst these metals, Pd is a well known catalyst for selective reduction of chlorinated carbon species. Gomez-Sainero et al. [130] investigated the kinetics of dechlorination and hydrogenation of carbon tetrachloride using various noble metals; they reported that Pd metal has greater affinity to break the carbon chlorine bonds with high selectivity and also has high chemical resistance to deactivation [130]. Pd coupled with ZVM can form an excellent bimetallic system for catalytic dechlorination. Pd/Fe bimetallic systems are more commonly investigated for dechlorination reactions [128, 131]. Bimetallic systems are effective and challenging. However, these systems are complex systems that are not understood quite well and are still being explored.

The treatment of chlorinated organic compounds in aqueous phase at ambient temperatures is an ideal condition resembling practical applications and hence has gained attention of the researchers over the years. In this study, we use mono-metallic Pd-NPs attached to carbon supports for aqueous phase catalytic dechlorination of CT. Palladium stands as a promising catalyst for reductive dechlorination of wide variety of toxic compounds at ambient temperatures such as; halogenated alkanes, alkenes, aromatics and halo-aromatics compounds like polychlorinated biphenyls (PCB), and also nitrate and nitrite compounds [132].

Nanoparticles adhered on to supports are commonly denoted by metal/support, e.g. Pd/C. The supports not only provide the underlying structure and avoid the agglomeration of the nanoparticles, but also influence the catalytic activity by specific metal-support interactions. Selection of support material plays an important role in the catalytic activity due to its interactions with the metal [20-21]. Gomez-Sainero et al. [130] have shown that the reactivity of Pd towards dechlorination may vary with support material and showed that Pd/C has higher activity and greater selectivity towards dechlorination of CT [130]. Most commonly used carbon materials like carbon nanotubes (CNTs) are advantageous as they possess extremely high specific surface area, which makes them attractive as catalyst supports, and they can also be effective as pollutant adsorbents in water treatment applications. The application of metal nanoparticles in water treatment technologies may impose certain challenges such as recovery of nanoparticles from water, their reusability and toxicity. If the nanoparticles to be utilized in water treatment applications are in suspended form, the recovery of the catalyst from the treated water and its reusability can be difficult. Nanoparticles, if not recovered from

the treated water, may pose toxicity to the receptors, and the treatment process can also become cost-prohibitive.

We present a new class of hybrid supports for anchoring Pd nanoparticles, CNT-grafted on microcellular carbon foam. It is the combination of the high surface area provided by the CNT and the structural robustness endowed by the micro-cellular carbon foam in designing flexibility, high catalytic activity and effective reusability of metal catalysts. These supports offer a convenient and environmental friendly approach unlike the free-standing particles.

7.3. Supports Used in this Study

Palladium nanoparticles supported on carbon foam and CNT-grafted foam samples were used in this study. Pd on both the supports was fabricated by the similar process as discussed in the earlier part of this thesis (precursor equilibrium-adsorption and thermal reduction). But here, both the supports were calcined in inert Ar environment. Figure 40 shows the typical SEM micrographs of Pd/Foam and Pd/CNT/Foam supports. The supports used in this study were 10x5x2 mm³ in dimensions, each weighing approximately 55 mg prior to palladium loading. The samples after palladium loading did not show significant increase or decrease in weight (up to four decimals of a gram – 100 µg). Table 5 provides statistical data for the surface area and mass of the Pd loaded on the above mentioned supports.

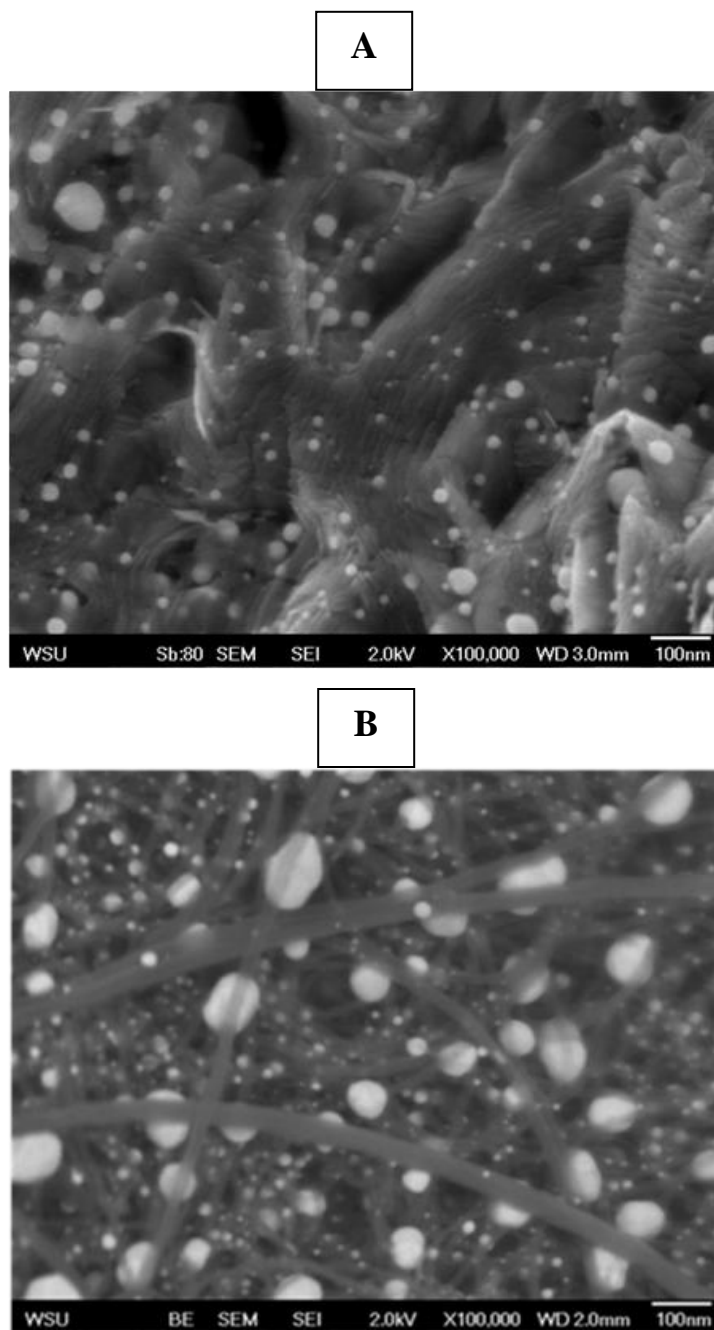


Figure 40 SEM Micrographs of Supported Pd-NPs Used for CT Dechlorination Test
(A) Carbon Foam Support (Pd/Foam) and (B) CNT-Grafted Foam Support (Pd/CNT/Foam)

Table 5 Estimated Mass of Palladium Loaded on Foam and CNT/Foam Supports

Approximate Mass of Palladium loaded on the Samples –Calculations				
S.No	Description	Formula	Amount	
1	Specific Surface Area of Foam	A ^[29]	6.2x10 ³	m ² /m ³
2	Size of the Support	B	100 (10x5x2)	mm ³
			100 x 10 ⁻⁹	m ³
3	Weight of the Support	C	55	Mg
4	Surface Area of the Support	S _A = A x B	6.2 x 10 ⁻⁴	m ²
			6.2 x 10 ⁸	μm ²
5	Density of Palladium,	ρ	12.02	g/cm ³
			12.02 x 10 ⁻⁶	μg/μm ³
Pd/Foam – Untreated Foam size 10x5x2 mm ³ (55mg)				
6	Surface Area of Pd-NPs on Untreated Foam per μm ²	*S _{Pd/Foam}	13 x 10 ⁻³	μm ²
7	Surface Area of Pd-NPs on Untreated Foam in 6.2 x 10 ⁸ μm ² (100mm ³)	S _{Pd/Foam} x S _A	8.06 x 10 ⁶	μm ²
8	Volume of Pd-NPs on Untreated Foam per μm ²	*V _{Pd/Foam}	10 x 10 ⁻⁶	μm ³
10	Volume of Pd-NPs on Untreated Foam in 6.2 x 10 ⁸ μm ² (100mm ³)	V _{Pd/Foam} x S _A	6.2 x 10 ³	μm ³
11	Total Estimated Mass of Pd on Foam in 100 mm ³ (in 55mg)	M _{Pd} = ρ x V _{Pd/Foam} x S _A	0.0745	μg
Pd/CNT/Foam – CNT-Grafted Foam size 10x5x2 mm ³ (55mg)				
12	Surface Area of Pd-NPs on CNT/Foam per μm ²	*S _{Pd/CNT/Foam}	150	μm ²
13	Surface Area of Pd-NPs on CNT/Foam in 6.2 x 10 ⁸ μm ² (100mm ³)	S _{Pd/CNT/Foam} x S _A	93 x 10 ⁹	μm ²
14	Volume of Pd-NPs on CNT/Foam per μm ²	*V _{Pd/CNT/Foam}	842 x10 ⁻³	μm ³
15	Volume of Pd-NPs on CNT/Foam in 6.2 x 10 ⁸ μm ² (100mm ³)	V _{Pd/CNT/Foam} x S _A	522 x 10 ⁶	μm ³
16	Total Estimated Mass of Pd on 100% coverage CNT/Foam in 100 mm ³ (in 55mg)	M _{Pd} = ρ x V _{Pd/CNT/Foam} x S _A	6274	μg
17	Total Estimated Mass of Pd on 20% coverage CNT/Foam in 100 mm ³ (in 55mg) (Reference 27)	0.2 x M _{Pd}	1255	μg

7.4. Gas Chromatograph

Gas chromatography is a technique that can quantify the volatile compounds present in gaseous sample. A gas chromatograph consists of a flowing mobile phase, an injection port, a column also known as a separator that is placed in a temperature controlled oven, a detector, and a data recording system. The mobile phase is the carrier gas that could be any inert gas. The column consists of a stationary phase which is either a solid or a liquid coated on the solid. The gaseous sample to be analyzed is injected into the preheated injection port using a gas tight syringe where they are carried into the column by the carrier gas. Compounds of the mixture that are carried by the mobile gas phase interact with the stationary column phase differently depending on their physical properties and pass through the column at different rates. This differential partitioning behavior allows the compounds to be separated in time and space. The fastest moving compound exits from the column into the detector first followed by remaining ones. Hence, each component reaches the detector at a different time and it generates a signal at the particular characteristic time known as retention time of the compound. The size of the peak determines the amount of the particular compound present in the gas mixture. The retention time for a particular compound is sensitive to the column conditions. A compound in gas phase should not decompose at the operating temperatures for GC analysis.

To be suitable for GC analysis, the compounds present in the liquid phase must possess volatilizing ability and thermal stability. Carbon tetrachloride and its daughter products have volatilizing ability required for GC analysis. The volatilizing factor can be calculated using ideal conditions of gas laws and Henry's gas constant. GC 7890 (Agilent technologies Inc.) was used in this study.

7.5. Materials and Methods

7.5.1. Chemicals

The reagents used in this research were of analytical grade and used without further purification including carbon tetrachloride (CCl_4 , Fisher Scientific), chloroform (CHCl_3 , Fisher Scientific), sodium hydroxide (solid, 97.0% NaOH, EMD Chemicals Inc.), TAPSO buffer (99%, $\text{C}_7\text{H}_{17}\text{NO}_7\text{S}$, Sigma-Aldrich Inc.), and double sided carbon tape. The water used in this study was MiliQ DI water ($0.22\ \mu\text{m}$). Gases used in this study were of high purity that includes 5% H_2 balance N_2 , 49.99% H_2 balance N_2 , and pure nitrogen gas was obtained from liquid nitrogen. Gas-tight syringes (Hamilton, Inc.) and end-to-end rotators at 32 rpm (Glas-Col®) were used. The pH of buffer solution was monitored using a pH meter (AP10, Denver Instruments).

7.5.2. CT - Stock Solutions and Standards

The stock solution of CT (200 mg/L) was prepared in 160 mL glass serum bottle. The serum bottles filled with DI water were capped with Teflon-lined butyl rubber stoppers and sealed with aluminum crimp leaving no headspace. Now 20 μL of free-phase carbon tetrachloride (neat) was injected into the serum bottle. The serum bottles containing stock solution were placed on a rotary shaker and allowed to equilibrate for a minimum of 48 hours prior to use.

CT standards (gaseous analytical standards) were prepared in 160 mL serum bottles by adding 96 mL DI water leaving 64 mL of air headspace volume, so as to maintain the water to headspace ratio of 60:40. The bottles were capped with stoppers and sealed with Al-crimps. Measured amount of stock solution was injected to the sealed serum bottles using appropriate volume of micro-syringes. Gas samples of volume 50 μL

was derived from the headspace of the each reactor using gas-tight syringe and analyzed on GC-MS 7890. The known concentration of CT in both liquid and gaseous phase was calculated using ideal gas law equation and Henry's constant for evaporation constant of CT. The stock solutions and standards for the expected daughter products were also obtained similarly. Table C1 – C4 in Appendix C show the standard calculations and the measured values for CT and CF.

7.5.3. Batch Experiments Methods

The dechlorination of carbon tetrachloride was carried out in a batch reactor system of 160 mL glass serum bottles containing carbon supported Pd-NPs as catalysts. The catalyst supports were attached to the sides of the serum bottle using a double sided carbon tape. An organic buffer solution of 1 mM TAPSO was prepared in MilliQ de-ionized water by adding few drops of 100 mM NaOH to obtain an initial pH of 7.5. 96 mL of TAPSO buffer solution was then added to the reactors, maintaining the solution to headspace ratio of 60:40. The supports in the bottles were rinsed with methanol and water thoroughly to obtain proper wetting conditions (see section 6.2.2), prior to adding the aqueous buffer solution. The reactors were capped with Teflon-lined butyl rubber septa and sealed with an aluminum crimp. The reactors were then purged with a gas mixture of nitrogen and hydrogen (95%N₂-5%H₂, 50 kpa) for 30 minutes. Carefully measured 100 µL volume CT stock solution (initial concentration at 200 ppb CT or 0.125 µmoles of CT mass) was then injected into the batch reactors using a gas-tight syringe and the time was recorded as reaction initiation time (t=0). The bottles were hand-shaken for 60 seconds and spun on an end-to-end rotary shaker (32 rpm, 45° inclination), at room temperature. The reactors were rotated at certain angle in a manner such that the

samples attached on the walls of the reactors remain in the liquid-phase at all times. The reactors were rotated so as to minimize the liquid-gas mass transfer effects. Assuming no mass transfer limitations from liquid to gaseous phase i.e. equilibrium was attained rapidly; 50 μL gaseous samples were removed from the headspace of the reactor at various intervals using a gas-tight glass syringe and analyzed on 7890 GC (Agilent Technologies).

Effect of Support – Pd/Foam Vs Pd/CNT/Foam

Batch experiments were conducted with the following two types of carbon supported catalysts, Pd/Foam and Pd/CNT/Foam. The pristine carbon supports samples without palladium content were also analyzed as reference samples. The size of the supports used was $10 \times 5 \times 2 \text{ mm}^3$ each weighing 55 mg approximately. The reactors conditions were maintained as explained in the methods section (Section 9.6.3.).

Effect of Size of Catalyst Support

Experiments were also carried out on different support sizes that was obtained by adding two supports of Pd/Foam in one reactor and two supports of Pd/CNT/Foam to other reactor [$2 \times (55 \text{ mg} - 10 \times 5 \times 2 \text{ mm}^3 \text{ each})$]. The reactors conditions were maintained as explained in the methods.

7.6. Dechlorination Results

The data obtained from GC are the peak areas at characteristic retention time of the compounds. Values obtained from the respective standards were adapted to match the retention time and convert the peak areas to molar concentrations before and after partitioning (using partitioning coefficients) as summarized in Appendix C (Table C1).

The standard curves obtained for carbon tetrachloride and chloroform are as shown in Figure 41A and 41B.

Effect of the Type of Support

Batch experiments were performed on various carbon supports with and without Pd catalyst, in order to determine the effect of type of support and amount of catalyst loading. Figure 42 shows the degradation of CT (initial mass 0.125 μ moles) obtained for following samples, (a) Foam, (b) CNT/Foam, (c) Pd/Foam, (d) Pd/CNT/Foam, and (e) Control. Foam and CNT/Foam supports without palladium loading were analyzed as reference supports and a control reactor having no catalyst or support was also evaluated. The control reactor is set-up as reference to study the effect of buffer solution and invariably shows 85-90% of initial or theoretical CT concentration. It is evident from the plot that the carbon supports (without Pd) do not show degradation of CT.

The data points from CT degradation were fit using exponential decay model curve for Pd/Foam and Pd/CNT/Foam samples (Fig 43). The plots show the pseudo first-order decay for the Pd/Foam and Pd/CNT/Foam samples, where the equation shows the reaction rate constant as the negative power of exponent. The rate constant of CT degradation is faster with Pd/CNT/Foam catalyst than with Pd/Foam catalyst. The results show that the reaction rate constant was several folds faster with Pd/CNT/Foam samples, in comparison to Pd/Foam. This is consistent since the hierarchical CNT/Foam support accommodates more Pd-NPs per unit volume of the support (Fig. 40). The reaction rate constants for duplicates are given in Appendix C (Table C5).

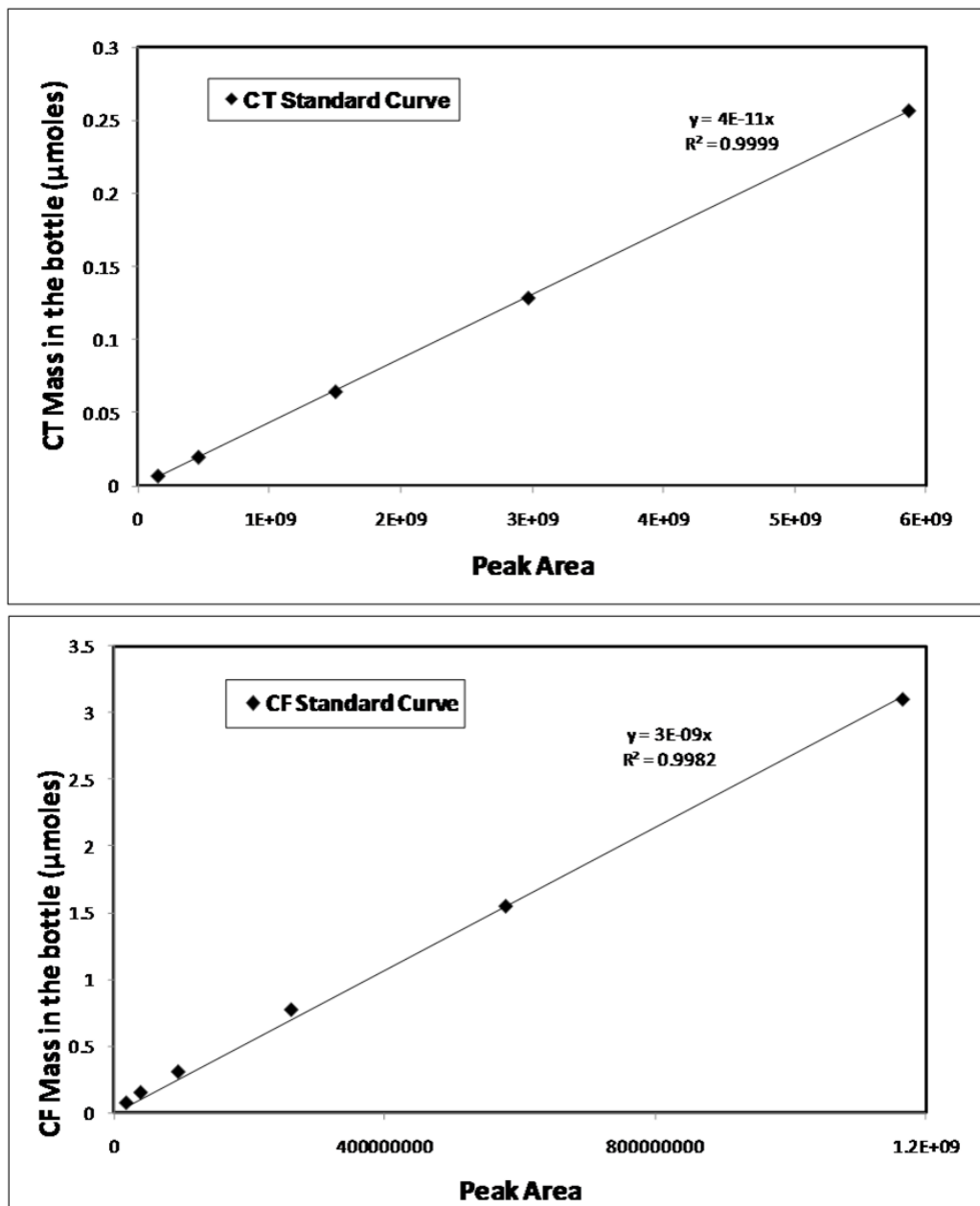


Figure 41 Standard Calibration Curve for (A) Carbon Tetrachloride, CT and (B) Chloroform, CF

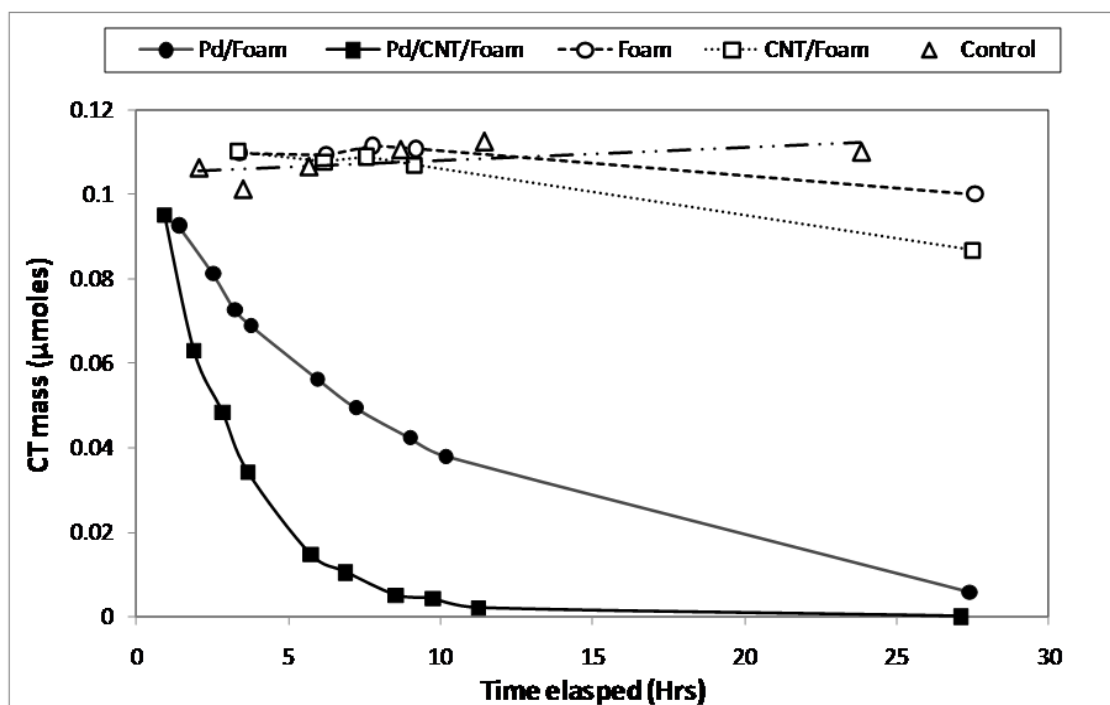


Figure 42 CT Degradation Curves Obtained With Various Catalyst Supports

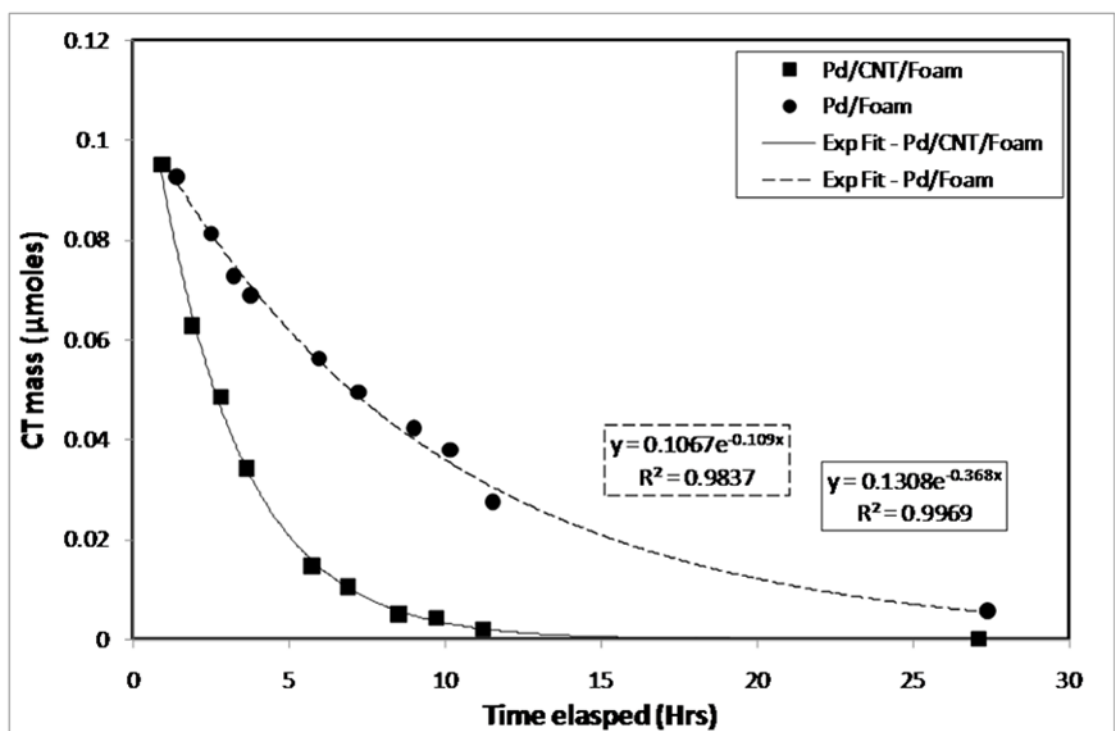


Figure 43 CT degradation Curves Obtained with Single-Size Supports, Pd/Foam and Pd/CNT/Foam

Approximate Exponential Curve Fit Obtained with Pd/Foam and Pd/CNT/Foam Samples

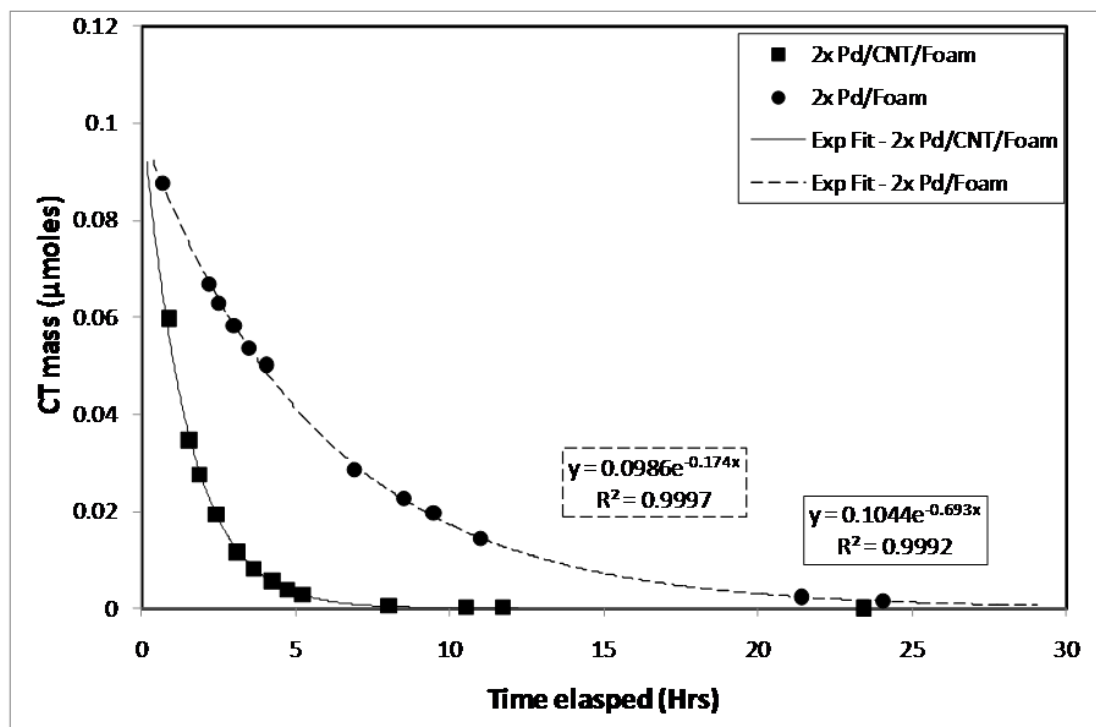


Figure 44 CT degradation Curves Obtained with Double-Size Supports, 2xPd/Foam and 2xPd/CNT/Foam

Approximate Exponential Curve Fit Obtained with 2xPd/Foam and 2xPd/CNT/Foam Samples

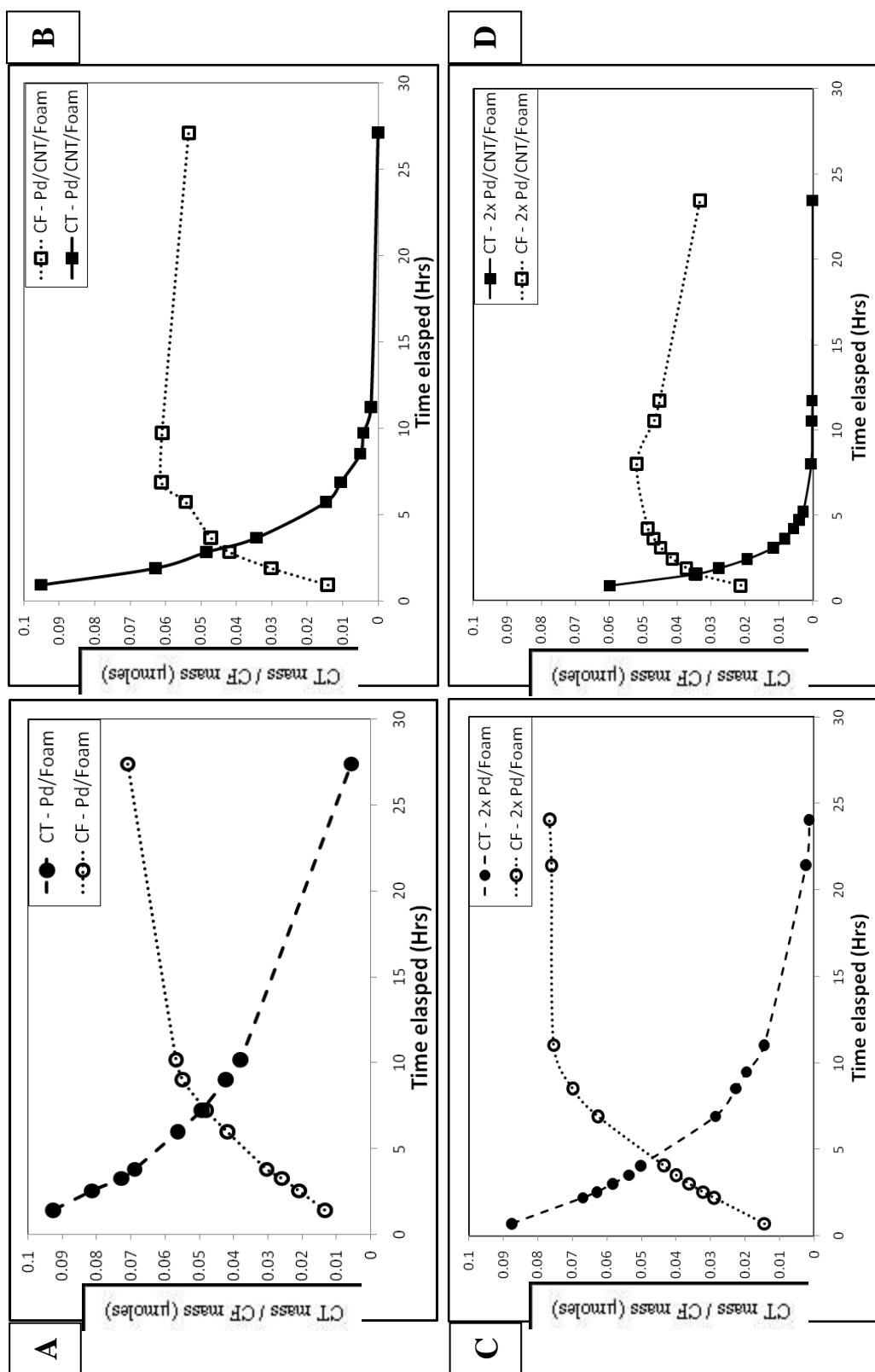


Figure 45 Carbon Tetrachloride Degradation and Chloroform Formation Curves

of (A) Pd/Foam, (B) Pd/CNT/Foam, (C) 2x Pd/Foam, and (D) 2x Pd/CNT/Foam

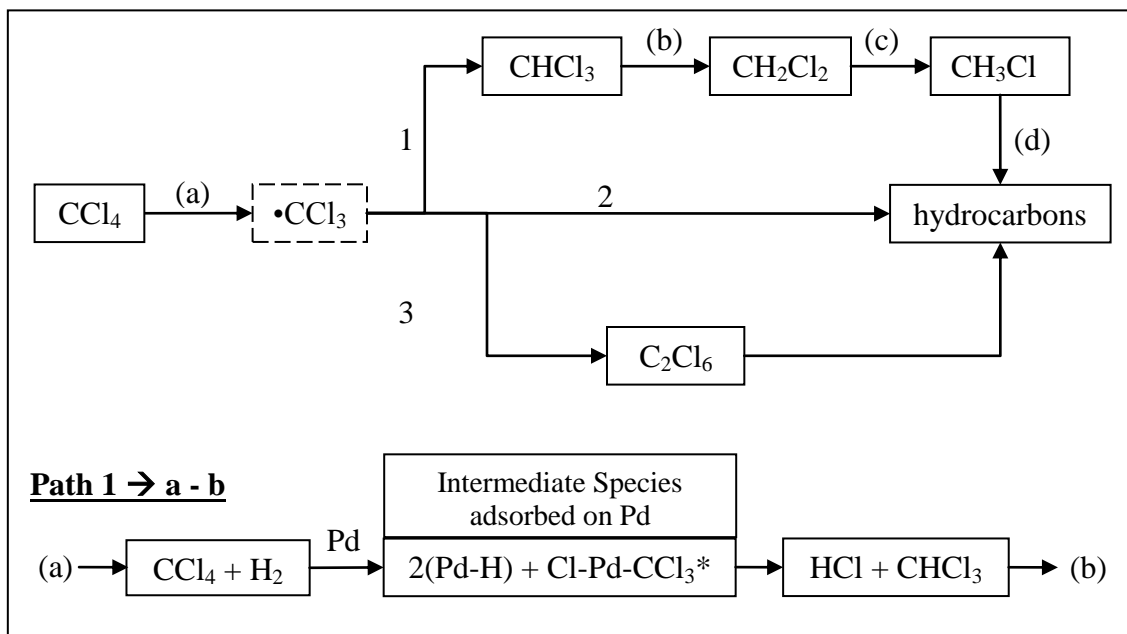


Figure 46 Proposed Mechanism for Catalytic Dechlorination of Carbon Tetrachloride

Proposed using References – 130, 133, 134

Path 1 shows the mechanism of formation of chloroform in the presence of Pd catalyst and H_2 gas

*Intermediate species adsorbed on the Pd active sites

**Reactions b, c, d of Path 1 takes place similarly by the adsorption of intermediate species on the Pd surface sites

Effect of the Size of the Support

The batch experiments were performed to determine the kinetics of CT degradation with varying catalyst size. The size of the supports was doubled by employing two supports of Pd/Foam and Pd/CNT/Foam each to the reactor. Figure 43 shows the CT degradation of samples twice or double the size as used previously. Increase in the size of the support enhances the degradation rates of CT and had an effect proportional to the available area of catalyst (Fig. 44).

Formation of Daughter Products

The dechlorination of carbon tetrachloride with carbon supported Pd-NPs results in rapid and selective formation of chloroform as shown in Figure 45. Chloroform was formed in all cases in the presence of palladium catalyst. The conversion of CT with Pd as catalyst was observed to be 100%. Trace amounts of dichloromethane was also observed after a reaction time of more than 8-10 hours. This can be attributed to the effective reduction of CF to DCM.

Carbon Tetrachloride Dechlorination Mechanism on Pd/H₂ System

In this study, aqueous phase dechlorination of carbon tetrachloride (CCl₄) at ambient temperatures was accomplished using a supported Pd catalyst in the presence of H₂ gas as a reducing agent. The schematic representation of dechlorination mechanism as proposed in the literature is shown in the Figure 46. As shown in this figure, reduction of CT can happen through various reaction pathways. The most favorable catalyzed reaction pathway often observed is Path 1, where CT positively yields daughter products such as chloroform (CHCl₃), dichloromethane (CH₂Cl₂), chloromethane (CH₃Cl), and/or methane (CH₄), and other non-chlorinated carbon species which are less toxic or non-toxic [130,

133, 134]. In this study, in the presence of Pd and H₂, CT is catalytically reduced to CF following Path 1. The degradation mechanism presumably involves steps that include dissociative adsorption of chemical species on the surface of the Pd (through dissociation of H₂ and CCl₄ into intermediate species on the active sites), chemical reaction between the intermediate species forming the reduced product (for example CHCl₃ and HCl), and the desorption of the final products from the catalyst surface or further degradation of the adsorbed intermediate species into the smaller daughter products.

Comparison of the Catalyst Activity on Foam and CNT-Grafted Foam

The duplicates data for all the samples is tabulated in Table C5 of Appendix C. Reproducible results were observed in most of the cases. The dechlorination data stands meaningful as the Pd on both the support (Foam and CNT/Foam) was grown by the identical process, but the Pd/CNT/Foam has improved catalytic activity. It is important to point out that hierarchical CNT supports improve the effectiveness of the metal catalysts as it provides high surface area for hosting metal nanoparticles as well as it exhibits strong interaction with the metal-precursor solution.

No quantitative analysis (such as BET for surface area of Pd or acid leaching for mass of Pd on the samples) has been done to determine the amount of Pd present in the respective samples. A direct correlation between kinetics and Pd mass/area has not been obtained in this study. However, the approximate mass and surface area values were obtained using statistical data from SEM images as tabulated in Table 5. The data summarized in Table 5 shows that Pd/CNT/Foam has few folds (four orders of magnitude) more mass of Pd but it shows relatively small increase in the catalytic activity (Fig. 42 - 43) compared to the Pd/Foam support. One possible reason may be incomplete

percolation of water through the nanotubes forest. This implies that if the CNT-grafted support can be made hydrophilic, deeper infiltration of water can be achieved. It can further improve the scope of these hierarchical supports in the water based environments.

7.7. Catalyst Durability Investigation – SEM, EDAX, and XPS

A defined set of Pd-supported samples were used over and over for all the experiments in this study. The observed CT degradation rates were fairly even for all the experiments or samples (duplicates) tested in the similar experimental conditions. SEM image analysis shows that Pd-NPs were intact with the CNT and EDAX analysis signify that there was no significant difference in the catalyst (Pd) densities, before and after (4 cycles) CT dechlorination test (Fig. 47-48). After retaining the catalyst supports from the reactors, the supports were rinsed thoroughly with methanol and water to avoid any build-up on them. Heavy build-up on CNT was observed (different batch of supports), if the rinsing was not performed plausible from the organic buffer. Immediate rinsing reduced the buildup on CNT, as it was observed to be minimal (Fig. 47). The chemical state of Pd was studied on the Pd/CNT/Foam catalyst before and after (3 cycles) CT dechlorination using XPS. Pd 3d_{5/2} peaks for both as-prepared and used samples were observed at 335.18 eV which indicates that the Pd-NPs did not undergo any chemical change, as shown in the Figure 49. The chlorine peak for the used catalyst was below the detection limit of XPS as shown in Figure 50A and relatively no chlorine was observed. Figure 50B shows the C1s peak after CT degradation shows a satellite peak at 286.1 eV, which can be attributed to the build-up on CNT as observed in SEM. Since relatively no chlorine was present in the sample, it implies that the build-up on CNT were the chlorine

free carbonaceous impurities that could plausibly from the hydrocarbons of organic TAPSO buffer.

The supports immersed in the water-phase of the reactor undergo ~32 revolutions per minute (rpm) continuously for 24 – 48 hrs in the CT dechlorination via batch test. The fact that the Pd-NPs stays intact with the foam (not included here) and CNT/Foam supports, after multiple cycles of such rigorous batch tests of CT dechlorination, signifies the reliability of both supports and Pd-NPs fabricated on these supports. Also these catalysts are chemically stable as the electronic state of the supported Pd does not change after the dechlorination analysis. Pd-NPs attached to these hierarchical carbon supports can be recovered easily and reused multiple times. Study on the catalyst-life of the Pd-NPs on these supports is beyond the scope of this study. It will be analyzed in the future and published elsewhere.

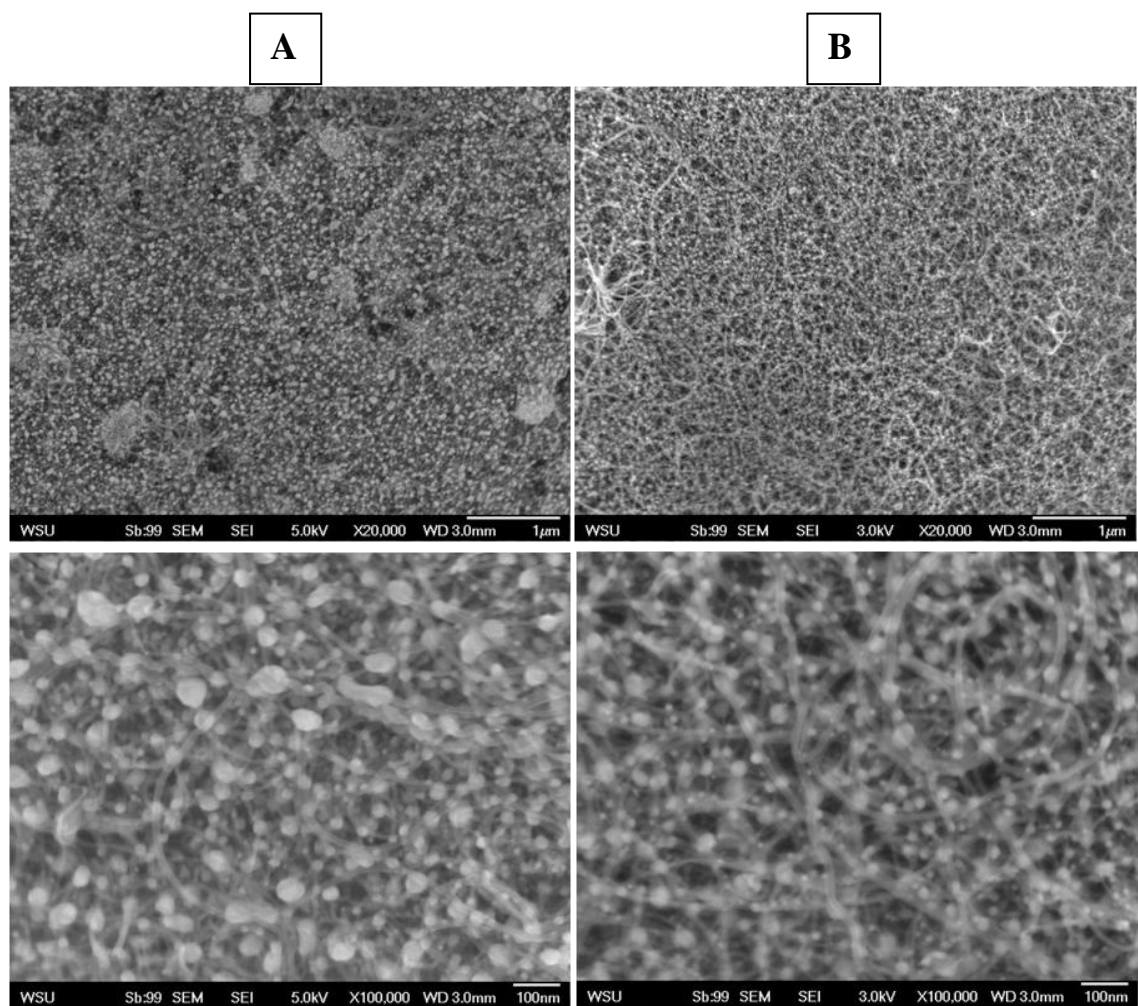


Figure 47 SEM Micrographs of Pd/CNT/Foam (A) Before and (B) After CT Dechlorination Test

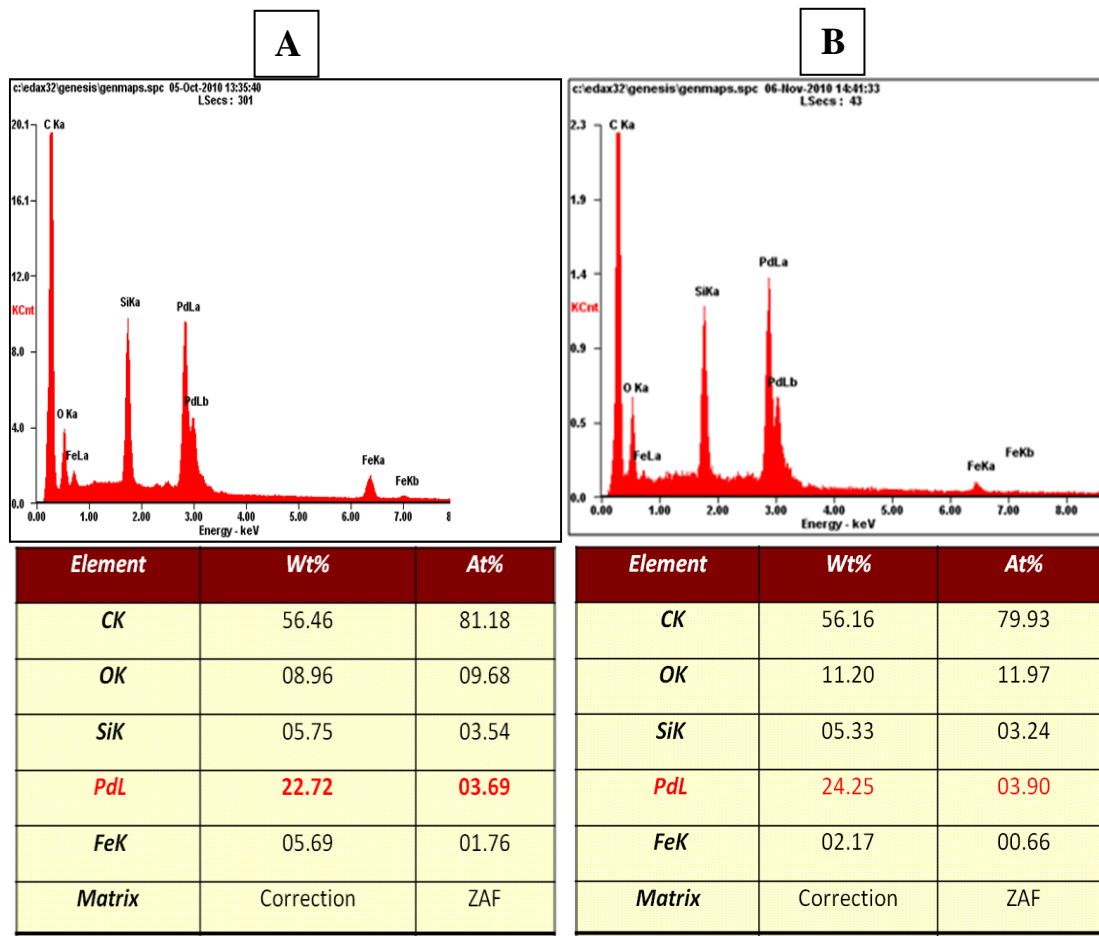


Figure 48 EDAX Results of Pd/CNT/Foam (A) Before and (B) After CT Dechlorination Test

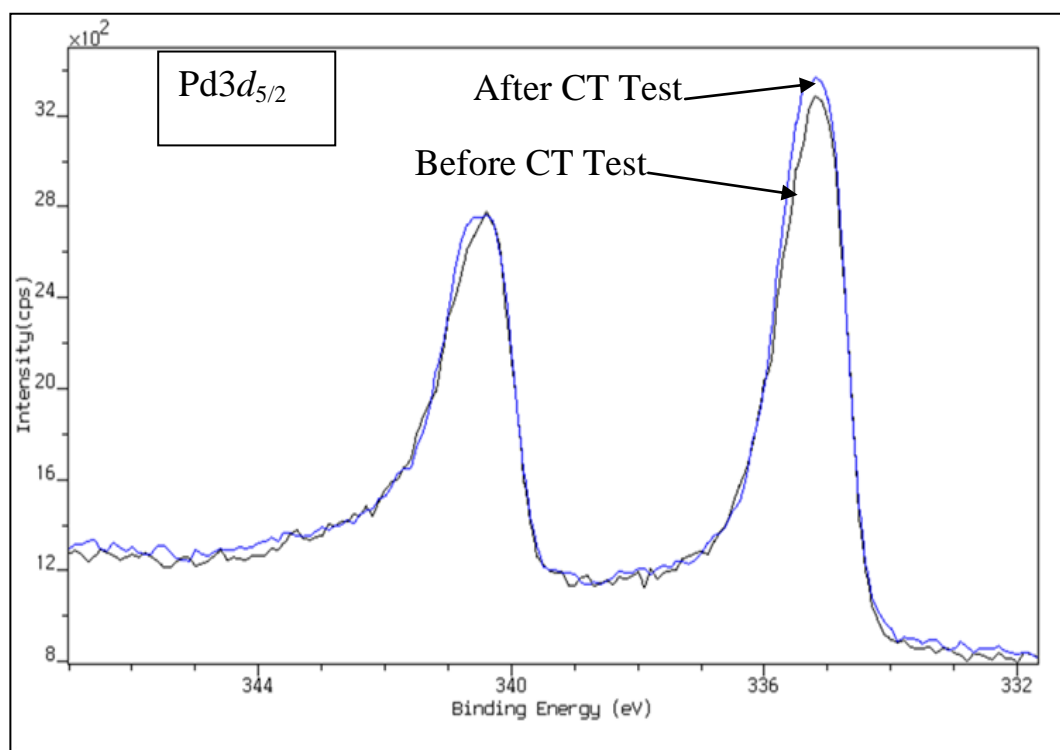


Figure 49 XPS Pd 3d Fine-Scan Spectra of Pd/CNT/Foam Before and After CT Dechlorination,

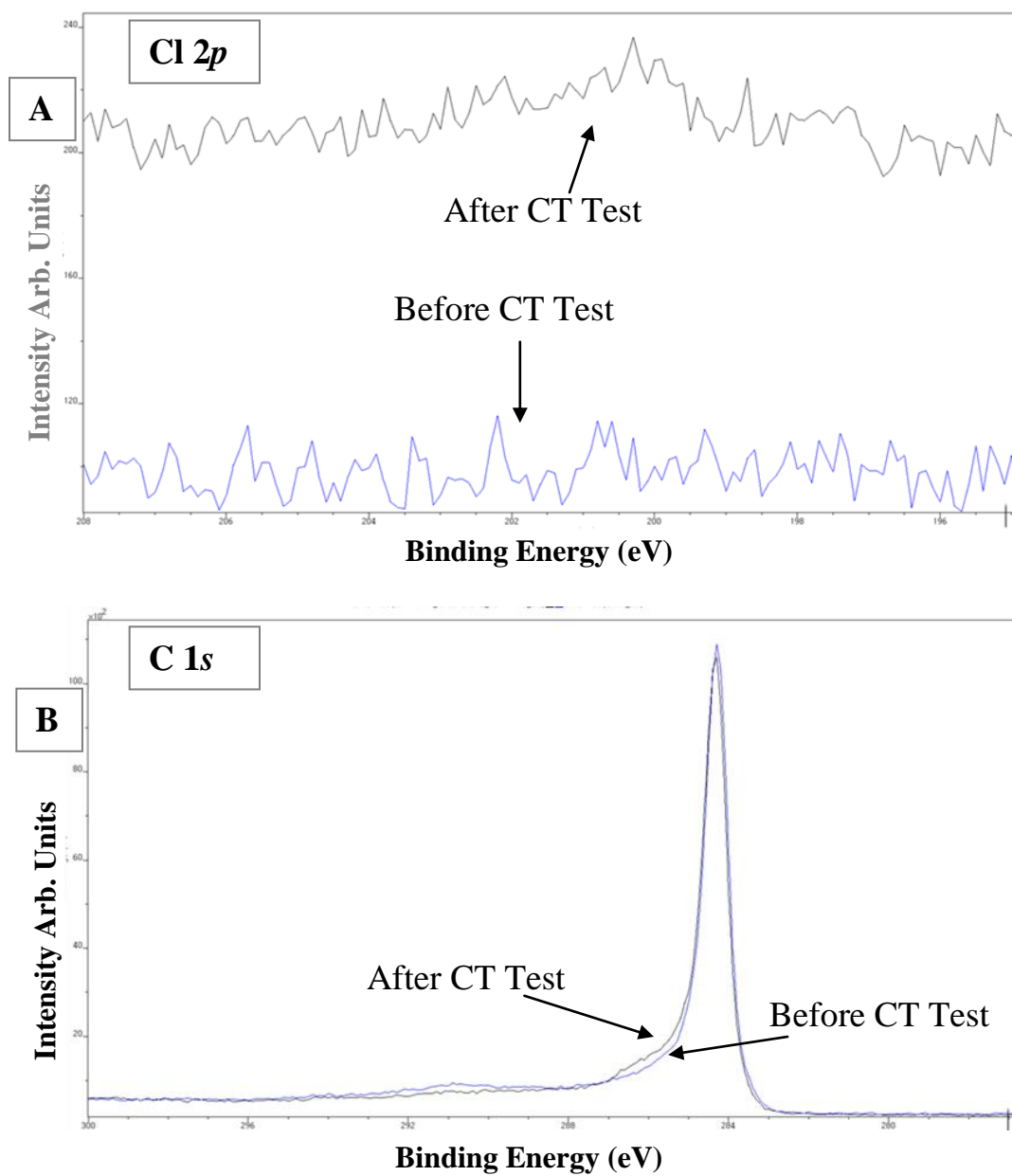


Figure 50 XPS (A) Cl 2p Fine-Scan and (B) C 1s Fine-Scan Spectra of Pd/CNT/Foam Before and After CT Dechlorination.

8. CONCLUSIONS AND FUTURE WORKS

In this research, Pd-carbon based structures having multi-scale architecture have been successfully developed. An insight to nanocatalyst fabrication techniques has been given, focusing on support morphology relevant to specific pretreatment support properties and effects of the heat-treating environment. The precursor and support interactions play a key role in the amount of Pd loaded on the support. Well-dispersed Pd nano-particles of various sizes and dispersion have been attached to micro-porous carbon foam. It was seen that the surface modifications had only a minimal impact when compared to samples having multiple numbers of coatings. It was also observed that a finely tuned size distribution of particles was obtained when using the double coating process. This research shows that the available surface area of the support is increased by creating hierarchical architecture with CNT, enhancing the Pd particle density. The palladium nanoparticles attached to carbon nanotubes grafted on micro-porous foam represents a multi-scale 3-dimensional hierarchical structure having. Major advantages of this is that a large amount of catalytic surface with high surface activity can be obtained resulting in smaller and lighter components in the form of robust porous solids.

The carbon supported Pd-NP samples fabricated in this project have been successfully employed as catalysts for reductive dechlorination of CCl_4 . Batch experiments were conducted at bench-scale that showed complete degradation of CT with supported Pd^0 nanoparticles, where CT was mostly transformed to less-toxic chloroform. Pd/CNT/Foam catalyst shows very high activity and is effective for rapid degradation of CT. XPS shows that Pd-NPs are stable in their metallic form (Pd^0) after three cycles of

catalytic degradations. These supported Pd-NPs can be used repeatedly that forms a cost-effective highly active catalyst for the removal of organic pollutants like CT.

These structures should also have potential use in hydrogen storage, electrochemical devices, as well as catalytic convertors of multiple pollutants. Future investigation will be geared towards the aforementioned applications.

APPENDIX A

ABBREVIATIONS AND CHEMICAL COMPOUNDS

ADF – Annular dark field detector

Au – Gold

BE – Binding energy

BF – Bright Field detector

CCVD - Catalytic chemical vapor deposition

CF –Chloroform

CFC – Chloroflouro hydrocarbons

CNF - Carbon nanofibers

CNT - Carbon nanotubes

CO – Carbon monoxide

COC – Chlorinated organic compounds

CT – Carbon tetrachloride

CdSe – Cadmium selenide

DP – Deposition-precipitation

EDAX – Energy dispersive spectroscopy

ESCA – Electron spectroscopy for chemical analysis

FeO, Fe₂O₃ – Iron Oxide

FE-SEM – Field emission scanning electron microscopy

fs – femto-second

FWHM - Full width half maximum

H₂ - Hydrogen

HCl – Hydrochloric acid

H₂PdCl₄ - Dihydrogen tetrachloropalladate (II)

HMDSO – Hexmethyl-di-siloxane

HOPG – Highly oriented pyrolytic graphite

KE – Kinetic energy

LPS – Liquid phase synthesis

MWCNT - Multi wall carbon nanotubes

NaBH₄ – Sodium Borohydride

Nd:YAG – Neodymium doped yttrium aluminum garnet, Nd: Y₃Al₃O₁₂

NPs - Nanoparticles

ns – nano-second

PCB – Polychlorinated biphenyls

PCE – Tetrachloroethylene

Pd - Palladium

Pd(OAc)₂ – Palladium acetate

PdCl₂ – Palladium chloride

Pd-NPs - Palladium nanoparticles

Pt - Platinum

SEM - Scanning electron micrograph

STEM – Scanning transmission electron micrograph

SWCNT - Single wall carbon nanotubes

TAPN – Tetraamine palladium (II) nitrate, [Pd(NH₃)₄](NO₃)₂

TCE – Trichloroethylene

TEOS – Tetraethoxysilane

TiO₂ – Titania

UHV – Ultra high vacuum

XPS – X-ray photoelectron spectroscopy

Z – Atomic number

ZVM – Zero valent metals

3-D – Three Dimensional

APPENDIX B

Pd Loading in Different Levels of Pores

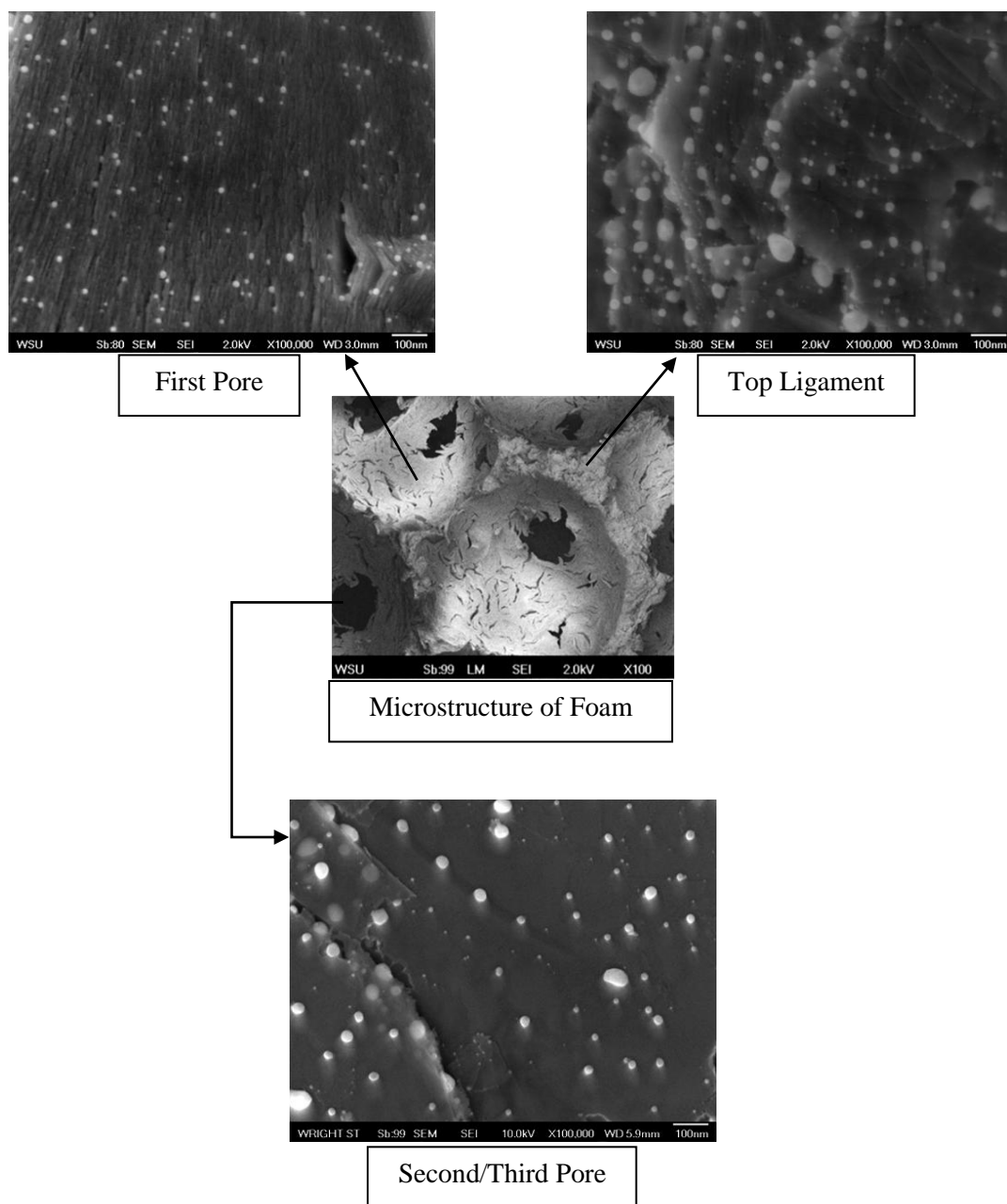


Figure B1 SEM Micrographs of Different Pores, Pd-NPs Fabricated on Carbon Foam

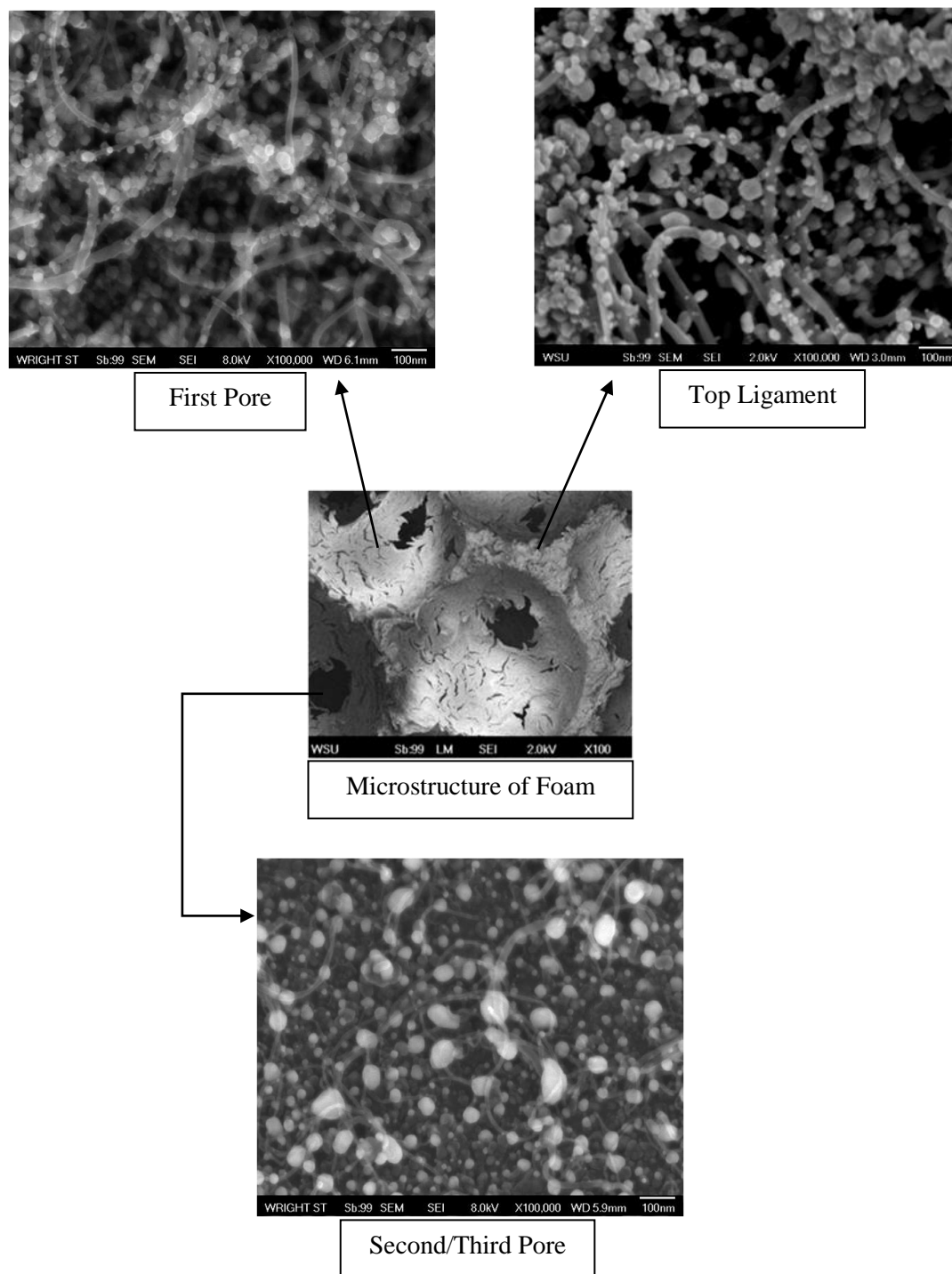


Figure B2 SEM Micrographs of Different Pores, Pd-NPs Fabricated on CNT-Grafted Carbon Foam

APPENDIX C

Batch Test Analytical Data

Table C1 Carbon Tetrachloride Stock Solution Calculations

Carbon Tetrachloride STOCK Solution Preparations			
<i>S.No</i>	<i>Description</i>	<i>Formula</i>	<i>Amount</i>
1	Density of carbon tetrachloride	D_{CT}	1.58 g/cc
2	Volume of water in bottle	V	160 mL
3	Vol. Pure CT injected into stock bottle	V_{CT}	20 μ L
4	Mass. CT in stock bottle	$M_{CT} : D_{CT} \times V_{CT}$	31.6 mg
5	Concentration of stock solution	$ST_{Conc} : M_{CT} / V$	197.5 mg/L (ppm)

Table C2 Standard Solution Calculations for Carbon Tetrachloride

Carbon Tetrachloride STANDARD Solution Preparations – Example Calculations			
<i>S.No</i>	<i>Description</i>	<i>Formula</i>	<i>Amount</i>
1	Total Volume of Reactor Bottle	V	160 mL
2	Volume of water, 60%	V_W	96 mL
3	Volume of air, 40%	V_A	64 mL
4	Molecular Weight CT	MW_{CT}	153.82 g/mol
5	Dimensionless Henry's Constant for CT at 24.8°C, Partitioning Coefficient	K_H'	0.963
6	F_W (fraction in water),	$F_W = 1 \div (1 + K_H' \times V_A \div V_W)$	0.609
7	Volume of stock to be injected (5, 10, 50, 100, or 200 μ L)	V_{STC}	5 μ L
8	Total CT mass in the bottle	$M_{CT} = V_{STC} \times ST_{Conc}$	0.9875 μ g
9	Total CT mass in the bottle (μ moles)	$M_{CTstd} = M_{CT} \div MW_{CT}$	0.00641 μ moles
10	Aqueous CT before partitioning (μ g/L)	$A_{bp} = M_{CT} \div V_W$	10.286 μ g/L (ppb)
11	Aqueous CT after partitioning (μ g/L)	$A_{ap} = A_{bp} \times F_W$	6.265 μ g/L (ppb)
12	Aqueous CT after partitioning (μ moles)	$A_{ap1} = (A_{ap} \times V_W) / MW_{CT}$	0.0039 μ moles

Table C3 Data Plotted for Carbon Tetrachloride Standards Curve

<i>S.No</i>	Vol. of CT Stock injected (μL)	Target Conc. in 160ml bottle with 40% headspace		GC Peak Areas		
		CT ($\mu\text{g/L}$) or (ppb)	CT Mass (μmoles)	Area 1	Area 2	Average
1	5	10.286	0.0064	1.40E+08	1.53E+08	1.47E+08
2	15	30.859	0.0193	4.56E+08	4.54E+08	4.55E+08
3	50	102.865	0.0642	1.47E+09	1.53E+09	1.50E+09
4	100	205.729	0.1284	2.93E+09	3.01E+09	2.97E+09
5	200	411.458	0.2568	5.97E+09	5.77E+09	5.87E+09

Table C4 Data Plotted for Chloroform Standards Curve

<i>S.No</i>	Vol. of CF Stock injected (μL)	Target Conc. in 160ml bottle with 40% headspace		GC Peak Areas		
		CF ($\mu\text{g/L}$) or (ppb)	CF Mass (μmoles)	Area 1	Area 2	Average
1	5.0	9.25	0.0077	1.80E+07	1.80E+07	1.80E+07
2	10.0	18.5	0.0155	3.44E+07	4.41E+07	3.92E+07
3	20.0	37.0	0.0310	9.48E+07	9.48E+07	9.48E+07
4	50.0	92.5	0.0775	2.62E+08	2.62E+08	2.62E+08
5	100.0	185.0	0.1550	5.79E+08	5.79E+08	5.79E+08
6	200	370.0	0.3099	1.17E+09	1.17E+09	1.17E+09

Table C5 Dechlorination Kinetics Including Duplicates

Sample	Function	Dechlorination Kinetics K_{obs} (T)⁻¹ hr⁻¹
Pd/Foam	Shown	0.109
	Duplicate	0.115
	Triplicate	0.095
2x Pd/Foam	Shown	0.174
Pd/CNT/Foam	Shown	0.368
	Duplicate	0.306
	Triplicate	0.252
2x Pd/CNT/Foam	Shown	0.693
	Duplicate	0.584

REFERENCES

1. J. N. Armor, "New catalytic technology commercialized in the USA during the 1990s", *Applied Catalysis A: General*, **222**, 407–426, (2001).
2. G. C. Bond, "The mechanism of catalytic hydrogenation and related reactions", *Quart. Rev.* **8**, 279-307, (1954).
3. C. Batchelor-McAuley, C.E. Banks, A.O. Simm, T. G. J. Jones, and R.G. Compton, "Nano-electrochemical detection of hydrogen or protons using palladium nanoparticles: Distinguishing surface and bulk hydrogen", *Chem. Phys. Chem.*, **7**, 1081-1085, (2006).
4. P. Millet and M. Guymont, "Metal hydrides : Activation procedures, thermodynamics and kinetic analysis", 2IWH 2007, 27-29 October 2007, Ghardaïa – Algeria.
5. L. Schlapbach and A. Züttel, "Hydrogen-storage materials for mobile applications", *Nature*, **414**, 353-358, (2001).
6. (a) S. Grigoriev, E. Lyutikova, S. Martemianov, V. Fateev, C. Lebouin C and P. Millet, "Palladium-based electrocatalysts for PEM applications", *WHEC*, **16**, 13-16, (2006).
 (b) Z. Chang, H. Fan, K. Zhao, M. Chen, P. He, and Y. Fang, "Electrochemical DNA biosensors based on palladium nanoparticles combined with carbon nanotubes", *Electroanalysis*, **20**, 131-136, (2008).
 (c) G. V. Lowry and M. Reinhard, "Pd-catalyzed TCE dechlorination in groundwater: Solute effects, biological control, and oxidative catalyst regeneration", *Environ. Sci. Technol.*, **34**, 3217-3223, (2000).
7. (a) Z. Shi, J. A. Szpunar, "Synthesis of an ultra-thin palladium membrane for hydrogen extraction", *J. Rev. Adv. Mater. Sci.*, **15**, 1-9, (2007).
 (b) F. Rahimi, A. I. Zad, "Characterization of Pd nanoparticle dispersed over porous silicon as a hydrogen sensor", *J. Phys. D, Appl. Phys.*, **40**, 7201-7209, (2007).

8. Y. Li, X. Fan, J. Qi, J. Ji, S. Wang, G. Zhang, and F. Zhang, "Palladium nanoparticle–graphene hybrids as active catalysts for the suzuki reaction", *Nano Res.*, **3**, 429–437, (2010).
9. V. L. Budarin, J. H. Clark, R. Luque, D. J. Macquarrie, and R. J. White, "Palladium nanoparticles on polysaccharide-derived mesoporous materials and their catalytic performance in C–C coupling reactions", *Green Chem.*, **10**, 382–387, (2008).
10. R. Dittmeyer, V. Hollein, and K. Daub, "Membrane reactors for hydrogenation and dehydrogenation processes based on supported palladium", *Journal of Molecular Catalysis A: Chemical*, **173**, 135–184, (2001).
11. G. Schmid, "Large clusters and colloids. Metals in the embryonic state", *Chem. Rev.*, **92**, 1709- 1727, (1992).
12. L. J. de Jongh, "Metal-cluster compounds: model systems for nanosized metal particles", *Applied Organometallic Chemistry*, **12**, 393–399, (1998).
13. G. C. Bond, "The origins of particle size effects in heterogeneous catalysis", *Surface Science*, **156**, 966-981, (1985).
14. G. C. Bond, "Supported metal catalysts: Some unsolved problems", *Chem. SOC. Rev.*, **20**, 441-475, (1991).
15. J. Turkevich, P. C. Stevenson and J. Hillier, "A study of the nucleation and growth processes in the synthesis of colloidal gold", *Discuss. Faraday Soc.*, **11**, 55-75, (1951).
16. R. M. Crooks, M. Qi Zhao, L. Sun, V. Chechik, and L. K. Yeung, "Dendrimer-encapsulated metal nanoparticles: synthesis, characterization, and applications to catalysis", *Accounts of Chemical Research*, **34**, 181-190, (2001).
17. S.Uk. Son, Y. Jang, K. Y. Yoon, E. Kang, and T. Hyeon, "Facile synthesis of various phosphine-stabilized monodisperse palladium nanoparticles through the understanding of coordination chemistry of the nanoparticles", *Nano Lett.*, **4**, 1147 - 1151, (2004).

18. M. A. R. Meier, M. Filali, J. -F. Gohy, and U. S. Schubert, "Star-shaped block copolymer stabilized palladium nanoparticles for efficient catalytic Heck cross-coupling reactions", *J. Materials Chemistry*, **16**, 3001-3006, (2006).
19. G. C. Bond, "Metal-support and metal-additive effects in catalysis", *J. Platinum Metals Rev.*, **27**, 16-18, (1983).
20. (a) S. J. Tauster, "Strong metal-support interactions", *J. Accounts of Chemical Research*, **20**, 389-394, (1987).
 (b) S. J. Tauster, S. C. Fung, and R. L. Garten, "Strong metal-support interactions: Group 8 noble metals supported on TiO₂", *J. American Chemical Society*, **100**, 170-175, (1978).
21. S. J. Tauster, S. C. Fung, R. T. K. Baker, and J. A. Horsley, "Strong interactions in supported-metal catalysts", *Science*, **211**, 1121 - 1125, (1981).
22. D. J. Suh, C. Kwak, Jin-H. Kim, S. M. Kwon, and Tae-J. Park, "Removal of carbon monoxide from hydrogen-rich fuels by selective low-temperature oxidation over base metal added platinum catalysts", *Journal of Power Sources*, **142**, 70-74, (2005).
23. B. I. Yakobson and R. E. Smalley, "Fullerene nanotubes: C_{1,000,000} and beyond", *American Scientist*, **85**, 324-337, (1997).
24. E. Auer, A. Freund, J. Pietsch, and T. Tacke, "Carbons as supports for industrial precious metal catalysts", *Applied Catalysis A: General*, **173**, 259-271, (1998).
25. A. Cabiac, T. Cacciaguerra, P. Trens, R. Durand, G. Delhay, A. Medevielle, D. Plee, and B. Coq, "Influence of textural properties of activated carbons on Pd/carbon catalysts synthesis for cinnamaldehyde hydrogenation", *Applied Catalysis A: General*, **340**, 229-235, (2008)
26. M. Platt, R. A. W. Dryfe, and E. P. L. Roberts, "Electrodeposition of palladium nanoparticles at the liquid/liquid interface using porous alumina templates", *J. Electrochimica Acta*, **48**, 3037 - 3046, (2003).

27. (a) Chien-L. Lee, Yu-C. Huang, Li-C. Kuo, and Yi-W. Lin, "Preparation of carbon nanotube-supported palladium nanoparticles by self-regulated reduction of surfactant", *Carbon*, **45**, 203-228, (2007).
 (b) G.C. Wildgoose, C.E. Banks, and R.G. Compton, "Metal nanoparticles and related materials supported on carbon nanotubes: methods and applications", *Small*, **2**, 182-193, (2006).
28. (a) W. Zhu, C. Zeng, J. P. Zheng, R. Liang, C. Zhang, and B. Wang, "Preparation of buckypaper supported Pt catalyst for pemfc using a supercritical fluid method", *Electrochemical and Solid-State Letters*, **14**, B81-B83, (2011).
 (b) W. Zhu, D. Ku, J.P. Zheng, Z. Liang, B. Wang, C. Zhang, S. Walsh, G. Au, and E.J. Plichta, "Buckypaper-based catalytic electrodes for improving platinum utilization and PEMFC's performance", *Electrochimica Acta*, **55**, 2555–2560, (2010).
29. S. M. Mukhopadhyay, A. Karumuri, and I. Barney, "Hierarchical nanostructures by nanotube grafting on porous cellular surfaces", *J. Phys. D: Appl. Phys.*, **42**, 195503, (2009).
30. S. M. Mukhopadhyay, N. Mahadev, P. Joshi, A.K. Roy, K. Kearns, and D. Anderson, "Structural investigation of graphitic foam", *Journal of Applied Physics.*, **91**, 3415 - 3420, (2002).
31. R. V. Pulikollu, S. R. Higgins, and S. M. Mukhopadhyay, "Model nucleation and growth studies of nanoscale oxide coatings suitable for modification of microcellular and nano-structured carbon", *Surface & Coatings Technology*, **203**, 65–72, (2008).
32. R. V. Pulikollu and S. M. Mukhopadhyay, "Nanoscale coatings for control of interfacial bonds and nanotube growth", *Applied Surface Science*, **253**, 7342–7352, (2007).
33. S. M. Mukhopadhyay, P. Joshi, and R. V. Pulikollu, "Thin films for coating nanomaterials", *Tsinghua Sci. Technol.*, **10**, 709-717, (2005).
34. S.M. Mukhopadhyay, R.V. Pulikollu, and A.K. Roy, "Surface modification of a microcellular porous solid: carbon foam", *Appl. Surf. Sci.*, **225**, 223-228, (2004).

35. S. Zhu, Ching-H. Su, S. L. Lehoczky, I. Muntele, and D. Ila, "Carbon nanotube growth on carbon fibers", *Diamond and Related Materials*, **12**, 1825–1828, (2003).
36. S. M. Mukhopadhyay and A. K. Karumuri, "Nanotube attachment for prevention of interfacial delamination", *J. Phys. D: Appl. Phys.*, **43**, 365301, (2010).
37. (a) Z. Tang, H. Y. Ng, J. Lin, A. T. S. Wee, and D. H. C. Chua, "Pt/CNT-based electrodes with high electrochemical activity and stability for proton exchange membrane fuel cells", *Journal of The Electrochemical Society*, **157**, B245-B250, (2010).
 (b) A.M. Kannan, P. Kanagala, and V. Veedu, "Development of carbon nanotubes based gas diffusion layers by in situ chemical vapor deposition process for proton exchange membrane fuel cells", *Journal of Power Sources*, **192**, 297–303, (2009).
38. P. Marcus and C. Hinnen, "XPS study of the early stages of deposition of Ni, Cu and Pt on HOPG", *Surface Science*, **392**, 134–142, (1997).
39. E. Sacher, "Asymmetries in transition metal xps spectra: metal nanoparticle structure, and interaction with the graphene-structured substrate surface", *Langmuir*, **26**, 3807–3814, (2010).
40. S. Niyogi, M. A. Hamon, H. Hu, B. Zhao, P. Bhowmik, R. Sen, M. E. Itkis, and R. C. Haddon, "Chemistry of single-walled carbon nanotubes", *Acc. Chem. Res.*, **35**, 1105–1113, (2002).
41. E. Gaffet, M. Abdellaoui, and N. Malhouroux-Gaffet, "Formation of nanostructural materials induced by mechanical processing", *Materials Transactions*, **36**, 198–209, (1995).
42. C.C. Koch, "Top-down synthesis of nanostructured materials: mechanical and thermal processing methods", *Rev. Adv. Mater. Sci.*, **5**, 91–99, (2003).
43. (a) H. Bonnemann and K. S. Nagabhushana, "Metal Nanoclusters: Synthesis and strategies for their size control", **Eds.**, B. Corain, G. Schmid, and N. Toshima, "Metal nanoclusters in catalysis and materials science. The issue of size control", ISSN – 978-0-444-53057-8, (2008).

- (b) C. Besson, E. E. Finney, and R. G. Finke, "Nanocluster nucleation, growth, and then agglomeration kinetic and mechanistic studies: A more general, four-step mechanism involving double autocatalysis", *Chem. Mater.*, **17**, 4925-4938, (2005).
44. M. A. Watzky and R. G. Finke, "Transition metal nanocluster formation kinetic and mechanistic studies. A new mechanism when hydrogen is the reductant: slow, continuous nucleation and fast autocatalytic surface growth", *J. Am. Chem. Soc.*, **119**, 10382-10400, (1997).
45. B. L. V. Prasad, S. I. Stoeva, C. M. Sorensen, and K. J. Klabunde, "Digestive-ripening agents for gold nanoparticles: Alternatives to thiols", *Chem. Mater.*, **15**, 935-942, (2003).
46. G. M. Wallraff and W. D. Hinsberg, "Lithographic imaging techniques for the formation of nanoscopic features", *Chem. Rev.*, **99**, 1801-1821, (1999).
47. T. M. Bloomstein, M. W. Horn, M. Rothschild, R. R. Kunz, S. T. Palmacci, and R. B. Goodman, "Lithography with 157 nm lasers", *J. Vac. Sci. Technol. B*, **15**, 2112 -2116, (1997).
48. S. D. Berger, J. M. Gibson, R. M. Camarda, R. C. Farrow, H. A. Huggins, J. S. Kraus, and J. A. Liddle, "Projection electron-beam lithography: A new approach", *J. Vac. Sci. Technol. B*, **9**, 2996-2999, (1991).
49. J. Boneberg, F. Burmeister, C. Schafle, and P. Leiderer, "The formation of nano-dot and nano-ring structures in colloidal monolayer lithography", *Langmuir*, **13**, 7080-7084, (1997).
50. J. C. Hulteen and R. P. Van Duyne, "Nanosphere lithography: A materials general fabrication process for periodic particle array surfaces", *J. Vac. Sci. Technol. A*, **13**, 1553-1558, (1995).
51. A. S. Eppler, G. Rupprechter, L. Gucci, and G. A. Somorjai, "Model catalysts fabricated using electron beam lithography and pulsed laser deposition", *J. Phys. Chem. B*, **101**, 9973-9977, (1997).

52. A. Akey, C. Lu, L. Yang, and I. P. Herman, "Formation of thick, large-area nanoparticle superlattices in lithographically defined geometries", *Nano Lett.*, **10**, 1517–1521, (2010).
53. (a) S. Huang, A. W. H. Mau, T. W. Turney, P. A. White, and L. Dai, "Patterned growth of well-aligned carbon nanotubes: A soft-lithographic approach", *J. Phys. Chem. B*, **104**, 2193 - 2196 (2000).
- (b) A. Javey and H. Dai, "Regular arrays of 2 nm metal nanoparticles for deterministic synthesis of nanomaterials", *J. Am. Chem. Soc.*, **127**, 11942-11943, (2005).
- (c) E. J. Bae, W. B. Choi, K. S. Jeong, J. Uk Chu, Gyeong-S. Park, S. Song, and I. K. Yoo, "Selective growth of carbon nanotubes on pre-patterned porous anodic aluminum oxide", *J. Adv. Mater.*, **14**, 277- 279, (2002).
- (d) G. Eres, A. A. Puretzky, D. B. Geohegan, and H. Cui, "In situ control of the catalyst efficiency in chemical vapor deposition of vertically aligned carbon nanotubes on pre-deposited metal catalyst films", *Appl. Phys. Lett.*, **84**, 1759-1761, (2004).
54. P. T. Murray and E. Shin, "Formation of silver nanoparticles by through thin film ablation", *Materials Letters*, **62**, 4336-4338, (2008).
55. M. Kalyva, G. Bertoni, A. Milionis, R. Cingolani, and A. Athanassiou, "Tuning of the characteristics of Au nanoparticles produced by solid target laser ablation into water by changing the irradiation parameters", *Microscopy Research and Technique*, **73**, 937-943, (2010).
56. R. M. Tilaki, A. Iraj-Zad, and S. M. Mahdavi, "Stability, size, and optical properties of silver nanoparticles prepared by laser ablation in different carrier media", *Appl. Phys. A.*, **84**, 215-219, (2006).
57. M. A. Pasha, R. Poursalehi, M. A. Vesaghi, and A. Shafiekhani, "The effect of temperature on the TCVD growth of CNTs from LPG over Pd nanoparticles prepared by laser ablation", *Physica B*, **405**, 3468-3474, (2010).

58. J. C. Alonso, R. Diamant, P. Castillo, M. C. Acosta-Garcia, N. Batina, and E. Haro-Poniatowski, "Thin films of silver nanoparticles deposited in vacuum by pulsed laser ablation using a YAG:Nd laser", *Applied Surface Science*, **255**, 4933-4937, (2009).
59. S. Senkan, M. Kahn, S. Duan, A. Ly, and C. Leidholm, "High-throughput metal nanoparticle catalysis by pulsed laser ablation", *Catalysis Today*, **117**, 291-296, (2006).
60. Z. Shi, S. Wu, and J. A. Szpunar, "Synthesis of palladium nanostructures by spontaneous electroless deposition", *Chemical Physics Letters*, **422**, 147-151, (2006).
61. L.A.M. Hermans and J. W. Geus, "Interaction of nickel ions with silica supports during deposition-precipitation." *Stud. Surf. Sci.Catal.*, **3**, 113-130. (1979).
62. C.J.G. Van Der Grift, P.A. Elberse, A. Mulder, and J. W. Geus, "Preparation of silica-supported copper catalysts by means of deposition-precipitation", *Appl. Catal.*, **59**, 275, (1990).
63. J.H. bitter, M.K. van der Lee, A.G.T. Slotboom, A.J. van Dillen, and K.P. de Jong, "Synthesis of highly loaded highly dispersed nickel on carbon nanofibers by homogeneous deposition-precipitation", *Catal. Lett.*, **89**, 139-142 (2003).
64. H. Jin, S.-E. Park, J.M. Lee and S.K. Ryu, "The shape-selectivity of activated carbon fibers as a palladium catalyst support," *Carbon*, **34**, 429-431, (1996).
65. A. Johanssona, J. Lu, J.-O. Carlsson, and M. Boman, "Deposition of palladium nanoparticles on the pore walls of anodic alumina using sequential electroless deposition", *J. Appl. Phys.*, **96**, 5189- 5194, (2004).
66. Y.H. Qin, Y. Jiang, H.H. Yang, X.S. Zhang, X.G. Zhou, L. Niu, and W.K. Yuan, "Synthesis of highly dispersed and active palladium/carbon nanofiber catalyst for formic acid electrooxidation", *Journal of Power Sources*, **196**, 4609-4612, (2011).
67. Y. Tan, X. Dai, Y. Li, and D. Zhu, "Preparation of gold, platinum, palladium and silver nanoparticles by the reduction of their salts with a weak reductant-potassium bitartrate", *J. Mater. Chem.*, **13**, 1069-1075, (2003).

68. G. Schmid, "Clusters and colloids-bridges between molecular and condensed materials", *Materials Chemistry and Physics*, **29**, 133-142, (1991).
69. B. Yoon and C. M. Wai, "Microemulsion-templated synthesis of carbon nanotube-supported Pd and Rh nanoparticles for catalytic applications", *J. AM. CHEM. SOC.*, **127**, 17174-17175, (2005).
70. Y. W. Lee, M. Kima, and S. W. Han, "Shaping Pd nanocatalysts through the control of reaction sequence", *Chem. Commun.*, **46**, 1535-1537, (2010).
71. Y. Piao, Y. Jang, M. Shokouhimehr, I. S. Lee, and T. Hyeon, "Facile aqueous-phase synthesis of uniform palladium nanoparticles of various shapes and sizes", *Small*, **3**, 255-260, (2007).
72. (a) Krijn P. de Jong, "Synthesis of solid catalysts", ISBN: 978-3-527-32040-0, (2009).
(b) W. V. Knowles, M. O. Nutt, and M. S. Wong, "Supported metal oxides and the surface density metric", *Eds, J. Regalbuto, Catalyst Preparation-Science and Engineering*, ISBN: 0849370884, Chapter **11**, 251- 282, (2007).
73. I. Yuranov, P. Moeckli, E. Suvorova, P. Buffat, L. Kiwi-Minsker, and A. Renken, "Pd/SiO₂ catalysts: synthesis of Pd nanoparticles with the controlled size in mesoporous silicas", *J.Molecular Catalysis A: Chemical*, **192**, 239-251, (2003).
74. M. Gurrath, T. Kuretzky, H. P. Boehm, L. B. Okhlopkova, A. S. Lisitsyn, and V. A. Likholobov, "Palladium catalysts on activated carbon supports. Influence of reduction temperature, origin of the support, and pretreatments of the carbon surface", *Carbon*, **38**, 1241-1255, (2000).
75. G. Strukul, F. Pinna, M. Marella, L. Meregalli, and M. Tomaselli, "Sol-gel palladium catalysts for nitrate and nitrite removal from drinking water", *Catalysis Today*, **27**, 209-214, (1996).

76. W. Dong, J. Sakamoto, and B. Dunn, "Electrochemical properties of vanadium oxide aerogels and aerogel nanocomposites", *J. Sol-Gel Science and Technology*, **26**, 641-644, (2003).
77. P. A. Robles-Dutenhefner, D. L. Nunes, J. A. Goncalves, E. V. Gusevskaya, and E. M. B. Sousa, "Sol-gel palladium composites: effect of the thermal treatment on the catalytic activity", *Journal of Non-Crystalline Solids*, **348**, 195-200, (2004).
78. (a) L.C. Cotet, M. Gich, A. Roig, I.C. Popescu, V. Cosoveanu, E. Molins, and V. Danciu, "Synthesis and structural characteristics of carbon aerogels with a high content of Fe, Co, Ni, Cu, and Pd", *Journal of Non-Crystalline Solids*, **352**, 2772–2777, (2006).
 (b) R. W. Pekalaa, J. C. Farmera, C. T. Alvisoa, T. D. Trana, S. T. Mayerb, J. M. Millerc, and B. Dunnc, "Carbon aerogels for electrochemical applications", *Journal of Non-Crystalline Solids*, **225**, 74-80, (1998).
79. S. Cacchi, C. L. Cotet, G. Fabrizi, G. Forte, A. Goggiamani, L. Martin, S. Martinez, E. Molins, M. Moreno-Manas, F. Petrucci, A. Roig, and A. Vallribera, "Efficient hydroxycarbonylation of aryl iodides using recoverable and reusable carbon aerogels doped with palladium nanoparticles as catalyst", *Tetrahedron*, **63**, 2519–2523, (2007).
80. Ming-Liang Chen, Feng-Jun Zhang, and Won-Chun Oh, "Preparation and catalytic properties of Pt/CNT/TiO₂ composite", *Journal of the Korean Ceramic Society*, **47**, 269-275, (2010).
81. K. S. Morley, P. Licence, P. C. Marr, J. R. Hyde, P. D. Brown, R. Mokaya, Y. Xia, and S. M. Howdle, "Supercritical fluids: A route to palladium-aerogel nanocomposites", *Journal of Materials Chemistry*, **14**, 1212-1217, (2004).
82. J. Shulga, V. Kisand, I. Kink, V. Reedo, L. Matisen, and A. Saar, "Formation of nickel oxide nanostructures on TiO₂", *Journal of Physics: Conference Series*, **93**, 012006, (2007).
83. F. Zheng, L. Liang, Y. Gao, J. H. Sukamto, and C. L. Aardahl, "Carbon nanotube synthesis using mesoporous silica templates", *Nano Lett.*, **2**, 729-732, (2002).

84. R. Pattabiraman, "Electrochemical investigations on carbon supported palladium catalysts", *Applied Catalysis A: General*, **153**, 9-20, (1997).
85. W. C. Mosley, Jr., "Palladium/Kieselguhr composition and method", *United States Patent*, **5248649**, (1993).
86. A.F. Perez-Cadenas, S. Morales-Torres, F. Kapteijn, F.J. Maldonado-Hódar, F. Carrasco-Marin, C. Moreno-Castilla and J.A. Moulijn, "Carbon-based monolithic supports for palladium catalysts: The role of the porosity in the gas-phase total combustion of *m*-xylene", *Applied Catalysis B: Environmental*, **77**, 272-277, (2008).
87. (a) R. F. Egerton, "Physical principles of electron microscopy: An introduction to TEM, SEM, and AEM", ISBN-10: 0387258000, (2005).
 (b) P. J. Goodhew, F. J. Humphreys, R. Beanland, "Electron microscopy and analysis", ISBN: 0748409688, (2001).
 (c) B. L. Gabriel, "SEM: A user's manual for materials science", *American Society for Metals(ASM)*, ISBN-10: 0871702029, (1985).
88. J. F. Watts and J. Wolstenholme, "An introduction to surface analysis by XPS and AES", ISBN – 9780470847138, (2003).
89. R. V. Pulikollu, "Nano-coatings on carbon structures for interfacial modification", Ph.D. Dissertation, Wright State University, (2005).
90. J. -E. Huang, D.-J. Guo, Y.-G. Yao, and H.-L. Li, "High dispersion and electrocatalytic properties of platinum nanoparticles on surface-oxidized single-walled carbon nanotubes", *Journal of Electroanalytical Chemistry*, **577**, 93–97, (2005).
91. Y. Li, F. P. Hu, X. Wang, and P. K. Shen, "Anchoring metal nanoparticles on hydrofluoric acid treated multiwalled carbon nanotubes as stable electrocatalysts", *Electrochemistry Communications*, **10**, 1101–1104, (2008).

92. (a) A. Sepulveda-Escribano, F. Coloma, and F. Rodriguez-Reinoso, "Platinum catalysts supported on carbon blacks with different surface chemical properties", *Applied Catalysis A: General*, **173**, 247-257, (1998).
- (b) F Coloma, A. Sepulveda-Escribano, J. L. G. Fierro, and F. Rodriguez-Reinoso, "Gas phase hydrogenation of crotonaldehyde over Pt/Activated carbon catalysts. Influence of the oxygen surface groups on the support", *Applied Catalysis A: General*, **150**, 165-183, (1997).
93. I.T. Barney, S.M. Mukhopadhyay, and A. Maleszewski, "Strongly bonded carbon nanotubes in porous materials: Growth, characterization, and functionalization of high surface area hierarchical structures", *under review for publishing*, Wright State University.
94. (a) Eric W. Weisstein, "Contact Angle." From MathWorld--A Wolfram, Web Resource: <http://mathworld.wolfram.com/ContactAngle.html>
- (b) Eric W. Weisstein, "Spherical Cap." From MathWorld--A Wolfram, Web Resource: <http://mathworld.wolfram.com/SphericalCap.html>
95. P. Marcus and C. Hinnen, "XPS study of the early stages of deposition of Ni, Cu, and Pt on HOPG", *J. Surface Science*, **392**, 134-142, (1997).
96. D.-Q. Yang and E. Sacher, "s-p Hybridization in highly oriented pyrolytic graphite and its change on surface modification, as studied by x-ray photoelectron and raman spectroscopies", *J. Surface Science* **504** 125-137 (2002).
97. D.-Q. Yang and E. Sacher, "Carbon 1s X-ray Photoemission Line Shape Analysis of Highly Oriented Pyrolytic Graphite: The influence of structural damage on peak asymmetry" *Langmuir*, **22** 860-862 (2006)
98. G. Zhang, D. Yang, and E. Sacher, "Structure and morphology of Co nanoparticles deposited onto highly oriented pyrolytic graphite", *J. Phys. Chem. C*, **111**, 17200-17205, (2007).
99. S. W. Poon, J. S. Pan, and E. S. Tok, "Nucleation and growth of cobalt nanostructures on highly oriented pyrolytic graphite", *J. Phys. Chem. Chem. Phys.*, **8**, 3326-3334, (2006).

100. D.-Q. Yang and E. Sacher, "Characterization and oxidation of Fe nanoparticles deposited onto highly oriented pyrolytic graphite, using x-ray photoelectron spectroscopy", *J. Phys. Chem. C*, **113**, 6418–6425, (2009).
101. D. Briggs and J. T. Grant, "Surface analysis by auger and x-ray photoelectron spectroscopy", ISBN 1-901019-04-7, (1990).
102. G. Mattogno, G. Polsonetti, and G. R. Tauszik, "Characterization of palladium-on-alumina catalysts by x-ray photoelectron spectroscopy", *J. Electron. Spectrosc. Relat. Phenom.*, **14**, 237-243, (1978).
103. M. Narayana, J. Michalik; S. Contarini, and Larry Kevan, "Determination of the chemical state of palladium in PdNa-X zeolite by electron spin resonance and x-ray photoelectron spectroscopy", *J. Phys. Chem.*, **89**, 3895-3899, (1985).
104. M. Brun, A. Berthet, and J. C. Bertolini, "XPS, AES and Auger parameter of Pd and PdO", *J. Electron Spectroscopy and Related Phenomena.*, **104**, 55-60, (1999).
105. T. Pillo, P. Steiner, and S. Hufner, "The electronic structure of PdO found by photoemission (UPS and XPS) and inverse photoemission (BIS)", *J. Phys. Condens. Matter*, **9**, 3987-3999, (1997).
106. (a) I. Kojima and M. Kurahashi, "Application of asymmetric Gaussian/Lorentzian mixed function for x-ray photoelectron curve synthesis", *J. Electron Spectroscopy and Related Phenomena.*, **42**, 177-181, (1987).
 (b) "Quantification using asymmetric line shapes", Casa XPS, Copyright 2005 Casa Software Ltd.
107. H. Wang and Y. wan, "Synthesis of ordered mesoporous Pd/carbon catalyst with bimodal pores and its application in water-mediated Ullmann coupling reaction of chlorobenzene", *J. Mater. Sci.*, **44**, 6553-6562, (2009).

108. S. M. Park, J. W. Park, H.-P. Ha, H.-S. Han, G. Seo, "Storage of NO₂ on potassium oxide co-loaded with barium oxide for NO_x storage and reduction (NSR) catalysts", *Journal of Molecular Catalysis A: Chemical*, **273**, 64–72, (2007).
109. A. Krepelova, J. Newberg, T. Huthwelker, H. Bluhm, and M. Ammann, "The nature of nitrate at the ice surface studied by XPS and NEXAFS", *Phys. Chem. Chem. Phys.*, **12**, 8870–8880, (2010).
110. M. Peuckert, "XPS Study on surface and bulk palladium oxide, its thermal stability, and a comparison with other noble metal oxides", *J. Phys. Chem.*, **89**, 2481-2486, (1985).
111. S. W. Cowley, "Nanocatalysis", **Eds.**, G. L. Hornyak, H. F. Tibbals, J. Dutta, and J. J. Moore, "Introduction to nanoscience and nanotechnology", ISBN- 1-4200-4779-0, Chapter 23., pp 1183-1206, (2008).
112. Z. Ustundag and A. O. Solak, "EDTA modified glassy carbon electrode: Preparation and characterization", *Electrochimica Acta*, **54**, 6426–6432, (2009).
113. A. I. Smolentsev, A. I. Gubanov, A. V. Zadesenets, P. E. Plyusnin, I. A. Baidina, and S. V. Korenev, "Structures of tetraammine salts [Pt(NH₃)₄](NO₃)₂, [Pd(NH₃)₄](NO₃)₂, and [Pd(NH₃)₄]F₂·H₂O", *Journal of Structural Chemistry.*, **51**, 709-713, (2010).
114. (a) E. T. Kang, K. G. Neoh, and K. L. Tan, "X-ray photoelectron spectroscopic characterization of protonation of polyaniline films by polymeric acids", *Polymer*, **35**, 3193-3199, (1994).
 (b) E. T. Kang, K. G. Neoh, K. L. Tan and B. T. G. Tan, "Protonation of the amine nitrogens in emeraldine – evidence from x-ray photoelectron spectroscopy", *Synthetic Metals*, **46**, 227-233, (1992).
115. R. E. Doherty, "A history of the production and use of carbon tetrachloride, Tetrachloroethylene, Trichloroethylene and 1,1,1-Trichloroethane in the United States: Part 1-Historical Background; Carbon Tetrachloride and Tetrachloroethylene." *J. Environmental Forensics*, **1**, 69 – 81, (2000).

116. "Handbook for the Montreal Protocol on substances that deplete the ozone layer" - 7th Edition, United Nations Environment Programme, ISBN 978-92-807-2770-8, (2006).
117. US EPA 1979, "Water-related environmental fate of 129 priority pollutants, Volume II", *Office of water planning and standards and Office of water and waste management, EPA-440/4-79-029b* (1979).
118. US EPA 1987 "Carbon tetrachloride health advisory." *Office of Drinking Water*, U.S. Environmental Protection Agency, Washington, DC, (1987).
119. U.S. EPA 1989 "Health effects assessment for carbon tetrachloride." U.S. Environmental Protection Agency, Cincinnati, Ohio (PB90-142407), (1989).
120. U.S. EPA 1998 "Technical fact sheet on carbon tetrachloride." National Primary Drinking Water Regulations, (1998).
121. "Carbon tetrachloride in drinking water." *Office of Environmental Health Hazard Assessment California Public Health Goal (PHG)*, California Environmental Protection Agency (2000).
122. P. L. McCarty, "Groundwater contamination by chlorinated solvents: History, remediation technologies and strategies", **Eds.**, H. F. Stroo and C. H. Ward, "In Situ Remediation of Chlorinated Solvent Plumes", ISBN 9781441914019, Chapter 1., pp 1-28, (2010).
123. E.A. Voudrias, "Pump-and-treat remediation of groundwater contaminated by hazardous waste: can it really be achieved?", *J. Global Nest: the Int.*, **3**, 1-10, (2001).
124. M. O. Rivett, S. W. Chapman, R. M. Allen-King, S. Feenstra, and J. A. Cherry, "Pump-and-treat remediation of chlorinated solvent contamination at a controlled field-experiment site", *J. Environ. Sci. Technol.*, **40**, 6770-6781, (2006).
125. (a) Y. Jiao, D. Wua, H. Mab, C. Qiu, J. Zhang, and L. Ma, "Electrochemical reductive dechlorination of carbon tetrachloride on nanostructured Pd thin films", *Electrochemistry Communications*, **44**, 1474—1477, (2008).

- (b) Y. H. Liou, S. L. Lo, and C. J. Lin, "Size effect in reactivity of copper nanoparticles to carbon tetrachloride degradation", *Water Research*, **41**, 1705- 1712, (2007).
- (c) V. Mucka, B. Lizalova, M. Pospisil, R. Silber, D. Polakova, and B. Bartonicek, "Radiation dechlorination of PCE in aqueous solutions under various conditions", *Radiation Physics and Chemistry*, **67**, 539–544, (2003).
- (d) L. M. Gomez-Sainero, X. L. Seoane, and A. Arcoya, "Hydrodechlorination of carbon tetrachloride in the liquid phase on a Pd/carbon catalyst: kinetic and mechanistic studies", *J. Applied Catalysis B: Environmental*, **53** 101-110 (2004).
126. R. W. Gillham and S. F. O'Hannesin, "Enhanced degradation of halogenated aliphatics by zero-valent iron", *Ground Water*, **32**, 958–967, (1994).
127. L. J. Matheson, P. G. Tratnyek, "Reductive dehalogenation of chlorinated methanes by iron metal", *J. Environ. Sci. Technol.*, **28**, 2045–2053, (1994).
128. R. Muftikian, Q. Fernando, and N. Korte, "A method for the rapid dechlorination of low molecular weight chlorinated hydrocarbons in water", *Water Research*, **29**, 2434-2439, (1995).
129. L.H. Chen, C.C. Huang, and H.L. Lien, "Bimetallic iron-aluminum particles for dechlorination of carbon tetrachloride", *Chemosphere*, **73**, 692-697, (2008).
130. L.M. Gomez-Sainero, A. Cortes, X. L. Seoane, and A. Arcoya, "Hydrodechlorination of carbon tetrachloride to chloroform in the liquid phase with metal-supported catalysts. Effect of the catalyst components", *J. Ind. Eng. Chem. Res.* **39** 2849-2854 (2000).
131. X. Wang, C. Chen, H. Liu, and J. Ma, "Characterization and evaluation of catalytic dechlorination activity of Pd/Fe bimetallic nanoparticles", *Ind. Eng. Chem. Res.* **47** 8645-8651 (2008)
132. N. Munakata and M. Reinhard, "Palladium catalysis for the treatment of contaminated waters: A review", **Eds.**, J. A. Smith, S. E. Burns, "Physicochemical Groundwater Remediation", ISBN – 0306465698, Chapter 3., pp 45- 71, (2002).

133. G. V. Lowry and M. Reinhard, "Hydrodehalogenation of 1- to 3-carbon halogenated organic compounds in water using a palladium catalyst and hydrogen gas", *Environ. Sci. Technol.*, **33**, 1905-1910, (1999).
134. V. D. Santo, C. Dossi, S. Recchia, P. E. Colavita, G. Vlaic, and R. Psaro, "Carbon tetrachloride hydrodechlorination with organometallics-based platinum and palladium catalysts on MgO", *J. Molecular Catalysis A: Chemical*, **182-183**, 157-166, (2002).